Cape Peninsula
University of Technology

NON-DESTRUCTIVE TESTING AND FINITE ELEMENT MODELLING OF HISTORICAL MASONRY WALL

by

Riaan Jaco Victor

Thesis submitted in fulfilment of the requirements

for the degree

Master of Engineering: Civil Engineering

in the

Faculty of Engineering and the Built Environment

at the

Cape Peninsula University of Technology

Supervisor: Prof. K. Pallav
Co-supervisor: Dr. M. Pourbehi

Bellville
28 November 2022

CPUT copyright information
The thesis may not be published either in part (in scholarly, scientific or technical journals), or as a whole (as a monograph), unless permission has been obtained from the University.

DECLARATION

I, Riaan Jaco Victor, declare that the contents of this thesis entitled "*Non-destructive testing and finite element modelling of historical masonry wall*" represent my work under Prof. Kumar Pallav's guidance and co-supervision of Dr. Mohammed Pourbehi. The financial aid was provided by the Construction Education and Training Authority (CETA) to fulfil the requirements of the degree Master of Engineering: Civil Engineering. The thesis has not previously been submitted for academic examination towards any qualification. Furthermore, it represents my opinions, not necessarily those of the Cape Peninsula University of Technology.

28 November 2022

Signed **Date**

ABSTRACT

The conservation of heritage structures is a critical field often overlooked worldwide, with developing countries severely lacking in the field. The lack of adequate and sustainable conservation has led to the degradation of many heritage structures. This research investigates the Non-Pareille manor house, an excellent example of Cape Dutch architecture. The manor house is classified as a Grade 1 heritage resource by SAHRA, the highest level of significance in South African heritage. The mechanical properties of the front gable wall of the Non-Pareille manor house have been determined through non-destructive testing and finite element analysis.

The non-destructive testing methods used in this research are rebound hammer testing and ultrasonic pulse velocity testing. The surface level compressive strength has been determined through rebound hammer testing, following calibration through site sample crushing in a laboratory. Poisson’s ratio and Young’s Modulus for the masonry have been calculated from ultrasonic pulse velocity test results. From visual inspection, severe cracking above the door opening has been noted and remediation is recommended to avoid further crack opening. The compressive strength distribution indicates a higher strength at the centre wall panel, with a higher Young's modulus and a lower Poisson's ratio. Increased cracking has been noted on the right wall panel, corresponding with a lower compressive strength, Young's modulus and a higher Poisson ratio.

The tested material properties have been incorporated into a finite element model of the wall for simulation. The finite element model has been developed as a simplified micro-model, with material properties obtained from non-destructive testing. A quasi-static analysis has been completed on the model for four loading scenarios: an unbraced gable wall with and without applied wind loading, and a braced gable wall with and without applied wind loading. This has described the wall in its current condition and a reconstructed condition. The reconstruction of the roof structure imposes an additional load on the gable wall and increases the Von Mises stress by approximately 15%. However, a decrease of approximately 30% in the total estimated deflection of the gable wall has been noted. This indicates the necessity of reconstructing the roof structure to reduce the risk of further damage to the structure.

The study achieves results through the development of a testing methodology that is unique in the field of conservation of heritage structures in South Africa. The method can be further incorporated to other heritage structures in South Africa to sufficiently describe the mechanical properties and aid in the development of suitable conservation plans.

LIST OF PUBLICATIONS

Title: Non-destructive testing on masonry wall of Non-Pareille manor house, South Africa
Journal: The International Conference on Structural Analysis of Heritage Structures (SAHC2023)
Status: Accepted

Title: Quasi-static analysis of the Non-Pareille manor house gable wall
Journal: South African Institute of Civil Engineering (SAICE)
Status: Submitted

ACKNOWLEDGEMENTS

I would like to express my sincere gratitude to Prof. Kumar Pallav for the guidance and insight provided throughout completing this thesis. His dedication to the research and enthusiasm has been truly inspiring.

I would also like to thank Dr. Mohammed Pourbehi for co-supervising and his help during the finite element model development.

The financial assistance of the Construction Education and Training Authority (CETA) towards this research is acknowledged. Opinions expressed in this thesis and the conclusions arrived at are those of the author and are not necessarily to be attributed to the Construction Education and Training Authority.

Lastly, I am honoured to express my deepest appreciation to my wife, Amy Victor, for supporting me and encouraging me throughout the completion of this thesis.

DEDICATION

This thesis is dedicated to my loving wife, Amy Victor, who has been a pillar of support and my source of inspiration that I so dearly appreciated throughout the process of this research. You have also supported me through the most difficult time following my mother's sudden and unexpected passing. Without you, this would have never been possible.

In memory of my mother, who passed away during the early stages of my research journey. I would also like to dedicate this thesis to Mom and Dad, who taught me never to give up and that I am capable of anything I set my mind to. You have provided me with an educational foundation that can never be replaced.

Mom, you are missed dearly, and your memory will live through all of us.

TABLE OF CONTENTS

Page

LIST OF FIGURES

Page

Body

APPENDICES

LIST OF TABLES

Page

Body

APPENDICES

GLOSSARY

Terms/Acronyms/Abbreviations	Definition/Explanation
μs	Microseconds, 1 x $^{10-6}$ seconds
Adobe bricks	Brick made from compressed earth and organic material
Apartheid	System of institutionalised segregation based on race existed in South Africa until the early 1990s
Conservation	The act of preservation or protection
Corbels	Piece of stone protruding out of a wall to support an element from above
Façade	The front exterior part of a building
Finite element modelling	The development of a numerical 3D model to which structural analysis is subjected to
GDP	Gross domestic product – the measurement of the size of the economy of a country
Heritage buildings	A structure that describes a specific era, culture, person or religion
Holbol	A type of gable in Cape Dutch architecture, concave-convex in outline
Homogeneity	The state of having similar properties through multiple elements
Inversely proportional	Relationship between two parameters as one increases, the other decrease
Lidar Scanning	Laser imaging, detection and ranging – measuring the time between transmission and reflection of a target object
Mesh	Network of interconnected nodes covering a surface
NDT	Non-destructive testing – the measurement of material properties with no damage to the element
NHRA	National Heritage Resources Act 25 of 1999
Photogrammetry	The use of photography to map measurements between objects
Poisson's ratio	The ratio of the proportional change in width to change in length when a force is applied to an elastic element.

Quasi-brittle	An element that exhibits a gradual increase in fracture zones when increased force is applied
Retrofitting	Addition of a component that was not provided during the manufacture
RILEM	Réunion Internationale des Laboratoires et Experts des Matériaux – association providing free access to scientific data relating to construction materials
SAHRA	South African Heritage Resources Agency
Sandcrete	A construction material made from cement, sand (in a 1:8 ratio) and water
Seismic	Relating to earthquakes
Static equilibrium	State of a system where the components are at rest and the resultant force is equal to zero
Structural integrity	The condition where a structural component is fit for purpose
Structural serviceability	The condition where a structure is still deemed useful
TIN mesh	Triangular Irregular Network – used to create a mesh to describe a surface
Transducer	Device that converts a signal from one form of energy to another
Truss tie	Member in a truss to prevent the rafters from pushing outward
Ultrasound tomography	The graphical representation of the ultrasound imaging/test results
UNESCO	The United Nations Educational, Scientific and Cultural Organization
World Heritage Trust International Union for Conservation of Nature	International, a non-governmental organisation, providing the World Heritage Committee with technical information regarding heritage structures
Young’s modulus	The measure of the stiffness of an elastic material

Chapter 1 INTRODUCTION

This chapter introduces the specific field of study. The background to the research is presented, followed by a description of the research problem. The objectives and expected outcomes are elaborated, and the research methodology is explained. Finally, the outline of the thesis is shown to provide an overall description of each chapter.

1.1 Background and motivation

Humankind has built structures throughout history, ranging from monuments to functional buildings. These structures provide an identity to the cultures of each specific era, essentially showing glimpses of how people have evolved in the use of technology and how tribute was paid to persons of interest, various religions and historical events. Heritage buildings provide continuity in history and cultural identity to a country's population. With the rapid development in architecture, conserving heritage structures is of utmost importance to retain the history and character captured in these structures. The United States initiated the idea of cultural conservation in *1965* with the *World Heritage Trust*. It was accompanied by similar proposals by the *International Union for Conservation of Nature* and presented to the United Nations Conference on the Human Environment. Today, culturally significant historical sites are protected by the *United Nations Educational, Scientific and Cultural Organisation* (UNESCO) with an international treaty accepted by *UNESCO* in 1972, called the Convention Concerning the Protection of the World Cultural and Natural Heritage (World Heritage Convention). Examples of protected heritage buildings include the Cathedral of Notre Dame in France, the Acropolis in Greece, the Taj Mahal in India and the Kremlin in Russia.

Heritage buildings in South Africa are protected under the *National Heritage Resources Act 25* of 1999 (NHRA). The significance of the heritage sites is grouped into three grades: *Grade I: Heritage resources of exceptional significance in a national viewpoint; Grade II: Heritage resources with significance to a specific province or region; and Grade III: Other significant heritage resources*. The heritage sites grouped in these gradings are managed nationally by the South African Heritage Resource Agency (SAHRA), provincial and local authorities, respectively. Examples of heritage buildings under the administration of SAHRA include the Castle of Good Hope in Cape Town, Robben Island (also declared a World Heritage site by UNESCO in 1999), the Union Buildings in Pretoria and Dal Josafat in Paarl (SAHRA, n.d.). During a meeting held on 5 March 2020 with the Built Environment Unit of SAHRA, concerns were raised about the general state of the heritage structures and the lack of conservation regarding the structural integrity of the heritage resources in South Africa.

Heritage buildings worldwide are subject to ageing and material degradation. Although built in ancient times, these heritage structures exhibit enhanced workmanship and structural expertise, with ages far exceeding the original design life (Riggio, D'Ayala, Parisi and Tardini, 2018). Environmental factors such as climate change, high rainfall, extreme temperature fluctuations, air pollution, and acid rain, coupled with human interference such as vandalism and a general disregard for the built environment, contribute to the ultimate destruction of heritage structures worldwide and South Africa (Cavalagli, Kita, Castaldo, Pisello and Ubertini, 2019; Pacheco-Torgal, 2014).

Although currently in decline, the tourism industry contributed to 2.7% of South Africa's GDP and provided jobs for 4.5% of the country's employed population in 2018, with the South African heritage having a direct contribution (Statistics SA, 2019). The rich heritage of South Africa captured in monuments and buildings is a crucial asset to the country’s economy, increasing tourism and providing jobs. Hence, a suitable approach is essential in determining the in-situ mechanical properties of the structural elements of South African heritage buildings compared to the in-depth structural analysis of the aforementioned elements.

1.2 Research problem

Heritage structures have seen continuous degradation from exposure to natural elements for an extended time and human interference. As a result, the preservation of heritage structures has received increased attention from researchers worldwide. Literature has indicated success in determining the mechanical properties of heritage structures through non-destructive testing. Such examples include the UPV testing of the Cathedral of Reggio Emilia, Italy, conducted by Casarin, Valluzzi, da Porto and Modena (2007) and the combined UPV testing, rebound hammer testing and modelling of the Sacred Heart of Jesus Cathedral in Algiers, Algeria, conducted by Merzoug, Chergui and Cheikh Zouaoui (2020). However, severely limited literature is available on determining mechanical properties by testing and assessing the current state of heritage structures in a South African context.

1.3 Research questions

- What is the distribution of mechanical properties (compressive strength, Young’s modulus and Poisson’s ratio) on the selected historical masonry wall?
- How are the results from testing incorporated into the finite element model?
- What does the finite element model indicate about the current state of the wall?

1.4 Objectives and outcomes

This research aims to conduct in-situ testing and structural analysis on a masonry wall of a heritage structure. For the study to be successful, the following objectives must be met:

- Identify cracking on the old masonry wall through visual inspection and its measurement through non-destructive testing.
- Conduct non-destructive testing on the masonry wall to estimate the current mechanical properties.
- Perform finite element modelling with the measured mechanical properties to develop a stable and accurate model of the old masonry wall.
- Graphically display the stress distribution and simulated deflections of the old wall.

Following this research, the current state of the wall has been described through testing and modelling. Further, the prepared model can be used for future restoration work. The expected outcomes are as follows:

- The identified crack patterns will provide a visual representation of the current state of the wall.

- The distribution of the mechanical properties of the old masonry wall is plotted over the wall dimensions, further describing the current state of the wall. This data is incorporated into finite element modelling.
- A finite element model has been developed using the tested mechanical properties. This model will provide an accurate base for conducting structural simulations.
- The behaviour of the masonry wall will be evaluated under gravity load and further increased theoretical loads to determine possible failure modes.

1.5 Significance

Heritage structures provide a great sense of pride to many cultures, telling a story about the history of humanity. Since ancient times, these structures have been built and subjected to many forms of degradation, such as environmental hazards and human interference, with some structures ultimately destroyed. South Africa's continued conservation of heritage structures is lacking due to the expertise and resources required, leading to the severe degradation of historical monuments and heritage buildings. Therefore, it is essential to test these structures to develop conservation plans and restore heritage structures to continue the story of South Africa's cultural history for generations to come.

1.6 Delineation

This research focuses on material testing (non-destructive testing) and structural analysis, with a critical focus on the Masonry wall of Dal Josafat under gravity load. It includes the challenges in South Africa regarding the decay of heritage structures while excluding the methods of structural restoration and development of restoration materials. No dynamic study will be performed on the wall.

1.7 Methodology

The research will be conducted based on experimental testing and computer-aided analysis to fully determine the material properties and assess the masonry wall's behaviour. The work is divided into two segments, i.e., experimental testing and structural analysis. The field test includes visual inspection, rebound hammer and ultrasonic pulse velocity testing. The results from the experimental testing will be incorporated into finite element analysis.

The significant heritage site, as prescribed by SAHRA, is the fire-damaged farmhouse of Dal Josafat, Paarl. A visual inspection will be undertaken to identify the site-specific information and the significant masonry wall to be tested. Visual damage – such as cracking, water ingress, settlement, material degradation and fire damage – is identified. Further, rebound hammer and ultrasonic pulse velocity testing are done to determine surface-level compressive strength, Poisson's ratio and Young's modulus. Calibration of the results is done through laboratory testing. The obtained material properties are incorporated into a finite element model to accurately represent the old masonry wall.

1.8 Organisation of thesis

Chapter 1: INTRODUCTION
A general introduction to the thesis is provided in this chapter, introducing the focus of the research. The background to the study and the study's significance are provided, continuing with the research objectives and outcomes, providing the motivation for this specific study.

Chapter 2: LITERATURE REVIEW & THEORY
This chapter elaborates on the theory obtained from previous scientific literature related to certain aspects of the current study. Literature relating to the non-destructive testing of masonry walls and finite element modelling has been investigated and described in this chapter. The previous research literature provides data on which the study is based and indicates research gaps, providing areas for further research.

Chapter 3: RECONNAISSANCE SURVEY
The masonry wall to be studied is introduced in this chapter. A reconnaissance survey is introduced, where the masonry wall is studied concerning the topography, the position of the wall in relation to the overall structure and visual damage to the wall.

Chapter 4: NON-DESTRUCTIVE TESTING
The data obtained from the reconnaissance survey is incorporated into this chapter. The non-destructive testing methods are introduced and described. The data extraction methodology is described by which the model will be developed.

Chapter 5: FEM MODEL OF MASONRY WALL
The results obtained from non-destructive testing are analysed and incorporated into a FEM model. The software used and the modelling method is described, as well as the expected outputs. The validation of the model undertaken in comparison with the visual inspection will be described.

Chapter 6: RESULTS & DISCUSSION
All the raw data extracted from non-destructive testing and the FEM model are introduced in Chapter 6. The results are grouped and interpreted using various calculations to determine the material properties throughout the masonry wall. These properties are used to develop the model, and the output results are described. The results are shown graphically, and the damage model is compared to the visual inspection. In conclusion, the results are discussed and interpreted to describe the current mechanical state of the masonry wall.

Chapter 7: CONCLUSIONS & RECOMMENDATIONS
The conclusions are drawn from the results and the discussion. The conclusion revisits the outcomes and objectives from Chapter 1 to determine if the research is successful. Recommendations are offered to encourage further study related to this topic.

Chapter 2 LITERATURE REVIEW & THEORY

The finite element modelling of old masonry structures and elements has been researched through past literature, discussing the requirements to create the model and the results that can be expected. Various available test methods have been investigated, elaborating on the efficiency of using old masonry elements. This chapter focuses on previous literature related to the current study, discussing various elements that contribute to heritage masonry testing and analysis.

Past literature indicates various methods for developing a finite element model by assuming the material properties (Annecchiarico, Portioli and Landolfo, 2010) or conducting non-destructive testing to determine actual material properties to incorporate in the model (Kumar and Pallav, 2020). This chapter investigates various literature to identify a research gap in the current field and to develop a suitable approach for conducting the current research. Each element related to the experimental study has been researched to effectively formulate a suitable research method and provide a foundation with which the results can be compared.

2.1 Introduction

Heritage structures are becoming degraded worldwide, and intervention is required to protect the history of various cultures. In developing countries, particularly South Africa, research into the conservation of heritage structures is required to improve the current condition of the local heritage. This section provides a brief literature review of specific measures to evaluate structural integrity and estimate heritage structures' design life. Structural testing is discussed to assess the mechanical properties, with structural analysis providing data on the serviceability of the masonry wall.

2.2 Non-destructive testing on heritage structures

The determination of the mechanical properties of structural elements is evaluated through destructive testing or non-destructive testing (NDT). Destructive tests are conducted with lab-testing machines such as compressive, tensile and flexural strength tests. These tests are based on the principle of specimen failure.

Non-destructive testing examines materials to determine certain properties without causing damage or reducing their future usefulness (Verma, Bhadauria and Akhtar, 2013). In heritage structures, any damage to testing areas must be negligible. Non-destructive testing is therefore performed with minor to no damage to the specimen. This contrasts with destructive testing, which tests the mechanical properties by destroying the specimen. Destructive testing is more suitable in the manufacturing field of structural components.

In-situ testing of structural elements, particularly effective on existing structures, is preferred over random sampling required for destructive testing. Non-destructive testing methods include pull-out tests, rebound tests, penetration tests, dynamic tests, and radioactive testing (Verma et al., 2013). These methods are further described in the following sections. Non-destructive testing aims to determine a structure’s condition by comparing another structure or computational analysis, ranking or comparing the structure with existing conditions, and comparing the properties of the structure to a certain threshold (Breysse, Klysz, Dérobert, Sirieix and Lataste, 2008). The researcher also describes the combination of various non-destructive tests to improve the accuracy of results by minimising the limitations of a single non-destructive test.

A review of various non-destructive test methods and the appropriate testing equipment is discussed in the following section. Visual inspection, rebound hammer testing and ultrasonic pulse velocity testing are discussed in detail due to their relevance to the current study.

2.2.1 Non-destructive testing methods

Non-destructive testing is a practice that has been in existence for centuries. Although no precise dates can be linked to its origin, skilled workers estimated the overall condition of machines and structures by analysing the shape for deformations and inspecting the elements for imperfections and cracks. Today, visual inspection is still utilised as a preliminary survey of existing structures.

During World War II, many technological advances were made to equipment being used in the present day. Since then, advances have included more straightforward tests like concrete rebound hammer tests to more advanced ultrasonic and radiographic testing. This is especially true with non-destructive testing from a mechanical perspective. Various non-destructive test methods and their possible applications are described in Table 2.1.

Table 2.1: NDT methods with respective applications (International Atomic Energy Agency, 2002)

Test Method	Application	Time	Cost	Data Quality	Properties
1. Visual Inspection	Looking for any visual damage	Rapid	Low	Dependent on the experience of the engineer	Visual imperfections
2. Half-cell electrical potential method	Testing for the possibility of corrosion	Rapid	Low	Unable to indicate the rate of corrosion	Reinforcement corrosion
3. Schmidt/ rebound hammer test	Surface hardness testing	Rapid	Low	Influenced by surface conditions	Compressive strength
4. Carbonation depth measurement	Diagnosis of reinforcement corrosion	Rapid	Low	Influenced by aggregate colour	Moisture penetration
5. Permeability test	Water ingress potential	Slow	Low	Results can only be indexed	Permeability
6. Windsor probe test	Surface hardness test	Rapid	Low	Affected by coarse aggregate	Compressive strength
7. Cover meter testing	Cover distance measurement	Slow	Low	Affected by large cover	Provides depth of reinforcement
8. Radiographic testing	Void detection	Rapid	High	Complex interpretation	Sub-surface imperfections
9. Ultrasonic pulse velocity test	Density and compressive strength test	Rapid	Moderate	Affected by moisture and reinforcement	Compressive strength, Poisson's ratio and modulus of elasticity

Test Method	Application	Time	Cost	Data Quality	Properties
10. Impact echo testing	Void and delamination detection	Rapid	Moderate	Complex interpretation	Sub-surface imperfections
11. Ground-penetrating radar	Detection of reinforcement bars and voids	Rapid	Low	Complex interpretation	Sub-surface element detection
12. Infrared thermography	Detection of multiple defects	Rapid	Moderate	Affected by environmental conditions	Sub-surface imperfections

Determining structural integrity is important for heritage structures with the absolute minimisation of visual and structural damage. Hence, the test methods of visual inspection, rebound hammer test and ultrasonic pulse velocity test are discussed in this paper.

2.2.2 Visual inspection

The visual inspection of the structural element, and the earliest test method classified as non-destructive testing, rely on the technician's expertise to visually classify the condition of a structure prior to conducting more sophisticated tests. Visual features of importance are related to workmanship, deterioration, and visible damage, focusing on cracking, spalling, delamination, blemishes, weathering or a lack of uniformity. The visual features can provide extensive information regarding the general condition and which testing methods can be employed to provide the most accurate results. Coupling the visual inspection of the relevant structure with any of the surrounding environment, neighbouring structures and climatic conditions can significantly improve the reliability of the overall inspection.

Kulkarni and Admane (2015) compiled a visual inspection method which includes obtaining the architectural and structural plans of the structure to be evaluated. If no plans are available, a professional or the researcher must create new plans. After familiarisation with the plans, inspections are done from the foundation regarding settlement, with evidence on masonry walls indicating possible settlement. Masonry walls, masonry columns, concrete columns and beams are inspected for cracking and spalling. Photographic evidence of the visual defects is collected with a field report describing the defects and possible causes. An informed decision is made on which testing methods are most suitable for the in-depth testing of the structural elements.

Tampone and Ruggieri (2016) studied visual imperfections of ancient timber roof structures in Italy. In one such example, the researcher found substandard fastening of a truss tie at Villa Demidoff, Florence, as shown in Figure 2.1.

Figure 2.1: Substandard fastening of a truss tie (Tampone and Ruggieri, 2016)

Such bracing of a damaged truss member is a recurring example in Italy, primarily undertaken in the 18th and 19th centuries. The practice entails the wrapping a damaged timber element with bands of flat, wrought iron sections and fastening these bands to the beam with many nails. The longitudinal splitting of the beam indicates an undersized beam thickness or substandard protection against weathering. As such, the strapping of the member serves no long-term purpose in strengthening the damaged member and lowers the aesthetic appeal. The solution requires more advanced methods, serving a structural purpose and aesthetically preserving the historical value, such as applying resistant members at the lower edge of the tie. Slotting the tie to hide tensioning cables can increase the member's overall strength while keeping the element's face unchanged.

Masonry is an ancient construction material that has evolved throughout history, one example being adobe bricks. Adobe bricks consist of compressed unfired earth combined with natural fibres commonly used in ancient construction. While modern structural use of adobe bricks is limited, ancient adobe structures are found in various parts of the world, including Southern Europe, East Mediterranean, North Africa and South Asia. These historical structures constitute a great part of cultural heritage worldwide. Illampas, Silva, Charmpis, Lourenço and Ioannou (2017) studied the effect of clay-based grout injections on an adobe model building after conducting a field inspection of existing structures. The researcher found that, due to the low tensile strength and quasi-brittle nature of adobe bricks compared to modern clay bricks, adobe structures are particularly vulnerable to cracking damage (Figure 2.2).

Figure 2.2: Cracking of a structure in Cyprus built with adobe bricks (Illampas et al., 2017)

The cracks disrupt the structural continuity, increasing movement in the element and reducing overall stiffness, accelerating the damage. Previously, repairs had been done to these structures with mortar injections or the retrofitting of timber or steel elements, leading to a much stiffer element than originally. The increased stiffness causes increased stress concentrations, possibly leading to further structural damage. The researcher developed a suitable material with similar properties as the existing adobe bricks to be used as a repair material, with success in restoring the original strength parameters of the structure, while maintaining the appearance similar to the original.

Robben Island, South Africa, is classified as a UNESCO World Heritage site due to its significant contribution to its cultural heritage as a prison, hospital and military base between the 17th and 20th centuries. In the late 20th century, Robben Island was employed as a maximum-security prison until the dawn of democracy and victory over the oppression of Apartheid (UNESCO, n.d.). With the progression of time, the structures have endured constant damage, and the need for intervention has escalated. Loke, Pallav and Haldenwang (2019) studied the sustainable repair of historic masonry elements at Robben Island. With recent repairs, it is evident that modern materials and methods are incompatible with the construction materials used originally, as evidenced by the detachment of the new mortar from the original surface shown in Figure 2.3.

Figure 2.3: Repairs done with incompatible material at Robben Island, causing further damage (Loke et al., 2019)

The visual inspection of the site provided significant evidence of the incompatibility between the materials. The researcher followed the steps to classify the existing mortar according to its physical properties. This classification serves as a basis for further study to develop a suitable mortar, following the existing classification, which can prove useful in repairing the historical building to extend its service life significantly.

Visual inspection, beneficial when conducted by a suitably experienced researcher, can offer various insights into the construction methods by identifying the era in which a structure was built and the architectural influences in the construction. This links the material and structural properties and research into similar structures. Kumar and Pallav (2020) studied the senate hall of Allahabad University in Prayag, India, through visual inspection, non-destructive testing and finite element modelling. The senate hall, an unreinforced masonry structure constructed in 1915 with architectural influences from Hindu and Muslim cultures, is an example of Indo-Saracenic architecture. Visual inspection provided valuable insight into determining the structural and non-structural components within the structure.

The architectural influences have been identified, with the arches and domes linked with Muslim architecture and the pillars and corbels linked with Hindu architecture. The visual inspection identified the openings, arches, columns and dimensions. This is critical in determining the test positions and developing a 3D model of the structural element. The material was also visually identified as a combination of masonry and stone arches (Figure 2.4).

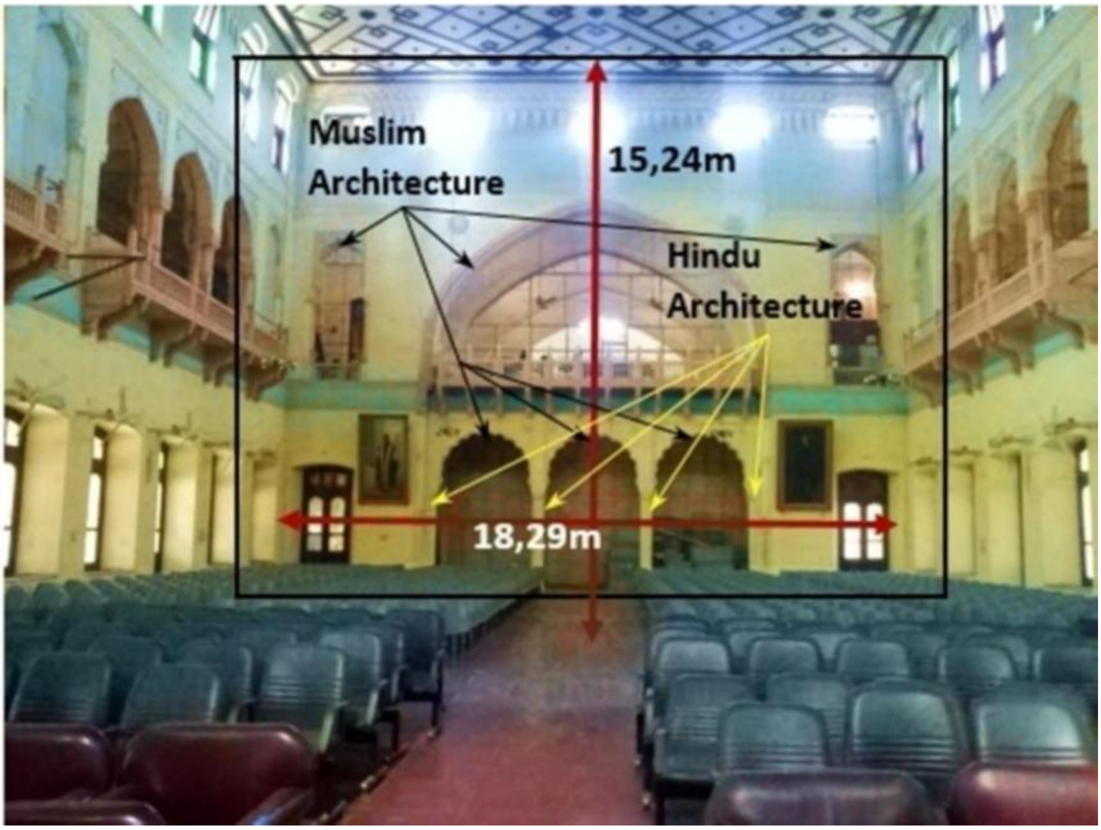

Figure 2.4: Measurements and features of the internal masonry wall of the senate hall, Allahabad University (Kumar and Pallav, 2020)

The initial visual inspection at the senate hall of Allahabad University provides a significant foundation upon which the corresponding studies can be built. Adapting the data to the current research, the visual inspection has provided information on the crack patterns, breakouts in masonry units from the wall and possible horizontal movements within the old masonry wall. Visual inspection serves as a viable benchmark in determining the accuracy of the finite element model.

Visual inspection is practised worldwide in various fields of structural engineering. In the field of heritage structures, visual inspection serves as a preliminary inspection, providing extensive information regarding the general condition and testing methods for the most accurate results.

2.2.3 Schmidt/rebound hammer testing

The Schmidt rebound hammer, developed by Swiss engineer Ernst Schmidt, is a non-destructive test method to determine the surface hardness of an element. The test method relies on the principle of striking an elastic mass on the surface being tested, with the rebound of said elastic mass being dependent on the hardness of the surface. The rebound hammer results in a rebound number, a dimensionless value that can be correlated to compressive strength.

Although the rebound hammer is a relatively simple and inexpensive method of testing surface hardness, it has significant limitations, namely: (1) the hammer must be used on a smooth surface, or the surface must be smoothed by sanding; (2) the specimen tested must be fixed and rigid, limiting movement; (3) testing done on old surfaces must be correlated with other test methods; (4) surface moisture can influence the rebound number; (5) different types of coarse aggregate provide slight variations in results; (6) the type of cement has an influence on the rebound number; and (7) high carbonation depths on concrete surfaces can produce a higher rebound number (International Atomic Energy Agency, 2002). The limitations of the test method reduce the reliability of the results obtained on elements from a heritage structure. Hence, combining the rebound hammer with other non-destructive test methods is essential. The general testing procedure of the rebound hammer is shown in Figure 2.5.

Figure 2.5: Rebound hammer test procedure (Rebound hammer test on concrete, 2018)

The rebound hammer consists of a plunger, instrument body, internal mass, impact spring and scale, or a digital display. The test procedure and the components are shown in Figure 2.6.

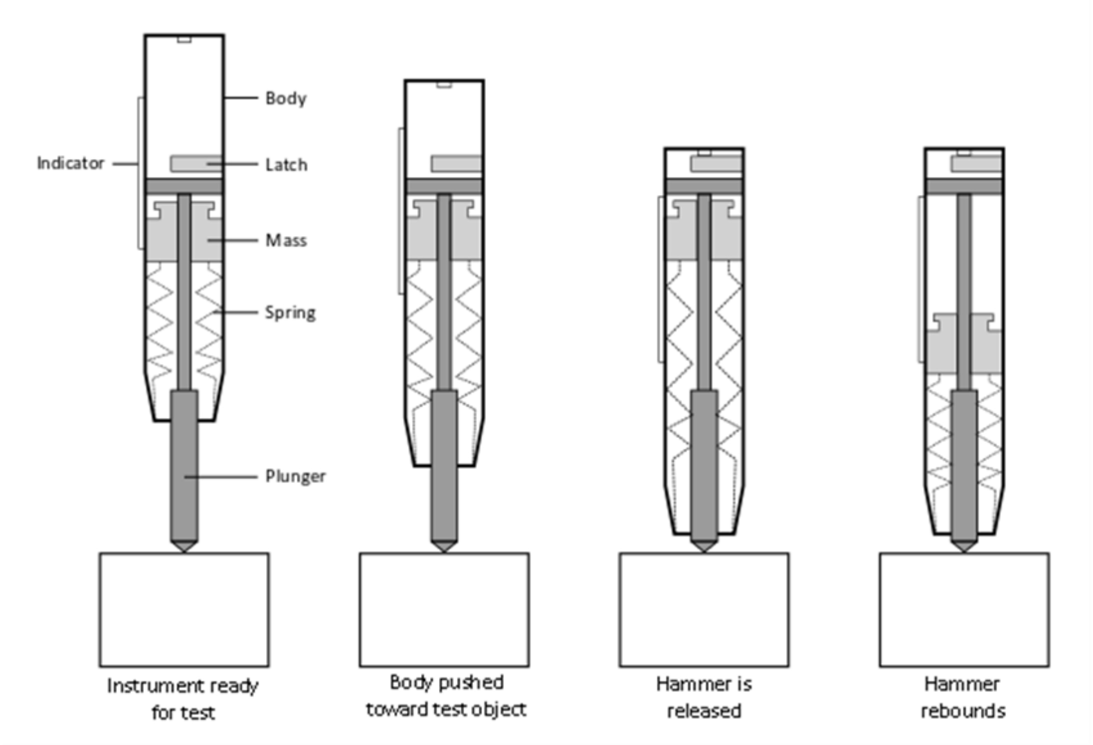

Figure 2.6: Visual representation of the rebound hammer test procedure (Engineersdaily, 2011)

The correlation between the rebound number and compressive strength is shown graphically in Figure 2.7. The graph considers the angle of testing on the surface.

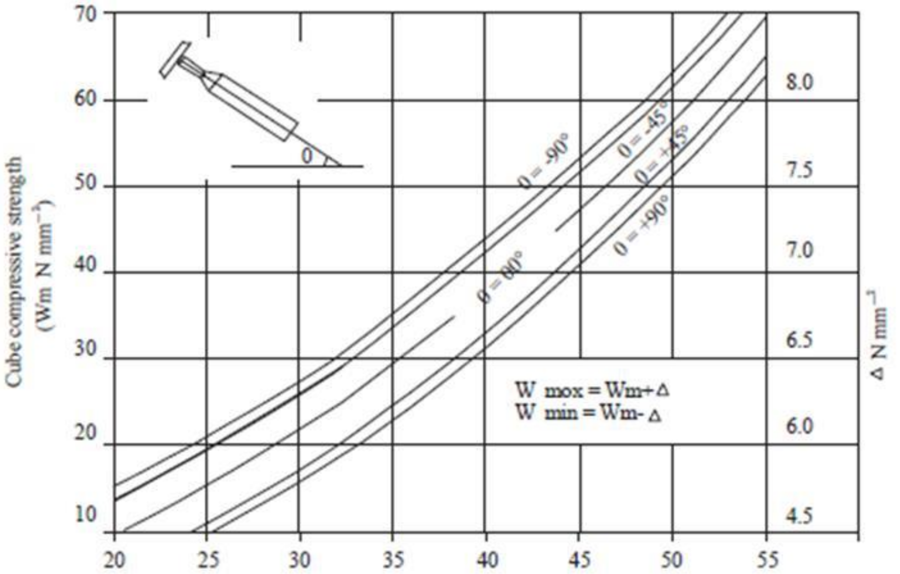

Figure 2.7: Correlation of rebound number to compressive strength (Nnaji, Amadi and Molokwu, 2016)

Jiao, Xia and Shi (2019) performed a non-destructive inspection of the Anyuan Miners' Club lecture hall in China. An initial visual inspection identified the areas of interest displaying significant damage. The structure was analysed with a rebound hammer for brick strength testing, a penetration test for determining the mortar strength, total station to determine the deflection of elements, moisture content testing and stress wave timing to determine internal timber decay.

A total of 10 test areas were identified, and 10 bricks in each area were selected randomly for testing. Five test points were used for each brick, and the average rebound number was used to determine the compressive strength of the brick. This ensures an even spread of results through the overall tested element.

Russo (2017) studied the structural integrity of monumental structures using non-destructive testing. A Buddhist Temple in Bagan, Myanmar, was studied by using the rebound hammer. The researcher noted that the study is not focused on the quality of the data produced but instead, aims to produce rapid test results that can be interpreted to conclude the structure's overall integrity.

Samples were collected to conduct lab tests compared with the in-situ testing. Tests were conducted on panels that were visually noted as damaged and undamaged to draw the comparison. The rebound hammer test was conducted on five positions for each brick. The comparison found that the rebound hammer produced higher results than the lab testing, although still consistent with the trends produced by lab testing. The researcher noted that the results are still reliable in estimating the structure's integrity; however, combining methods will produce more accurate results.

In an African perspective, Nnaji et al. (2016) studied the mechanical properties of sandcrete (mortar with low binder content, yellow-white colour) and concrete walls in Nigeria deteriorating under biological growth. Two hundred buildings were studied, with ages ranging from less than

10 to 50 years. Rebound hammer readings were taken at various positions on the wall, with an average of 15 readings used to determine the rebound index for the specific test position.

The researcher found that the rebound numbers decreased in walls affected by biological growth. This indicates the solubility of cementitious material in the presence of biological growth, reducing the bond between aggregates.

Kumar and Pallav (2020) conducted rebound hammer testing on the internal masonry walls of the senate hall of Allahabad University, India. The tests were conducted at selected positions in a 4x4 grid, producing 16 readings at each position. Additional rebound hammer tests were compared with compressive strength tests done in a laboratory on masonry samples. Comparing the rebound number and the compressive strength of masonry samples in a laboratory allows for a direct correlation between the test results and the sample's compressive strength with specific material properties.

A linear equation is developed to describe further the correlation between the rebound number and the compressive strength of the specific material. The results are graphically demonstrated to provide a global correlation for the masonry elements, as shown in Figures 2.8 and 2.9.

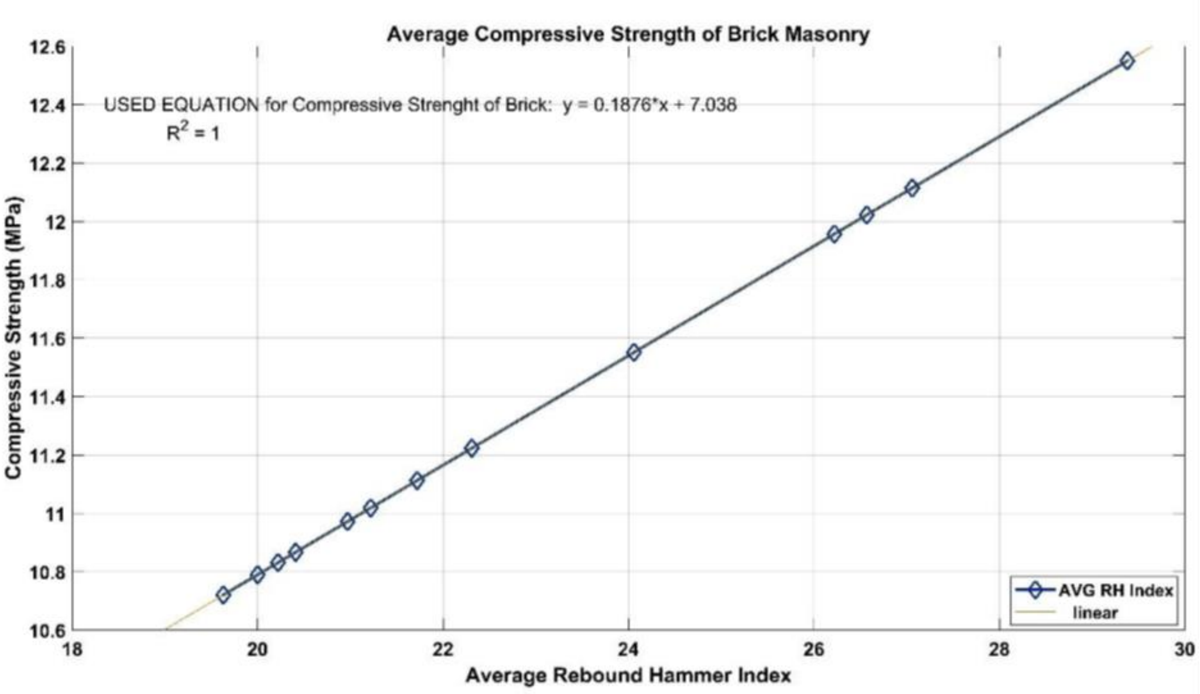

Figure 2.8: Correlation of the rebound number with the compressive strength of brick masonry (Kumar and Pallav, 2020)

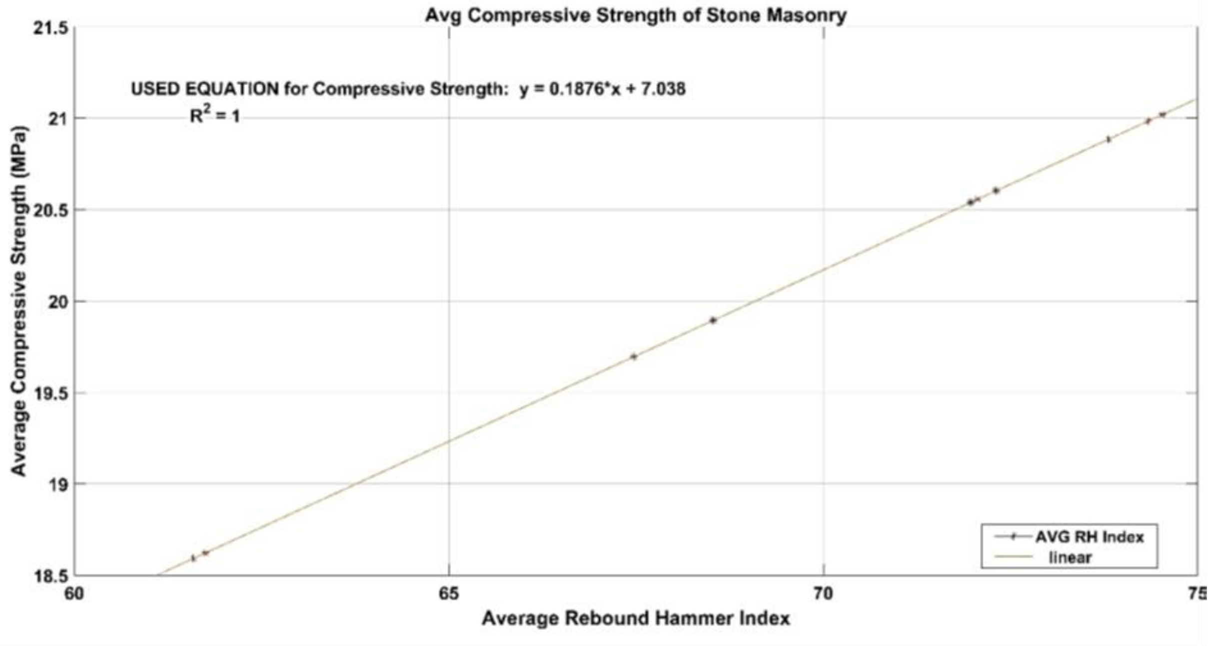

Figure 2.9: Correlation of the rebound number with the compressive strength of stone masonry (Kumar and Pallav, 2020)

Eljufout, Hadadin, Haddad and Alhomaidat (2022) evaluated limestone walls using the rebound hammer. Typically, the compressive strength of building bricks is determined through destructive testing. For existing structures, semi-destructive testing is conducted through core extractions. This poses the problem of conservation when historical structures are to be tested, as damage to the structure needs to be minimal. The authors built full-size limestone wall models using traditional construction methods, with limestone material obtained from various regions in Jordan. In-situ testing was conducted on the models with the rebound hammer, and the samples were subjected to crush testing. This produced a direct comparison between the rebound number and the compressive strength of the specific material. The correlation is shown in Figure 2.10.

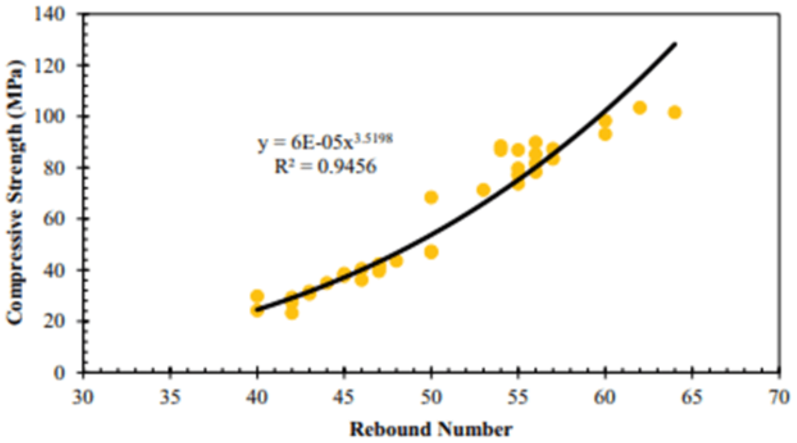

Figure 2.10: Rebound number and compressive strength correlation (Eljufout et al., 2022)

The correlation between the rebound number and the compressive strength is material-specific, and calibration is required for other construction materials (Brencich, Bovolenta, Ghiggi, Pera and Redaelli, 2020). According to Brencich et al. (2020), certain drawbacks exist when conducting rebound hammer tests. A limited area is hit by the plunger, thus producing a localised result. In certain instances, difficulty can be experienced in smoothing the test surface due to irregularities in the concrete mix, affecting results. Results are also affected by local irregularities such as voids.

The reliability of the rebound hammer test is questionable when used as the sole method of determining the mechanical properties of concrete or masonry. Past studies have indicated success in determining structural elements' surface hardness; however, more reliable results have been obtained when used in conjunction with other test methods for comparison (Atoyebi, Ayanrinde and Oluwafemi, 2019).

In the current research, rebound hammer testing has been conducted on the old masonry wall to determine the surface hardness of the masonry units. The results have been combined with the ultrasonic pulse velocity to improve the accuracy of the data, which has been calibrated through laboratory testing and incorporated into finite element modelling.

Rebound hammer testing is a simple test to determine the surface hardness of concrete or masonry. However, the test instrument does not provide a direct result of the compressive strength but rather a rebound number. This rebound number is then correlated to compressive strength. Various studies have shown rebound hammer testing to be effective in evaluating heritage structures, but similar studies from a South African perspective are scarce.

2.2.4 Ultrasonic pulse velocity testing

Ultrasonic pulse velocity (UPV) testing consists of transmitting pulses of longitudinal waves passing through the element of interest, with the waves produced by an electro-acoustic transducer (International Atomic Energy Agency, 2002). The transmitted pulse is passed through the element, reflecting off discontinuities and changes in material, developing a complex system of stress waves. The waves pass through the element towards the receiving transducer, converting to an electrical signal processed through the test equipment’s timing circuit. The transit time of the pulse is measured, and the pulse velocity is calculated as per Equation 1.

$$V = \frac{l}{t} \tag{1}$$

where:
$V =$ Ultrasonic wave velocity in km/s
$l =$ measured length in mm
$t =$ measured time in µs

UPV testing is useful in evaluating the quality and homogeneity of structural elements, measuring changes occurring in the element over time, estimating the element's strength after correlation with the pulse velocity, and determining the modulus of elasticity and dynamic Poisson's ratio of the element.

The general principle in assessing the quality of a structural member through UPV testing is analysing the pulse velocity. The pulse velocity will be higher for higher quality, indicating good density, homogeneity and uniformity. In contrast, poorer quality will produce a lower pulse velocity. In the presence of a discontinuity, the pulse will pass around the discontinuity instead of through it, increasing the path length and resulting in higher measured time. Commonly a transducer operating within 20 kHz to 150 kHz is used. The higher frequency (up to 150 kHz) is used for shorter path lengths up to a maximum of 500 mm, whereas the lower frequency of 20 kHz is used for path lengths of more than 1500 mm (IS 13311-1(1992), 1992).

UPV testing can be done using three transmission methods: direct, semi-direct or indirect. For direct transmission, the receiver is placed on the tested element at the opposing surface from the transmitter. Direct transmission is the most common method of UPV testing and provides the highest accuracy and therefore, the recommended method where possible. Semi-direct transmission requires the transmitter and receiver to be placed at 90º surfaces on the element to be tested. For indirect transmission, the transmitter and receiver are arranged on the same surface (Aydin, 2013). The test method can be expanded to develop an ultrasound tomography, which is described in the literature by Akoglu, Kotoula and Simon (2020). The transmission methods are shown in Figure 2.11.

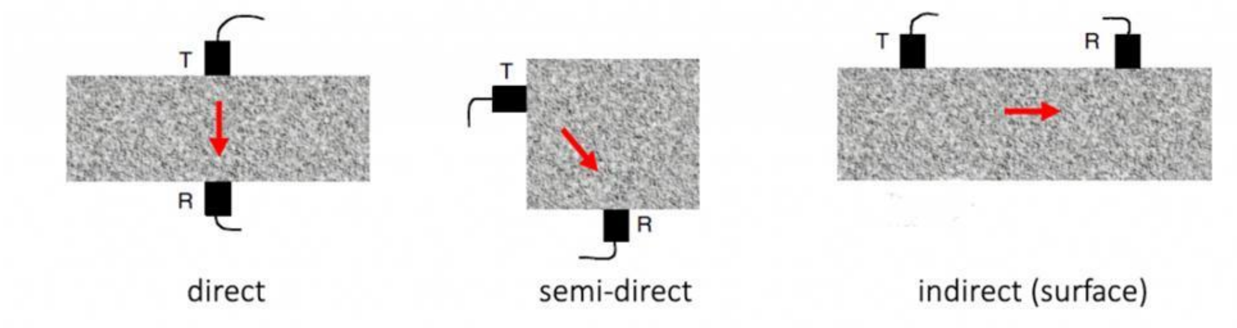

Figure 2.11: UPV transmission methods (Ultrasonic Testing of Concrete, 2021)

Azam, Riaz, Haq, Shihata and Zawam (2022) studied the compressive strength of fired clay bricks based on the results obtained from ultrasonic pulse velocity testing. Testing was done on a 100-year-old masonry structure, and the results were correlated with compressive strength tests on masonry samples in a laboratory. The authors developed a suitable method for conducting rapid in-situ UPV tests to determine the old structure's compressive strength of the clay bricks. In determining Poisson's ratio and the dynamic Young's modulus of a historical structural element, UPV testing proves useful in determining said properties.

Rao, Sravana and Rao (2016) investigated the relationship between the compressive strength and Young’s modulus of roller-compacted concrete. The authors conducted laboratory testing on concrete cube specimens through ultrasonic pulse velocity tests and cube crushing. An empirical equation has established a relationship between the compressive strength and Young’s modulus. This empirical equation provides the data to determine the compressive strength of similar materials through rapid UPV testing.

Kumar and Pallav (2020) investigated an internal masonry wall of the senate hall at Allahabad University, India, by conducting various test methods, including UPV. A fixed path length of 0.5 m was selected, and the testing was done with direct and indirect transmission to determine the compressive and shear wave velocity. Using these values, Poisson's ratio and the dynamic Young's modulus were determined using masonry and stone material density, respectively, as shown in Figures 2.12 and 2.13.

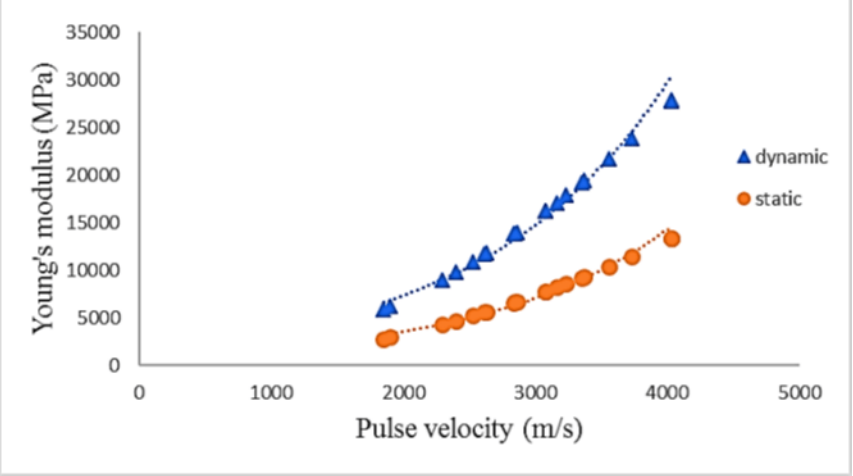

Figure 2.12: Comparison of static and dynamic Young's modulus of masonry through UPV Testing (Kumar and Pallav, 2020)

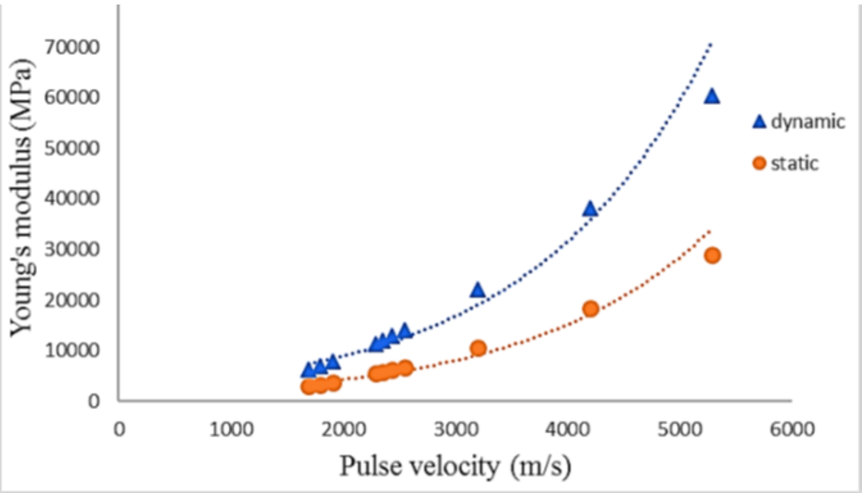

Figure 2.13: Comparison of static and dynamic Young's modulus of stone through UPV Testing (Kumar and Pallav, 2020)

The combined results from UPV testing and rebound hammer testing can be incorporated into finite element modelling to accurately simulate the behaviour of the structure.

Akoglu et al. (2020) studied ultrasound tomography, which was developed following UPV testing in the United States of America to monitor memorials in the Grove Street Cemetery, New Haven, Connecticut. The study aimed to develop a simple and cost-efficient methodology for determining tombstone deterioration. The cemetery's significance is evident in its social and cultural history. The two tombstones are shown in Figure 2.14.

Figure 2.14: Trowbridge Angel Memorial (left) and Howell marble memorial (right) (Akoglu et al., 2020)

Researching the cemetery’s conservation ensures that the history will not be lost as time progresses. The researcher produced 3D renderings of each memorial tombstone, visually mapping the results of the UPV testing. The rendering of the Trowbridge Angel Memorial is shown in Figure 2.15.

Figure 2.15: Trowbridge Angel Memorial model mapping by UPV testing (above) and the damage mapping by visual inspection (below) (Akoglu et al., 2020)

The 3D models of the memorials were measured through photogrammetry. This scanning method relies on detailed and high-resolution photographs taken of the subject from various angles. Using specialised software, control points on the subject are selected to match all photographs. These photographs are imposed onto each other to match the control points. The software analyses the data and produces a model based on these photographs. Photogrammetry is a cost-effective method of developing 3D models from more complex shapes compared to more sophisticated scanning methods such as Lidar scanning. Manual measurements can provide sufficient accuracy for simpler models, like a masonry wall. However, photogrammetry lacks accuracy when compared with Lidar scanning.

Ultrasonic tomography consists of UPV testing at known coordinates on the element, with tests various directions determining the velocity for all areas not easily accessible by direct measurement. The results are entered into tomography algorithm software to calculate the ultrasound paths and respective velocities, producing tomograms detailing the element's structural integrity.

Analysing the results of UPV testing, Young's modulus of elasticity can be calculated with Equation 2.

$$E = \frac{\rho(1+\mu)(1-2\mu)}{1-\mu} V^2 \tag{2}$$

where:
$E =$ Young's modulus of elasticity in MPa
$\mu =$ Poisson's ratio
$V =$ pulse velocity in m/s
$\rho =$ density in kg/m³

The Indian Standard IS 13311 (Part 1): 1992 defines the criteria to classify the quality of the structural element. The grading criteria are shown in Table 2.2.

Table 2.2: IS 13311 (Part 1): 1992 UPV grading criteria (IS 13311-1(1992), 1992)

Ultrasonic Pulse Velocity Grading Criteria		
No.	Pulse Velocity (km/s)	Quality Grading
1.	Over 4.5	Excellent
2.	3.5 – 4.5	Good
3.	3.0 – 3.5	Medium
4.	Less than 3.0	Poor

If UPV testing returns poor quality, further testing might be recommended.

Casarin et al. (2007) studied the Cathedral of Reggio Emilia, Italy, and the San Zeno Basilica bell tower in Verona, Italy, to conduct non-destructive testing for condition monitoring of cultural heritage buildings. The researcher conducted UPV testing on various masonry panels of the structures. Although visual defects have been noted, the UPV testing returned results indicating material with good overall mechanical characteristics, seldom producing poor results. It is also noted that the UPV testing in isolation could not provide significant reliability and would need to be coupled with other non-destructive testing methods.

In Africa, little research is available on non-destructive testing in determining the structural integrity of historical or heritage structures. In one such study, the researcher studied the structural integrity and stability of the Sacred Heart of Jesus Cathedral in Algiers, Algeria (Merzoug et al., 2020). The researcher conducted UPV, rebound hammer testing and analysis through the finite element method (FEM). The structure was built in 1956 according to modern architecture; the Sacred Heart of Jesus Basilica is an architectural monument with state-of-the-art structural concrete members.

Algiers and the surrounding areas have experienced devastating earthquakes from 1359 to 2014 (National Geophysical Data Center, nd.). The seismic activity in the area provides a significant basis for the research. The results obtained from UPV and rebound hammer tests were correlated with ISO strength curves produced by RILEM TC 043-CND: Combined non-destructive testing of concrete (Figure 2.16).

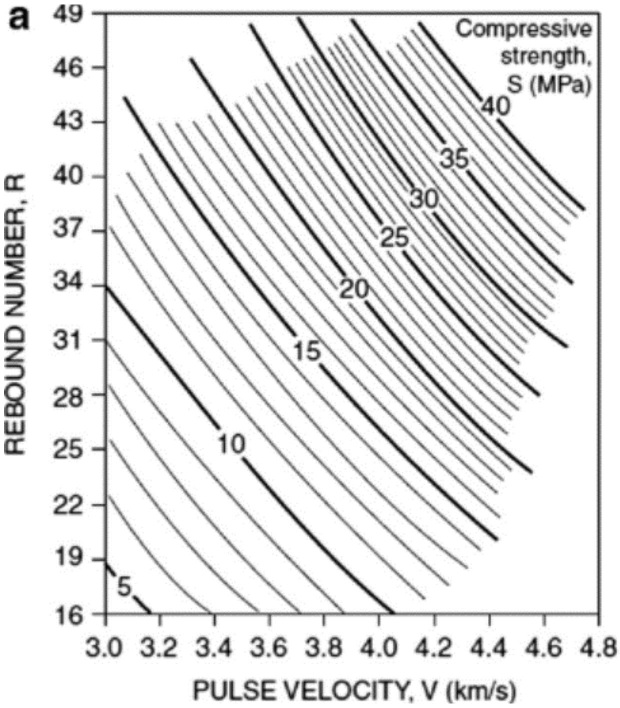

Figure 2.16: ISO strength curves produced by RILEM (Alwash, Breysse and Sbartaï, 2015)

Ahn, Kim, Sim, Shin and Shin (2017) reviewed various ultrasonic non-destructive test methods to determine the depth of a crack in the cementitious material. Using UPV testing equipment, two measurements are taken over the crack, as shown in Figure 2.17.

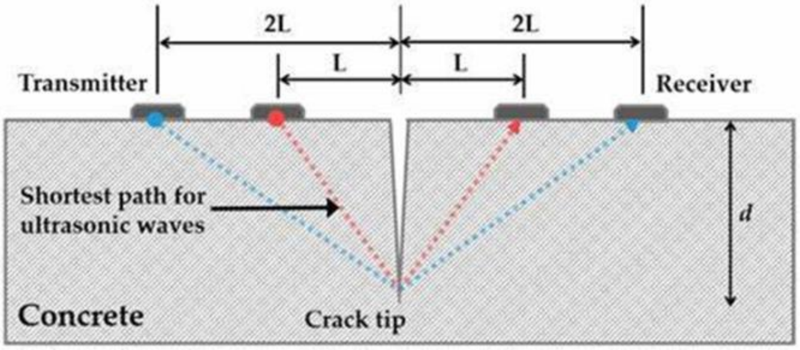

Figure 2.17: Crack depth measurement through UPV testing (Ahn et al., 2017)

The time measurement obtained is used to obtain the crack depth using Equation 3.

$$d = \sqrt{\frac{4{t_L}^2 - {t_{2L}}^2}{{t_{2L}}^2 - {t_L}^2}} \tag{3}$$

where:
$d =$ crack depth
$t =$ measured time for length L or L2

For the current research, ultrasonic pulse velocity has been conducted following rebound hammer testing. The results have been interpreted to calculate Young's modulus and Poisson's ratio, which has been further incorporated into the finite element model.

UPV testing provides valuable data on heritage structures' internal defects and material properties. With the limited research on UPV testing available in Africa, more significantly in South Africa, future research is necessary.

South Africa has seismic activity to a lesser degree; historical buildings and monuments are experiencing decay due to environmental factors and human interference such as vandalism and theft. Performing non-destructive testing on historical structures will introduce a proactive approach to conserving the heritage instead of focusing on remedial methods.

2.3 Analysis of heritage structures

Masonry elements exhibit complex structural behaviour under load with plastic deformation and tensile cracking. Heritage masonry structures, subjected to loads for many years, require urgent rehabilitation and technical assessments to produce accurate rehabilitation plans. Therefore, an extensive analysis is essential to determine the stability of heritage structures and assess the extent of current damage through static and dynamic analysis (Binda, Saisi and Tiraboschi, 2000). Various analysis methods are available, with examples including limit state analysis, linear elastic analysis, thrust line analysis and finite element analysis.

Limit state analysis is useful for structural design, where structural stability is achieved when the resisting forces are higher than the acting forces. This method's limitation is evident in the evaluation of old materials where unorthodox behaviour is expected. The linear elastic analysis, effectively describing the internal stresses of structural elements, is commonly used to analyse reinforced concrete or steel elements. The method is severely limited when analysing masonry due to the non-linear behaviour under stress. Thrust line analysis effectively analyses structures where stability is the determining factor of failure. Therefore, it is useful for analysing arches. However, the application on an old masonry wall is insufficient to provide accurate results compared with other analysis methods.

Finite element analysis, a numerical method to analyse a given element, can be performed in various fields, with structural engineering necessary in the current study. Finite element analysis is based on matrix analysis of structures, and due to the complexity of most calculations, the problems are solved with computer software.

Finite element analysis consists of modelling the structural element to be analysed with all material properties provided, developing partial differential equations and solving the partial differential equations through matrix calculations with the known end conditions of the structural elements.

Kujawa, Lubowiecka and Szymczak (2020) analysed a 14th-century church in Gjonewo, Poland, through finite element analysis. Each element was modelled with the respective material properties, and the full structure could be analysed with FEM software. The whole church was modelled using 3D scans, providing a macro-model of the structure. The model is developed using Abaqus FEA; the parts are shown in Figure 2.18.

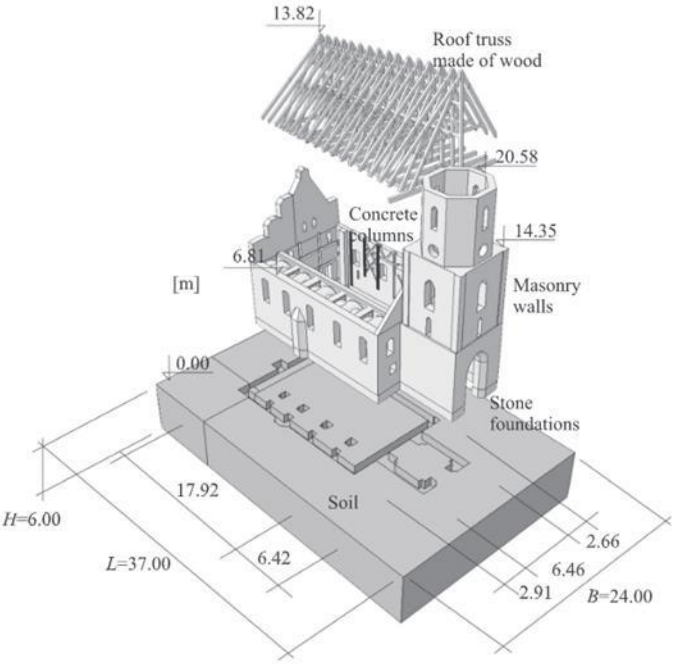

Figure 2.18: Model development of the 14th century church in Gjonewo, Poland (Kujawa et al., 2020)

The developed model has been analysed under gravity loads with completely restrained boundary conditions at the structure base. The mesh has been generated as 4-node tetrahedral elements, namely C3D8 elements. Approximately 3.5 million finite elements exist within the model, with parameters set to perform each analysis case within 24 hours. This limitation is introduced as large models with a high-density mesh can lead to impractical processing times.

The crack patterns obtained through the finite element analysis have been compared with the visual cracks on the structure, and the crack patterns on the west-south walls and the east wall have been shown in Figures 2.19 and 2.20, respectively.

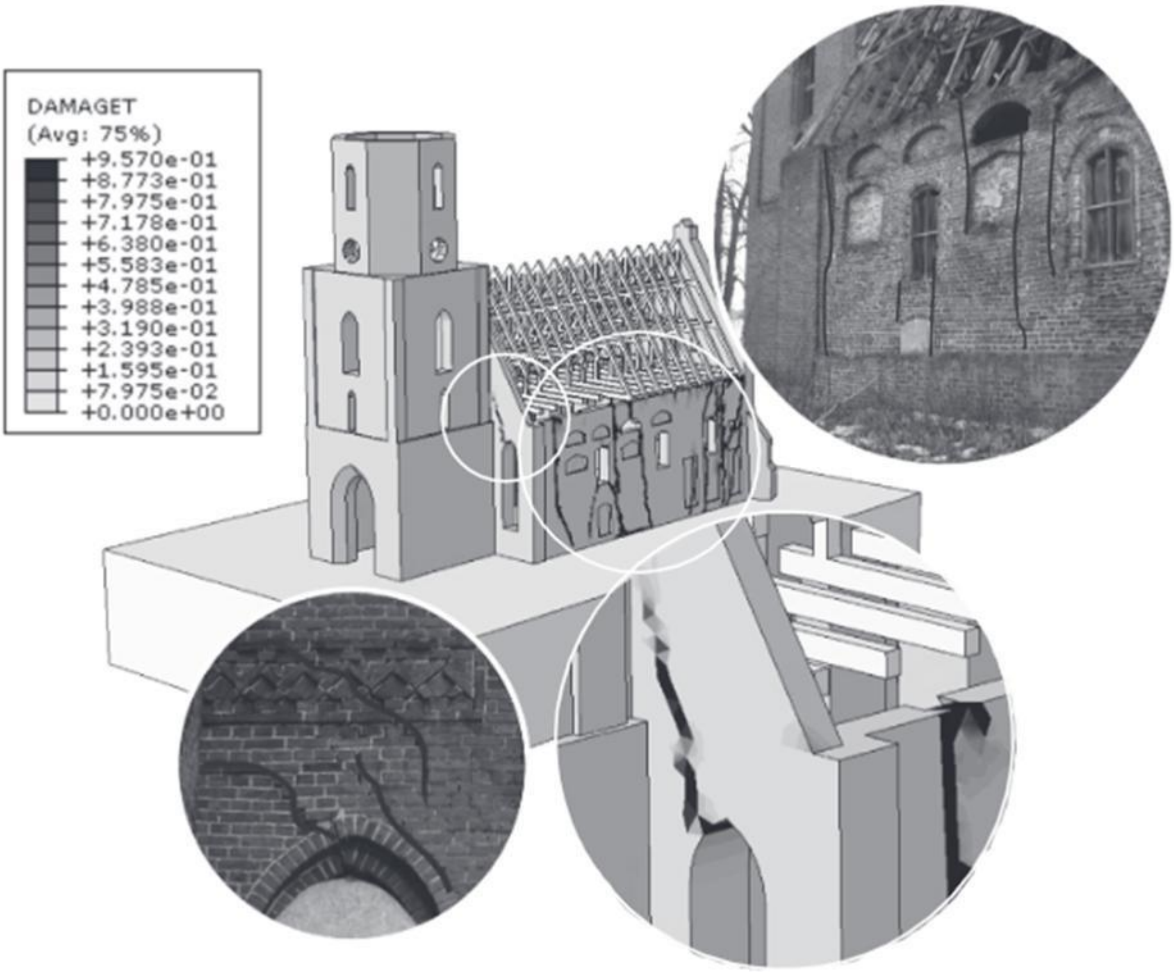

Figure 2.19: Main cracks on the west-south wall compared with photographic data (Kujawa et al., 2020)

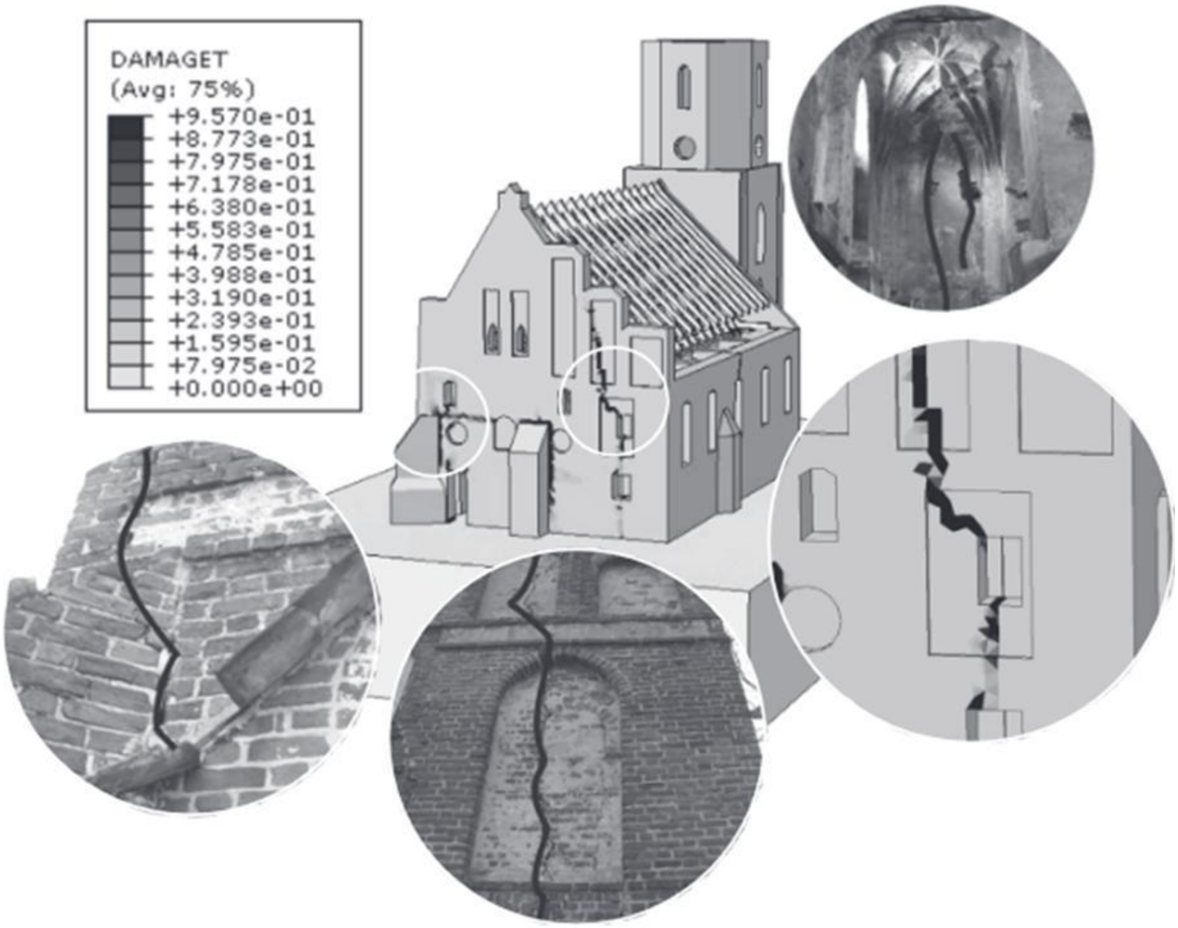

Figure 2.20: Main cracks on the east wall compared with photographic data (Kujawa et al., 2020)

As seen in Figures 2.19 and 2.20, finite element modelling has produced accurate results comparable with actual data. Although finite element modelling requires extensive processing power, it can analyse complex structures that would otherwise prove near impossible with other analysis methods.

Finite element analysis produces extensive results for masonry structures that are difficult to replicate with other analysis methods. Detailed analysis through FEM is essential for heritage masonry, as unorthodox material properties and construction methods can influence results.

2.4 Finite element modelling of heritage structures

FEM is a powerful tool to simulate the structural behaviour under different loading scenarios and estimate the structural stability with future loads. Masonry, especially old masonry, has been shown to exhibit complex behaviour and can be subjected to various failure modes. This section discusses the modelling process, different modelling types and their influence on FEM results and accuracy. Macro-modelling and micro-modelling are introduced and described, and different mesh techniques are defined.

2.4.1 Model definition

A macro-model assumes that the masonry wall to be analysed is a single element with homogeneous material properties. The wall is divided into nodes into which a mesh is created, allowing deflections within the single element. A macro-model does not take the masonry-masonry interface or the masonry-mortar-masonry interface into account – instead, it relies on the mesh to produce possible deflections or failure planes within the element.

Developing the masonry wall as a macro model is advantageous by simplifying the analysed element and reducing the required processing power. The results produced by the macro-model will, however, be less accurate when compared to a similar micro-model, as the macro-model disregards failure modes on the contact planes between the brick units.

The macro-model shown in Figure 2.21 indicates the lack of detail in the model, where all internal material differences and discontinuities are ignored.

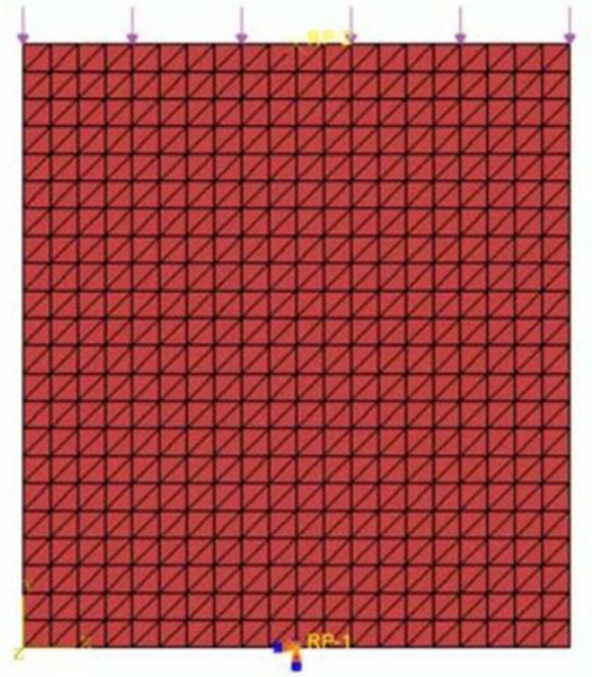

Figure 2.21: Macro-model mesh of a masonry wall panel (Annecchiarico et al., 2010)

A micro-model is developed by independently modelling each masonry unit and the mortar bond. This creates a masonry-mortar-masonry interface where separate material properties are defined for the masonry and the mortar. These individual units, or parts, are combined to form the final masonry wall model. Each part in the wall is divided into nodes, and a mesh is developed, with the boundaries of the mesh not extending past the part boundaries.

Micro-modelling has the disadvantage of having higher processing requirements due to the complexity of the model but has the advantage of being more accurate. Failure can occur within masonry units or through the mortar between the masonry units, provided that the model has been sufficiently defined. The interface between the masonry units and the mortar is defined, and results can be obtained to accurately describe real masonry walls scenarios.

Investigating Figure 2.22 below, the micro-model includes more detail. The mesh for the mortar and the masonry elements are included in the micro-model.

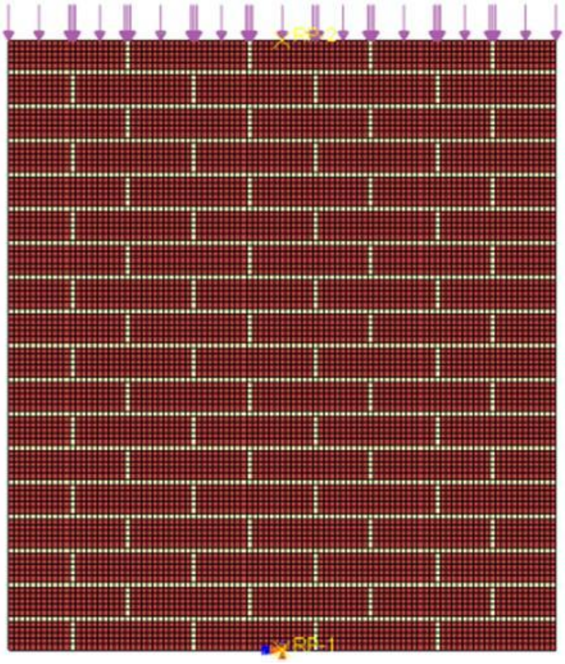

Figure 2.22: Micro-model mesh of a masonry wall panel (Annecchiarico et al., 2010)

The simplified micro-model is based on the micro-model, where the masonry units are modelled independently. However, for the simplified micro-model, the mortar is excluded. The interface is defined between each mortar unit, and the material properties of the mortar are irrelevant. The nodes are created within the masonry units, and the mesh is generated within each masonry unit, with the mesh boundaries not extending past the part boundaries.

Simplified micro-modelling requires less processing power than micro-modelling but is more intensive than macro-modelling. The simplified model can still provide accurate results where the masonry material properties are unknown. Failure can occur within individual masonry units or on the masonry-masonry interface, as shown in Figure 2.23.

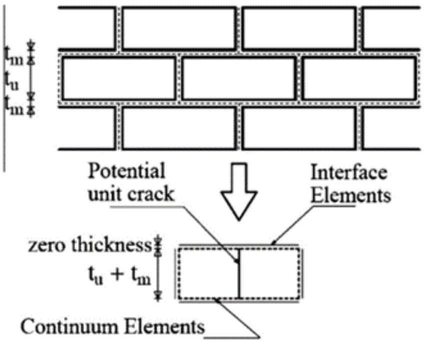

Figure 2.23: Simplified micro-model interface (Bolhassani, Hamid, Lau and Moon, 2015)

The masonry units shown in Figure 2.23 are modelled to include the mortar. The thickness of the mortar, t_m, is assumed to be zero, and the masonry unit is modelled to include the thickness of the mortar, therefore having a thickness of $t_u + t_m$.

Each model definition has advantages and disadvantages, and the suitable definition is chosen based on the characteristics of the application. Macro-modelling and micro-modelling are described in more detail in the following section.

2.4.2 Macro-modelling

Macro-modelling of masonry structures is based on the assumption that the element is homogeneous, and the masonry-mortar interface is assumed insignificant. The masonry joints and units are assumed to be continuous materials for analytical purposes. This significantly reduces the number of individual elements to be analysed, resulting in a less time-consuming method reducing the requirement for computational resources.

Macro-modelling is useful in large-scale applications where small, detailed interactions of the elements are insignificant and smaller mesh elements require significantly higher processing power. Saloustros, Pelà, Cervera and Roca (2017) studied the macro-modelling of a large-scale application in the form of a multi-storey masonry wall. The model was developed to obtain accurate crack patterns using separate mesh patterns. The modelled wall is shown in Figure 2.24 below.

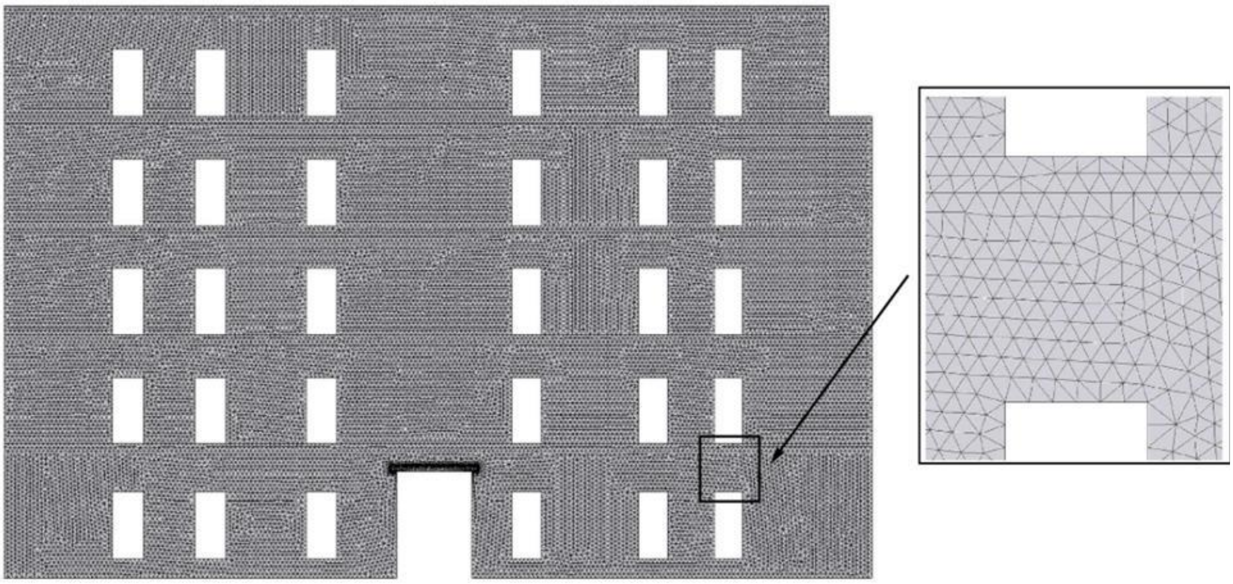

Figure 2.24: Macro-model of large masonry wall (Saloustros et al., 2017)

The researcher has developed a dense model to create accurate crack patterns, as a finite model will only provide stress values per mesh face. Therefore, a denser mesh will produce a finer stress distribution, indicating accurate positions for possible crack patterns. The model was structured by adjusting the mesh configuration to orientate in horizontal, vertical and diagonal angles, as shown in Figure 2.25.

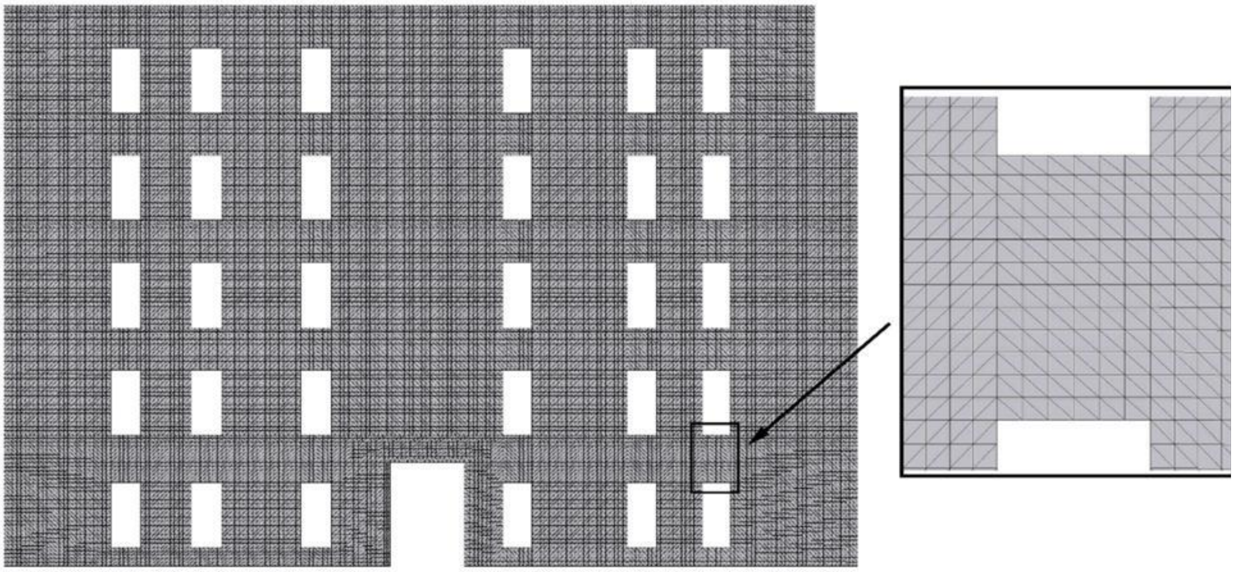

Figure 2.25: Structured macro-model of large masonry wall (Saloustros et al., 2017)

The crack patterns developed using both models are shown in Figure 2.26 below.

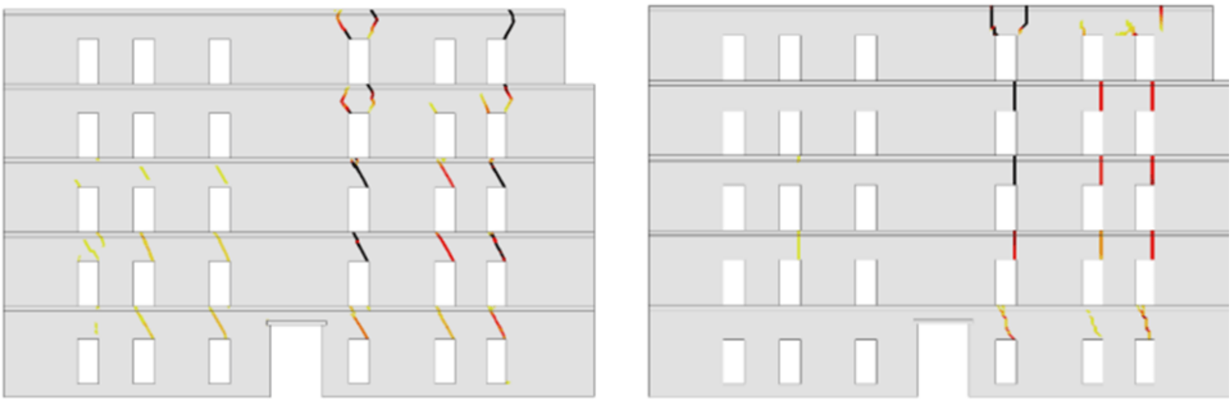

Figure 2.26: Maximum principal stresses in unstructured masonry wall (left) and structured masonry wall (right) (Saloustros et al., 2017)

The crack tracking algorithm used by the researcher has proven to be suitably accurate for both mesh types. However, slight changes in crack patterns are evident between the structured and unstructured mesh.

D'Altri, Milani, de Miranda, Castellazzi and Sarhosis (2018) analysed a historic masonry leaning tower through macro-modelling, namely the leaning tower of Caerphilly Castle, South Wales, which has been in a ruined and leaning condition for centuries. The tower is shown in Figure 2.27.

Figure 2.27: Artist drawing of the leaning tower of Caerphilly Castle (left) and modern photos of the tower (middle and right) (D'Altri et al., 2018)

The tower’s geometry was measured through independent research by Prizeman, Sarhosis, D’Alri, Whitman and Muratore (2017) using a FARO Focus 3D X130 laser scanner. The 3D scan was integrated into the study conducted by D'Altri et al. (2018), and a finite element mesh was developed. The mesh was generated using a macro-modelling approach. The TIN mesh produced by the laser scanner is shown in Figure 2.28, and the finite element mesh is shown in Figure 2.29.

Figure 2.28: TIN mesh of the leaning tower developed from the laser scanning (D'Altri et al., 2018)

Figure 2.29: Finite element mesh superimposed on the TIN mesh of the leaning tower (D'Altri et al., 2018)

The mesh has been developed as a tetrahedron shape with triangular interfaces. A tetrahedron can provide a 4-node first-order element or a 10-node second-order element, described as C3D4 and C3D10 elements, respectively. The mesh element and the interface are described in Figure 2.30.

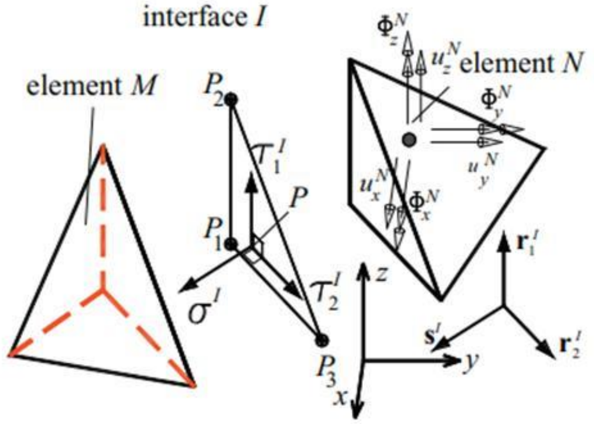

Figure 2.30: 4-node tetrahedron elements M and N with the interface I as a triangular plane (D'Altri et al., 2018)

The model is assumed to be homogeneous, and the analysis is completed on the entire model, where the interface provides total fixity between the mesh elements.

The analysis was completed by incorporating limit states into the finite element model. This method provides absolute limits where failure will occur within the structure through collapse. The model is assumed to be completely fixed at the base, with gravity and self-weight as the loads on the model. From the model, a hinge point was selected at the corner of the base, with the base being the tilting plane. The overall inclination of the structure has been increased until collapse occurs. The actual and limiting inclination have been graphically expressed in Figure 2.31.

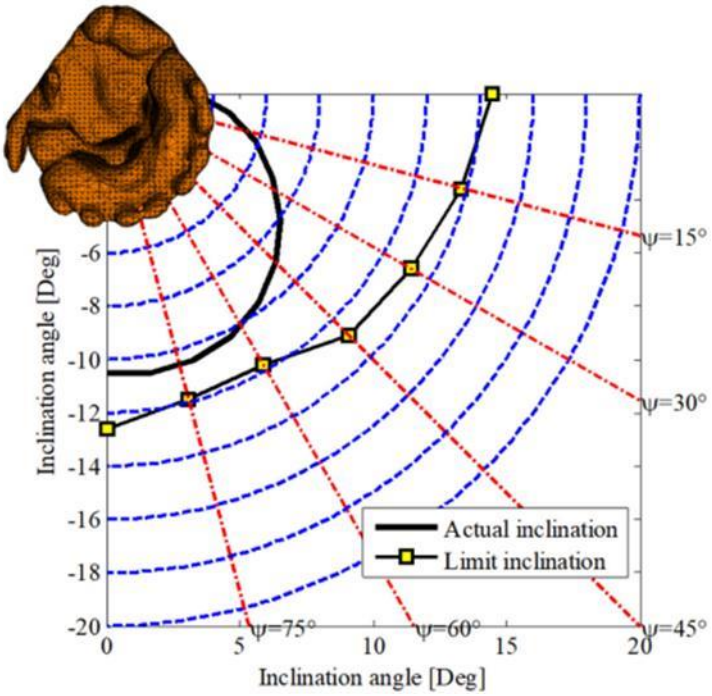

Figure 2.31: Actual inclination and limiting inclination at various horizontal angles of the rocking direction (D'Altri et al., 2018)

As shown in Figure 2.31, the structure is close to collapse. At an angle of 75° of the rocking direction, a further 1.5 degrees will lead to collapse. The model has also indicated the plane where the structure is predicted to fail. The possible collapse mechanism is shown in Figure 2.32.

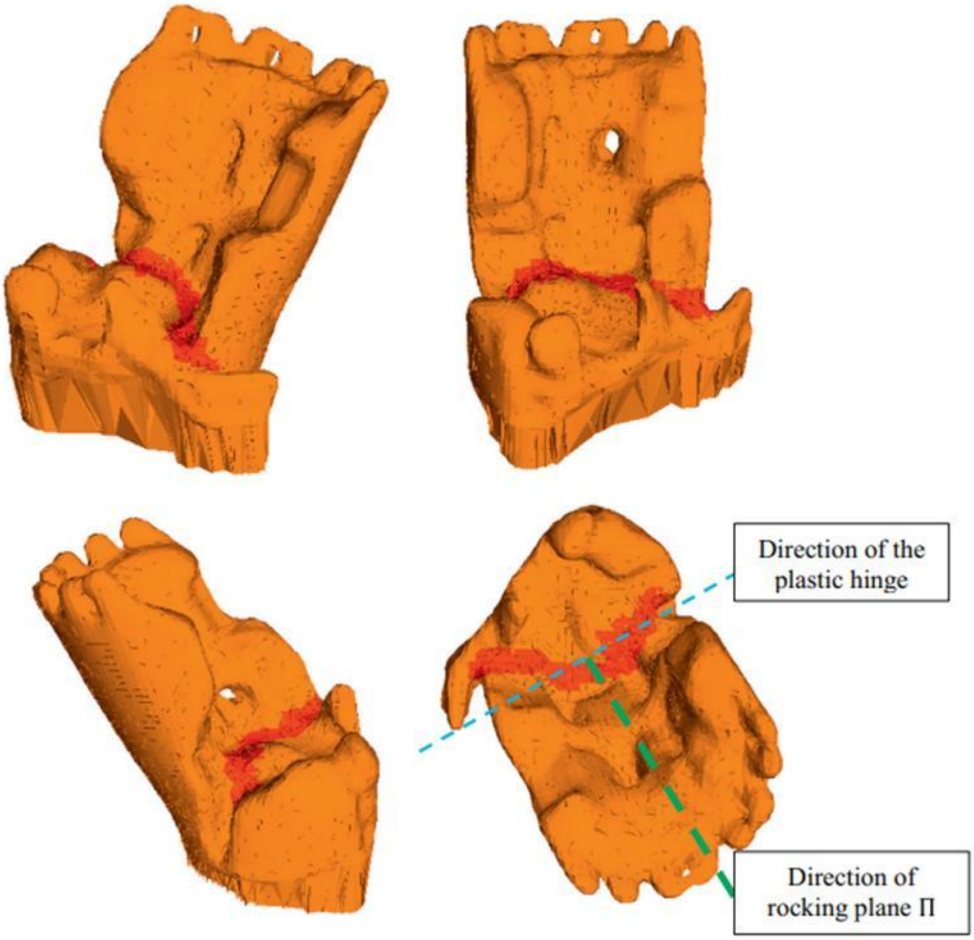

Figure 2.32: Collapse mechanism indicating the plastic hinge where failure is expected to occur (D'Altri et al., 2018)

Merzoug et al. (2020) followed a similar modelling technique to analyse the Sacred Heart of Jesus Cathedral in Algeria. Macro-modelling was conducted in this study by using automatic meshing software that treats the model as homogeneous.

The Sacred Heart of Jesus Cathedral, constructed in 1956, is regarded as a revolutionary work of modern-day architecture and engineering using concrete as a building material. Due to the complex geometry of the cathedral, the experience was required for the design and construction. The Perret Freres Company successfully bid to construct the cathedral, given their experience with constructing Église Notre-Dame du Raincy (Church of Notre Dame in Raincy, France).

The Algiers region and surrounding areas have a history of seismic activity, with several recent devastating earthquakes with a magnitude of more than 6.0 on the Richter scale, resulting in a high number of fatalities and damage to structures. Therefore, testing and analysing a monumental structure such as the Sacred Heart of Jesus Cathedral was essential. The cathedral is shown in Figure 2.33.

Figure 2.33: The Sacred Heart of Jesus Cathedral in Algeria (Merzoug et al., 2020)

The researcher studied this structure by conducting non-destructive testing on the base columns and finite element modelling on the superstructure. The finite element modelling was done using Robobat, currently known as Autodesk Robot. Rebound hammer testing and ultrasonic pulse velocity testing are undertaken as non-destructive testing.

The superstructure has been modelled as shell elements based on historical plans of the structure and archive data of the construction materials used. The shell mesh element is shown in Figure 2.34.

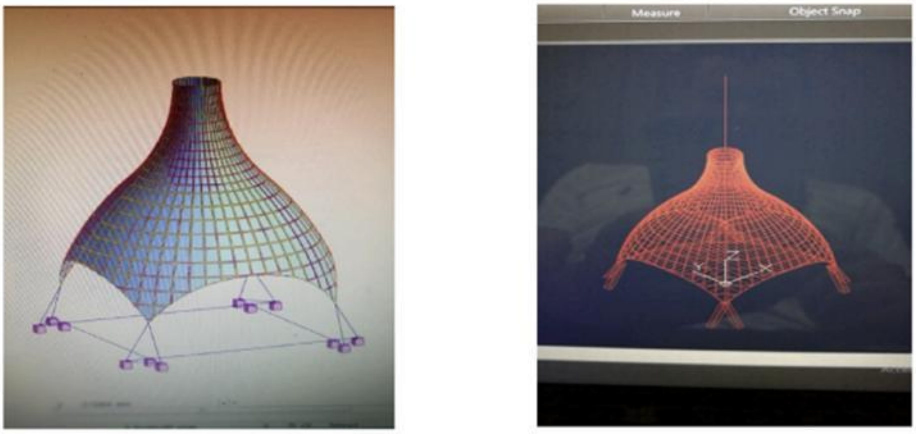

Figure 2.34: Finite element model of the Sacred Heart of Jesus Cathedral (Merzoug et al., 2020)

Measured the current structural state of the support columns through non-destructive testing, the researcher determined that the concrete used during construction is of high quality with an average compressive strength of 36 MPa, providing a sound basis for the prediction of the future stability of the structure.

The finite element model has been subjected to self-weight and seismic activity. The structure is fully fixed at the bottom of the column supports, and the floors have rigid characteristics. It was found that inter-storey drift occurs in both directions. However, the resultant forces and stresses remain within the allowable ranges according to the Algerian seismic design code (Merzoug et al., 2020).

2.4.3 Micro-modelling

Micro-modelling of masonry structures is described as the detailed and separate modelling of the masonry units, including the mortar and the masonry-mortar interface. This modelling method provides a detailed simulation of the behaviour of individual masonry units in the overall element on a small, micro-scale. Micro-modelling requires more powerful computational resources and can be time-consuming due to the complexity of myriad elements. However, the data produced from the model showcases the behaviour of the masonry structure in greater detail and accuracy.

Annecchiarico et al. (2010) conducted experimental research to compare the differences between macro- and micro-modelling of a masonry wall, following up on experimental research by Lourenço, Rots and Blaauwendraad (1995). The wall, with fixed dimensions 1000 mm high and 990 mm wide for both scenarios, has been modelled as a single, homogeneous element for a macro-model and as a wall consisting of individual masonry units with mortar between each unit as a micro-model. Both models have been subjected to the same loads, and the material properties for each model are assumed. The loading of the wall model has been done according to the experimental research of Lourenço et al. (1995), as shown in Figure 2.35.

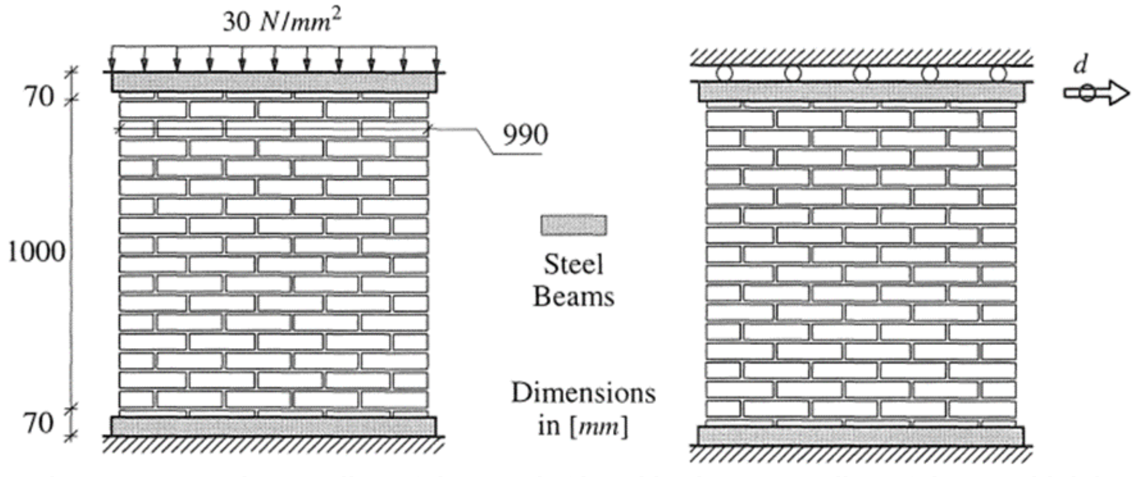

Figure 2.35: Vertical loading of the wall (left) and horizontal loading of the wall (right) (Lourenço et al., 1995)

Following the development and analysis of the model using Abaqus FEA, the principal stresses in the macro- and micro-model have been determined. The results for the macro- and micro-model are shown in Figures 2.36 and 2.37, respectively.

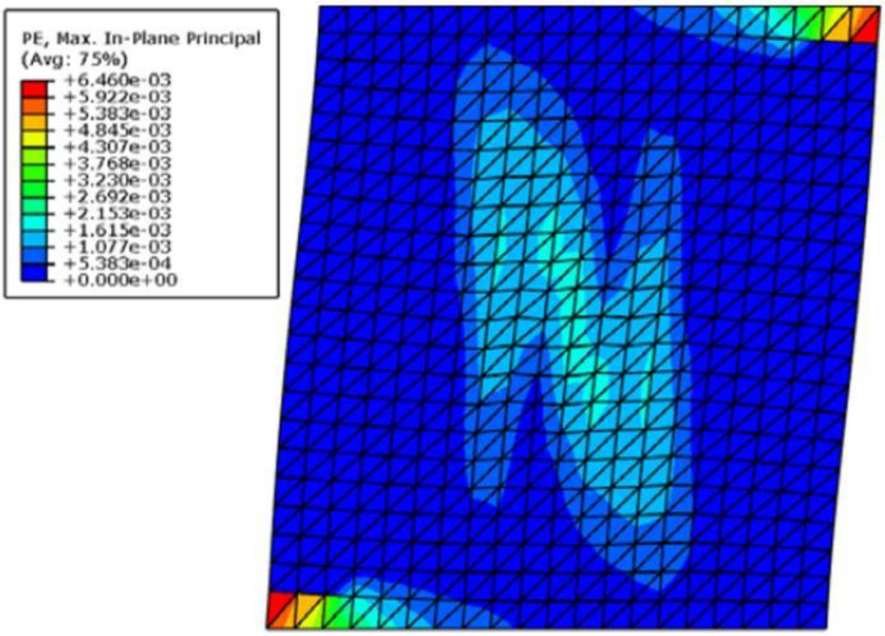

Figure 2.36: Maximum principal stresses in the macro-model indicating a coarse stress response (Annecchiarico et al., 2010)

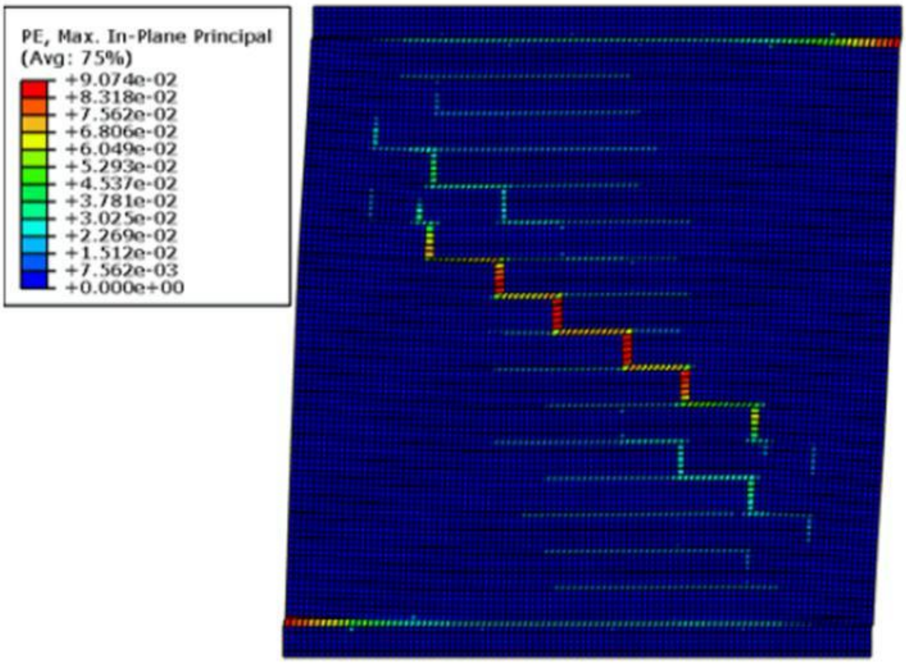

Figure 2.37: Maximum principal stresses in the micro-model indicating a fine stress response (Annecchiarico et al., 2010)

From the results shown in Figures 2.36 and 2.37, it is clear that the micro-model showcases a higher accuracy in predicting possible crack and failure patterns due to the higher sensitivity in the mesh. The results from the model have been compared with the experimental results shown in Figure 2.38.

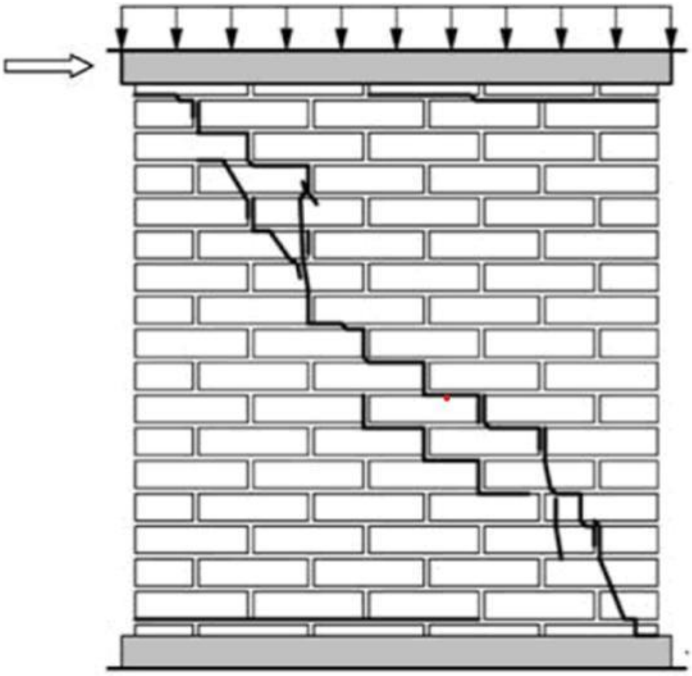

Figure 2.38: Experimental crack pattern of the masonry wall accurately corresponding with the micro-model (Lourenço et al., 1995)

Comparing the finite element models with the experimental results, the micro-model provides more accurate results that correlate with the experimental tests' crack patterns. The micro-modelling produces results of higher accuracy in the study.

Abdulla, Cunningham and Gillie (2017) produced a simplified micro-model to simulate the in-plane cracking of the individual masonry units through FEM. The differences between micro-modelling, simplified micro-modelling and macro-modelling are shown in Figure 2.39.

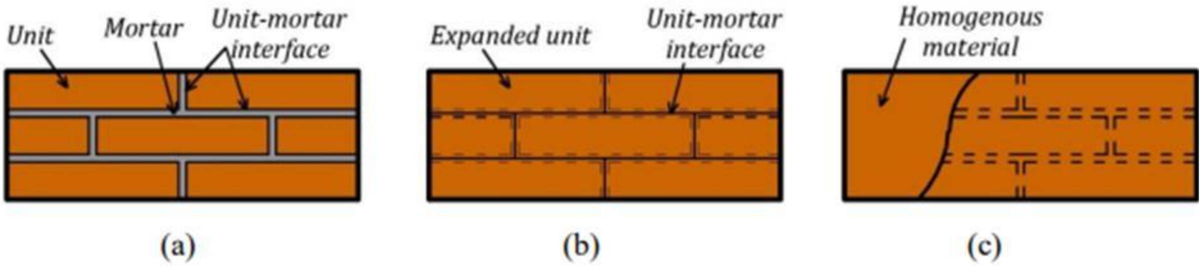

Figure 2.39: Differences between micro-modelling (a), simplified micro-modelling (b) and macro-modelling (c) (Abdulla et al., 2017)

Simplified micro-modelling ignores the mortar between masonry units and instead assumes a masonry-masonry interface. This differs from micro-modelling, where the mortar is modelled and influences the structure and macro-modelling, where the masonry wall is modelled as a homogeneous model.

FEA software divides the model and the individual parts into nodes. These nodes, placed at fixed, defined intervals in the x, y and z directions, form the connecting points of the mesh. The mesh is automatically generated according to the selected parameters and divides each part into smaller portions. These divided shapes are shown in Figure 2.40.

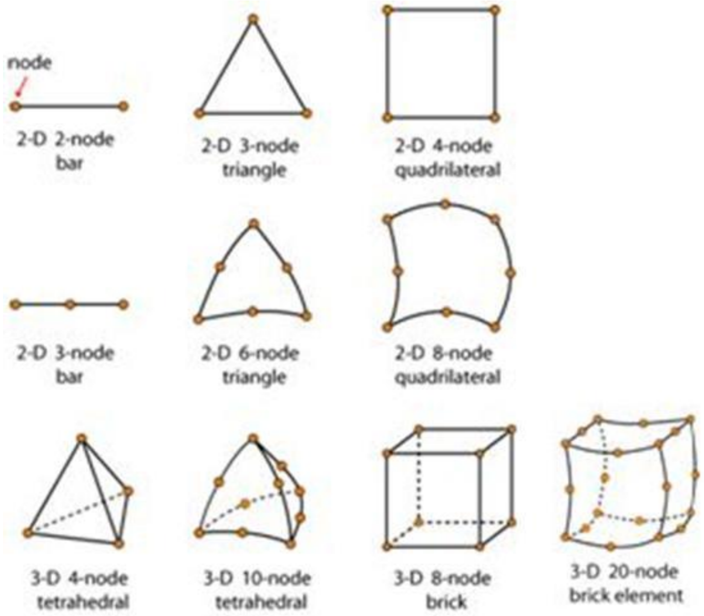

Figure 2.40: Types of elements that are used for finite element analysis (University of Cambridge DoITPoMS, 2016)

The masonry wall, modelled as a 3D model, consists of brick-type elements. Therefore, ABAQUS creates the mesh as a 3D 8-node brick element or a 3D 20-node brick element. These mesh elements are named C3D8 and C3D20, respectively. A C3D8 element is the first-order element and uses linear interpolation. A C3D20 element is a second-order element and uses quadratic interpolation.

A mesh created using C3D20 elements is assumed to provide more accurate results, as the second-order elements can allow internal buckling within the boundaries of the mesh. It, however, poses the negative response of higher processing requirements and therefore, longer simulation times. C3D20 elements can only be assigned using Abaqus/Standard solver. Where the Abaqus/Explicit solver is used, a C3D8 element is assigned.

In this research, the simplified micro-modelling has been conducted, and the mortar between the masonry units has been assumed to be an interface with a zero thickness. The model has been developed using Abaqus FEA, and the mesh elements have been generated as an 8-node 3D hexahedral element with reduced integration, namely a C3D8R element, as shown in Figure 2.41.

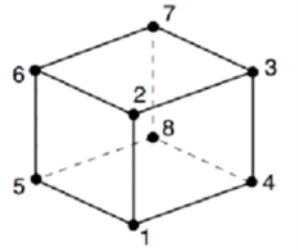

Figure 2.41: 8-node hexahedral element, namely C3D8 (Fanaie, N., Esfahani, F.G. and Soroushnia, S., 2015)

The researcher developed the model with a vertical and a horizontal load to simulate the shear behaviour of the masonry wall. The generated mesh of the simplified micro-model is shown in Figure 2.42.

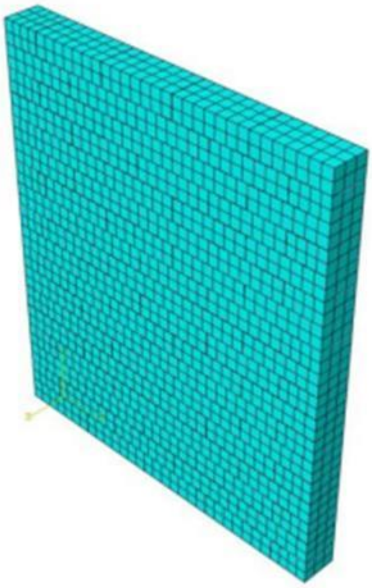

Figure 2.42: Generated mesh of the simplified micro-model (Abdulla et al., 2017)

The application of the vertical load and the horizontal load on the wall that is fully restrained at the bottom has produced results indicating accurate crack patterns similar to experimental studies. The researcher indicated the position of the crack patterns graphically, as shown in Figure 2.43.

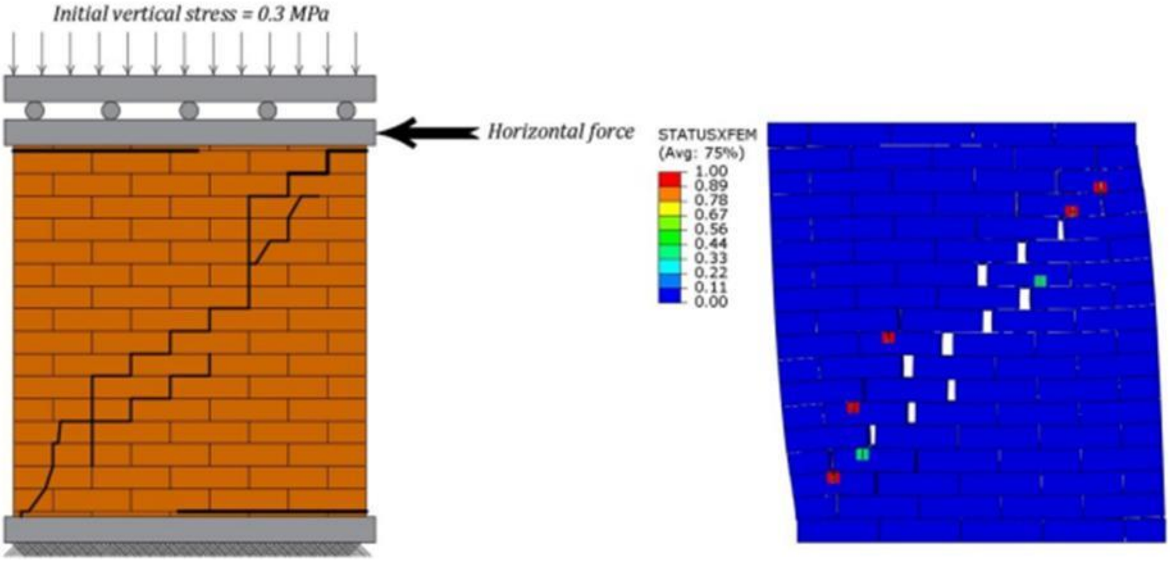

Figure 2.43: Experimental crack pattern (left) and simulated crack pattern (right) (Abdulla et al., 2017)

The results produced from the modelling indicated the crack patterns through a numerical legend, with 0.00 indicating no cracking and 1.00 where total cracking and separation between masonry units have occurred. The minimum principal stresses obtained from the numerical analysis are shown in Figure 2.44.

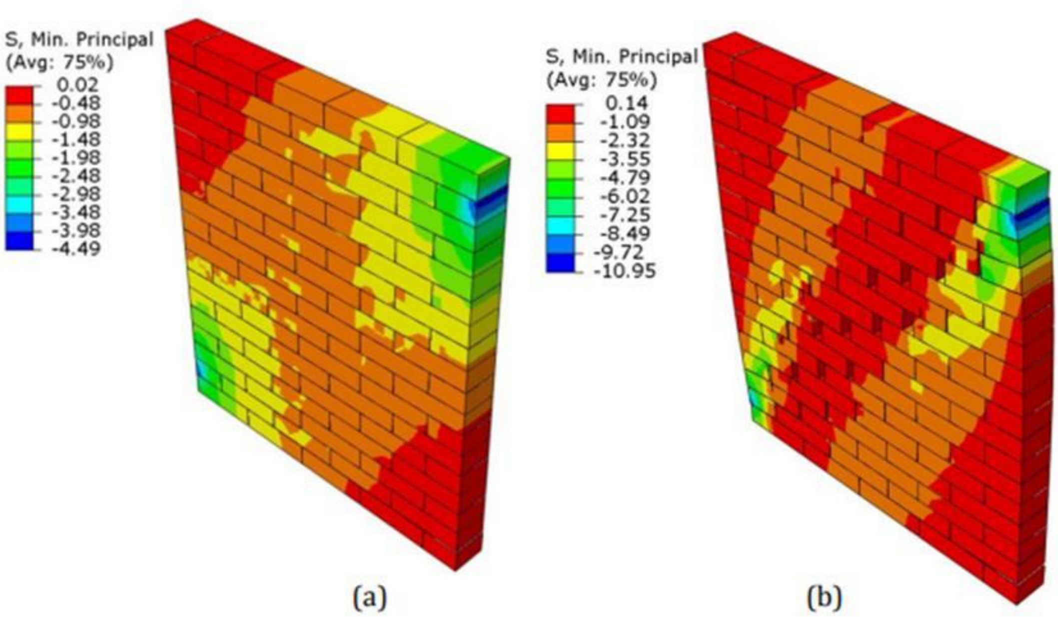

Figure 2.44: Minimum stress with 1 mm displacement (a) and 4 mm displacement (b) in the masonry wall (Abdulla et al., 2017)

With an increased displacement, the crack pattern that develops in the masonry wall is indicated more clearly. The crack patterns in the model accurately represent the results obtained from the experimental results, and the model has therefore been verified.

Comparing the various methods by which finite element modelling can be conducted to model a masonry wall accurately, it has been shown that macro-modelling does not accurately represent the actual failure patterns within the wall. For the current research, where the application is to model an old masonry wall where accuracy is essential, micro-modelling and simplified micro-modelling have been proven sufficient. However, due to the varying material properties located throughout the old masonry wall, a simplified approach still produces accurate results with the added benefit of lower computational resources required.

The benefits of conducting FEM to analyse heritage structures have been realised worldwide. However, with the dearth of literature on heritage structures in South Africa, a gap in research is exposed.

2.5 Heritage structures in South Africa

South Africa has a rich history built in a relatively short timeframe compared to different world cultures. Through this history, which has shaped South Africa's cultural, political and demographical landscape, the built environment has seen significant degradation due to the lack of research, skills and equipment required to ensure adequate conservation of these structures. This section introduces various world heritage and national heritage sites.

2.5.1 World heritage sites in South Africa

South Africa is home to various world heritage sites. These sites include the Mapungubwe cultural landscape, an important example of early cultural integration and development in South Africa, the Cradle of Humankind, home to the earliest and highest concentration of human ancestral remains; and Robben Island, where Nelson Mandela was imprisoned for 18 years before the fall of Apartheid. These examples of world heritage sites are shown in Figures 2.45 to 2.47.

Figure 2.45: Ancient rock drawings at Mapungubwe cultural landscape

Figure 2.46: Human ancestral remains found at one of the sites of the Cradle of Humankind

Figure 2.47: Entrance to Robben Island

2.5.2 National heritage sites in South Africa

National heritage sites, as declared by SAHRA, include the Castle of Good Hope, the oldest Dutch colonial building of the era in South Africa, the South African Astronomical Observatory, the oldest permanent observatory in the southern hemisphere, and Dal Josafat, a cultural landscape with buildings showcasing excellent examples of Cape Dutch architecture. Photos of these national heritage sites are shown in Figures 2.48 to 2.50.

Figure 2.48: Photo of the Castle of Good Hope

Figure 2.49: The South African Astronomical Observatory

Figure 2.50: Front view of the Non-Pareille manor house

The Non-Pareille manor house, situated on the Dal Josafat farmlands, exhibits Cape Dutch architecture. The manor house has been selected for the current study because urgent attention for restoration and conservation is required following severe structural fire damage.

2.6 Summary of findings

The literature has been reviewed, and data has been processed that is significant to the current research. Table 2.3 summarises the literature and the significance of the current research.

Table 2.3: Summary of literature findings

Author(s)	Research Title	Significance	Topic Relation
Abdulla et al. (2017)	Simulating masonry wall behaviour using a simplified micro-model approach	Micro- and simplified micro-modelling of masonry wall	Comparison between micro- and simplified micro-modelling
Akoglu et al. (2020)	Combined use of ultrasonic pulse velocity (UPV) testing and digital technologies: A model for long-term condition monitoring memorials in historic Grove Street Cemetery, New Haven	UPV testing to produce ultrasound tomography of old tombstones	UPV test methods and the graphical plotting of material properties
Alwash et al. (2015)	Non-destructive strength evaluation of concrete: Analysis of some key factors using synthetic simulations	Comparison between rebound number and UPV test results	Showcases RILEM chart to correlate rebound number and UPV test results
Annecchiarico et al. (2010)	Micro and macro-finite element modelling of brick masonry panels subject to lateral loadings	Macro- and micro-modelling of masonry wall	Comparison of results between macro- and micro-modelling
Breysse et al. (2008)	How to combine several non-destructive techniques for a better assessment of concrete structures	Combining NDT and analysis	Explains significance of NDT combined with FEM
Casarin et al. (2007)	Evaluation of the structural behaviour of historic masonry buildings by using a sonic pulse velocity method	Conducting of UPV testing in isolation	Indicates the need for other test methods to be conducted with UPV testing for more accurate results
D'Altri et al. (2018)	Stability analysis of leaning historic masonry structures	3D scanning and macro-model of old leaning tower	Describes the current condition of old structure through macro-modelling
Illampas et al. (2017)	Validation of the repair effectiveness of clay-based grout injections by lateral load testing of an adobe model building	Grout injection for adobe brick structural repairs	Explains visual inspection leading to crack repair method

Jiao et al. (2019)	Non-destructive inspection of a brick-timber structure in a modern architectural heritage building: Lecture Hall of the Anyuan Miners' Club, China	Non-destructive testing of old structure	Presents testing method for rebound hammer testing
Kujawa et al. (2020)	Finite element modelling of a historic church structure in the context of a masonry damage analysis	Finite element modelling of 14th century church	Showcases method for 3D scanning and finite element modelling
Kumar and Pallav (2020)	Experimental and Numerical Investigation of Old Masonry Wall Using a Macro-Modeling Approach	Visual inspection, rebound hammer testing and UPV testing of old structure	Showcases detailed test methods for overall material testing
Kulkarni and Admane (2015)	Recommendation for systematic and precise framework of structural audit of residential building	Visual inspection overview	Explains significance of detailed visual inspection
Loke et al. (2019)	The sustainable restoration of historic masonry: Robben Island	Visual inspection of damaged heritage structure	Explains the visual inspection indicating damage caused by improper repairs
Merzoug et al. (2020).	The impact of reinforced concrete on the modern-day architectural heritage of Algeria	UPV testing and finite element modelling	Explains method of UPV testing and finite element modelling in African perspective
Nnaji et al. (2016)	Investigative Study of Biodeterioration of External Sandcrete/Concrete Walls in Nigeria	Rebound hammer testing on sandcrete material	Shows test method for rebound hammer tests on unorthodox materials
Russo (2017)	Simplified procedure for structural integrity's evaluation of monuments in constrained context: The case of a Buddhist Temple in Bagan (Myanmar)	Rapid results from non-destructive testing	Presents test methods to produce rapid, significant results, including rebound hammer testing

Saloustros et al (2017)	An Enhanced Finite Element Macro-Model for the Realistic Simulation of Localized Cracks in Masonry Structures: A Large-Scale Application.	Macro-modelling of multi-storey structure	Compares various mesh patterns of a macro-model
Tampone and Ruggieri (2016)	State-of-the-art technology on conservation of ancient roofs with timber structure.	Visual inspection of substandard structural repairs	Emphasises the importance of higher quality restoration
Verma et al. (2013)	Review of Non-destructive Testing Methods for Condition Monitoring of Concrete Structures.	Description of NDT methods	Comparison between test methods

2.7 Conclusion

Non-destructive testing to determine the structural properties and finite element modelling to analyse the historical structures have received much research attention with applications worldwide. Many literature articles focus on conserving heritage structures, and effective remedial action is generally proposed. However, certain fields require further research due to the lack of data. The dearth of literature on the testing and analysis of heritage structures from a South African perspective indicates a significant gap that requires extensive research by future researchers.

Visual inspection is an important pre-testing step to assist the researcher in prescribing suitable test methods, whether non-destructive or destructive. From visual inspection, recommendations are made regarding further testing and the required testing parameters. Various non-destructive test methods are available, each with separate capabilities and applications. In the specific case of historical structures, preservation from an architectural and structural viewpoint is critical; therefore, non-destructive testing is preferred. Although non-destructive testing is done in the field, the application of historical structures has received little attention in South Africa.

FEM is a powerful tool in determining the structural stability of historic structures and has been used worldwide with great success. Although FEM studies have been undertaken in South Africa, literature on the applications of heritage structures is severely lacking. Further to the studies, structural analysis can be performed through finite element modelling, with the material properties determined through testing.

The literature reviewed indicated a serious absence of research on structural testing and analysis in Africa, with little to no data available in the field in South Africa. Developing sustainable conservation plans in South Africa through non-destructive testing and finite element modelling will ensure that historical structures can be maintained and repaired affordably while effectively increasing the lifespan of the country's cultural heritage. With the wide range of valuable expertise from various departments and engagement with the governing bodies, effective rehabilitation can be applied to heritage structures in South Africa and the heritage of other developing countries.

The Non-Pareille manor house has been selected for further research as it is an excellent example of Cape Dutch architecture and is in dire need of urgent intervention for restoration and conservation. This is further detailed in the following sections of the current research.

Chapter 3 RECONNAISSANCE SURVEY

A reconnaissance survey is an essential step before conducting further research. It provides a basis for experimental testing and analytical modelling. This section discusses the methodology followed to complete the reconnaissance survey and to obtain suitable information for the overall research. The findings of the reconnaissance survey have been introduced.

The reconnaissance survey, conducted to determine site-specific parameters essential for further testing, is also used to obtain site measurements for which the model is developed. The site topography and the overall structure are inspected, the significant wall to be tested is evaluated and the positions on the wall for testing are selected. This provides a preliminary overview of the data required before non-destructive testing can be done.

3.1 About Non-Pareille manor house

Non-Pareille manor house is located in Dal Josafat, Paarl, South Africa. Paarl is home to significant historical events, such as being the town where the "Genootskap van Regte Afrikaners" (Society of True Afrikaners) laid the foundations for the Afrikaans language in the 19th century and where Nelson Mandela ended his 27-year imprisonment and continued towards the post-apartheid era of South Africa.

The farmland was granted to Pierre Vivier in 1694 after his settlement on the land in 1690. The property eventually came under the ownership of Jan Gysbert Hugo in 1804. The front gable of the Non-Pareille manor house is dated 1826 and is assumed to be built by Jan Gysbert Hugo, while it is possible that the structure can predate the front gable. The gables are described as "holbol", a typical feature in Cape Dutch architecture (Fransen, 2004).

The Non-Pareille manor house is built with strong Cape Dutch architectural influence. The architectural style is identified with T-, H- or U-shaped layout, a porch spanning the entire front face of the house, symmetrical front windows next to the entrance, a front door that is divided between a top and bottom (stable-type door), thatched roof with a steep slope and most commonly with prominent front gables and less significant end gables. Typical Cape Dutch gable drawings are shown in Figure 3.1.

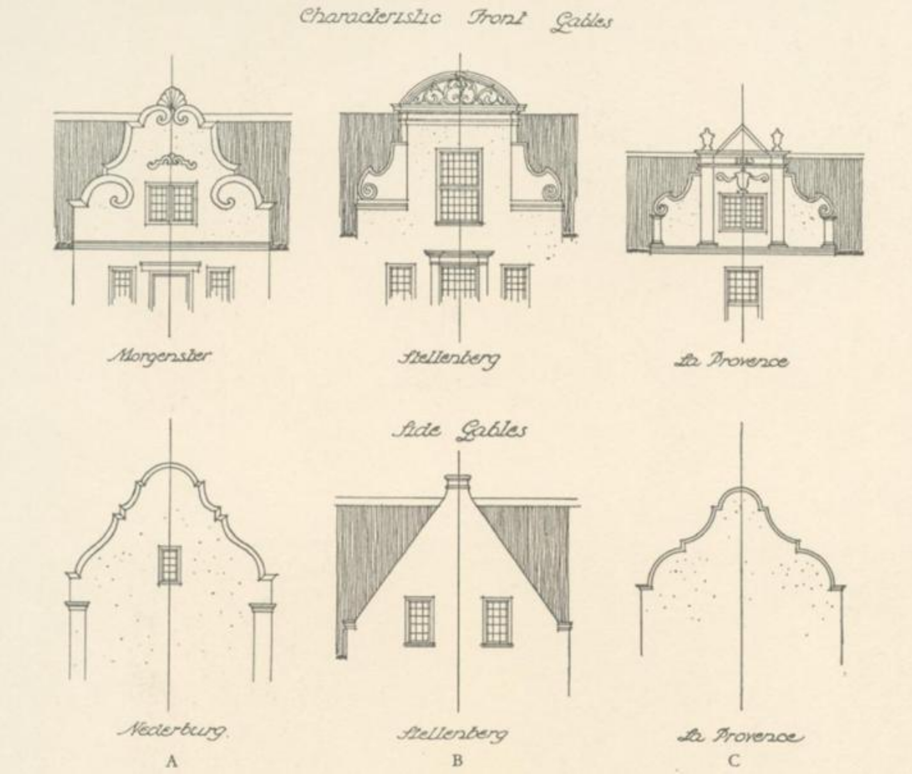

Figure 3.1: Artist impression of Cape Dutch front and side gables (Pearse, 1973)

The Non-Pareille manor house, currently managed by SAHRA, is classified as a Grade 1 heritage resource, the highest significance grading administered by SAHRA. The manor house has an H-shaped layout, with a thatched roof with steep slopes. The walls are constructed from unfired clay masonry, as the firing of clay masonry was an expensive practice at the time of construction (Pearse, 1973). To protect to the masonry units, the walls are plastered with mortar. On 29 July 2019, the manor house was ravaged by fire and has since been dilapidated. A news article detailing the damage is presented in Figure 3.2.

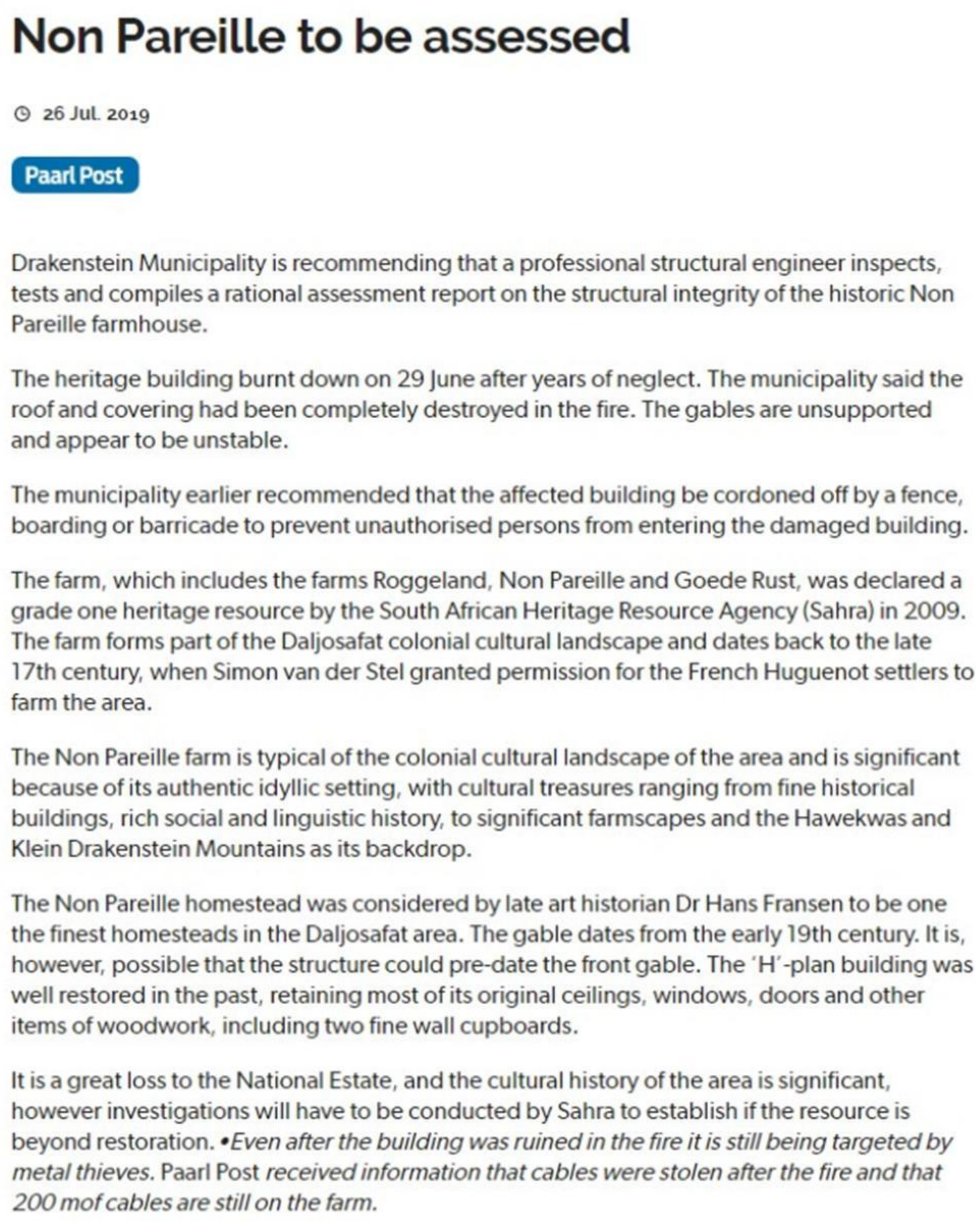

Non Pareille to be assessed

26 Jul. 2019

Paarl Post

Drakenstein Municipality is recommending that a professional structural engineer inspects, tests and compiles a rational assessment report on the structural integrity of the historic Non Pareille farmhouse.

The heritage building burnt down on 29 June after years of neglect. The municipality said the roof and covering had been completely destroyed in the fire. The gables are unsupported and appear to be unstable.

The municipality earlier recommended that the affected building be cordoned off by a fence, boarding or barricade to prevent unauthorised persons from entering the damaged building.

The farm, which includes the farms Roggeland, Non Pareille and Goede Rust, was declared a grade one heritage resource by the South African Heritage Resource Agency (Sahra) in 2009. The farm forms part of the Daljosafat colonial cultural landscape and dates back to the late 17th century, when Simon van der Stel granted permission for the French Huguenot settlers to farm the area.

The Non Pareille farm is typical of the colonial cultural landscape of the area and is significant because of its authentic idyllic setting, with cultural treasures ranging from fine historical buildings, rich social and linguistic history, to significant farmscapes and the Hawekwas and Klein Drakenstein Mountains as its backdrop.

The Non Pareille homestead was considered by late art historian Dr Hans Fransen to be one the finest homesteads in the Daljosafat area. The gable dates from the early 19th century. It is, however, possible that the structure could pre-date the front gable. The 'H'-plan building was well restored in the past, retaining most of its original ceilings, windows, doors and other items of woodwork, including two fine wall cupboards.

It is a great loss to the National Estate, and the cultural history of the area is significant, however investigations will have to be conducted by Sahra to establish if the resource is beyond restoration. •*Even after the building was ruined in the fire it is still being targeted by metal thieves.* Paarl Post *received information that cables were stolen after the fire and that 200 mof cables are still on the farm.*

Figure 3.2: Article from the local newspaper describing the fire at Non-Pareille manor house

This research will focus on the north-facing wall of the manor house to determine the structural serviceability following the damage caused by the fire. Photos of the house prior to the fire are shown in Figures 3.3 to 3.7.

Figure 3.3: North view of the manor house showing the immediate surroundings of the farmlands (Van der Walt, 2016)

Figure 3.4: Manor house H-shape layout (Van der Walt, 2016)

Figure 3.5: Manor house interior, viewing towards the front door (Van der Walt, 2016)

Figure 3.6: Example of historical artwork on the interior walls of the manor house (Van der Walt, 2016)

Figure 3.7: Non-Pareille manor house front gable (Van der Walt, 2016)

The north-facing wall consists of three panels – the eastern panel with a single window, the centre panel with two windows divided by the entrance door, and the western panel with a single window, similar to the eastern panel. The centre panel has a prominent gable above, with a single window and the date of 1826 above the window in the middle. The wall was selected for this research due to the historical significance of the front façade of the structure and providing a basis for further research towards the testing of the full structure. Site investigation has determined that further investigation is required to provide data for the determination of the mechanical properties of the heritage structure.

3.2 Visual inspection

A visual inspection was undertaken to identify the site-specific information as well as the significant masonry wall to be tested. The visual inspection identifies cracking, water ingress, settlement, material degradation and fire damage. Photographic evidence has been produced for all the visual imperfections, as well as the surroundings of the site.

The site is situated in Dal Josafat, Paarl, on the Non-Pareille farmlands. The site locality is shown in Figure 3.8. The subject structure is the manor house, exhibiting Cape Dutch architecture, and is built with an H-shape layout. The manor house is located at GPS coordinates 33°41’15”S, 19°0’13”E.

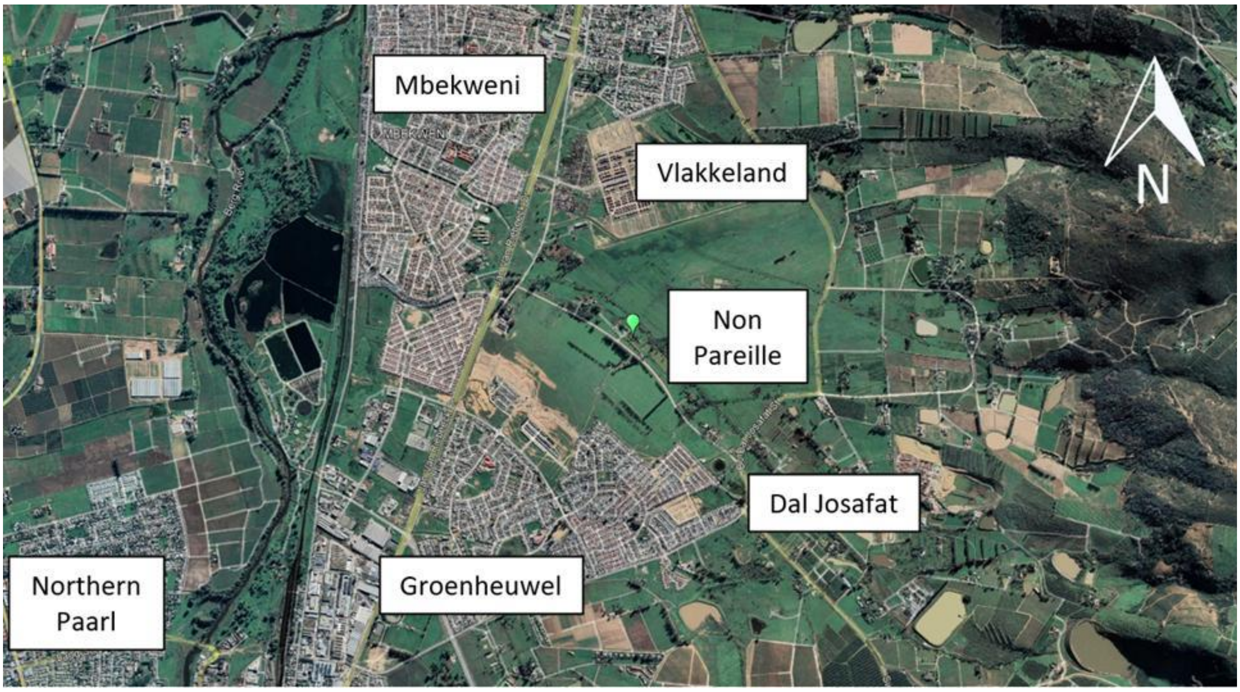

Figure 3.8: Location of Non-Pareille manor house on Dal Josafat farmlands, GPS coordinates 33°41’15”S, 19°0’13”E (Google Earth)

Access to the site is from Roggeland Road from Jan van Riebeek Drive situated to the west of the site. The site is bound to the north by the Vlakkeland housing development and to the south by the Groenheuwel residential neighbourhood, with Berg River further to the west.

The site’s topography features rolling terrain of undeveloped grasslands with a sparsely populated rural community. The site, managed by SAHRA, is protected by security patrols.

An enlarged aerial photograph of the Non-Pareille manor house is shown in Figure 3.9.

Figure 3.9: Enlarged aerial photograph of Non-Pareille manor house and immediate surroundings (Google Earth)

The aerial photograph indicates the H-shaped house with the fire-damaged roof structure. An on-site survey is conducted to study the house’s external walls and to select the significant wall for testing. After inspection of the overall structure, architectural features and visual damage, the front gable wall of the manor house was selected for further investigation. The gable wall in its current condition is shown in Figure 3.10.

Figure 3.10: Recent photo of the gable wall of the Non-Pareille manor house indicating overall damage

The manor house was ravaged by a fire on 29 July 2019, causing severe destruction to the structure. As a result of the fire, the entire thatch roof was destroyed, together with most timber elements such as beams, window frames and doorframes. The damage identification survey conducted on-site has provided a more detailed description.

As a result of the fire, the overall stability of structural elements is unknown and therefore seen as a potential hazard. A warning note has been placed at the front door to deter intruders, as shown in Figure 3.11.

Figure 3.11: Warning note on the front wall due to the hazardous potential of the building

The subject wall has been surveyed, and all the measurements have been collected using a measuring tape. The measurements have been noted, and CAD drawings were developed. The wall dimensions are shown in mm in Figure 3.12.

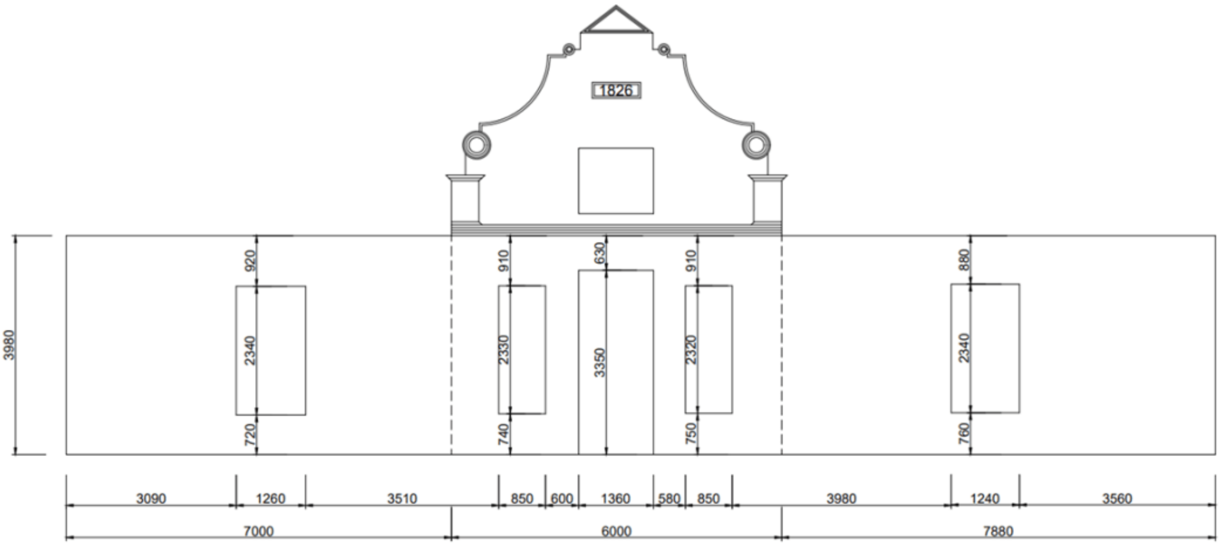

Figure 3.12: CAD drawing indicating the dimensions of the wall in mm

The overall width of the wall is measured as 600 mm. The width of the wall has been measured through the window opening (Figure 3.13). The burnt wood in the window opening is an indication of vandalism at the site, which remains an ongoing problem.

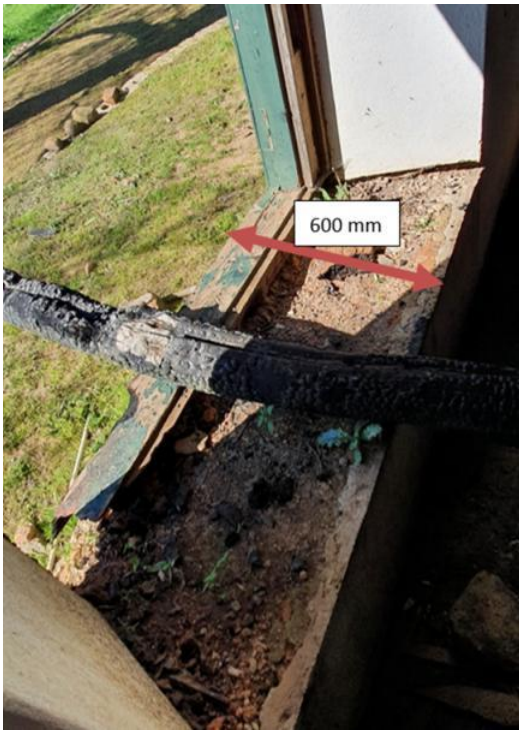

Figure 3.13: Wall width measured at the window opening

The wall is further inspected, and photographic evidence of all visual defects is collected. The structure is inspected for out-of-plane movement and cracking. The visual defects are discussed in detail in the damage identification survey.

3.3 Damage identification survey

The Non-Pareille manor house indicates clear examples of visual damage following the fire damage that has been sustained. The thatch roof has been destroyed, further masonry breakouts are evident, and the timber window and door frames have sustained significant damage. The damaged roof structure and further damage to the masonry wall are shown in Figure 3.14.

Figure 3.14: Visual damage on the eastern section of the gable wall

In Figure 3.14, the remainder of the roof structure is visible on the eastern section of the wall. The partially fire-damaged timber rafters regularly break when exposed to wind loads. Plasterwork has broken out below the window, which could be attributed to the additional fire heat that deteriorated the mortar. Several thin cracks are located on the wall; however, more severe cracking has been located where the east panel joins with the centre panel, as shown in Figure 3.15. The position of this crack is where an internal wall laterally braces the wall.

Figure 3.15: Cracking between east and centre wall panels

The breakout of the plasterwork on the east panel is shown in Figure 3.16.

Figure 3.16: Plasterwork breakout on east wall panel exposing the masonry bricks

More cracking has been located between the top of the front door and the window frame in the gable. This crack exhibits signs of separation, as shown in Figure 3.17.

Figure 3.17: Gable crack indicating separation

Moving toward the western panel of the masonry wall, more vertical and horizontal cracking is evident, as shown in Figure 3.18.

Figure 3.18: Visual damage on the western section of the gable wall

Vertical cracks are located at the west end of the wall, where the panel lines up with the corner of the structure, with a diagonal crack at the top right corner of the window frame. As shown in Figure 3.18, a similar vertical crack line is located where the west panel connects with the centre panel. This is also the position where an internal wall laterally braces the wall. More cracking is located throughout the wall, including horizontal cracking in line with the bottom of the window frame. The diagonal crack is shown in Figure 3.19.

Figure 3.19: Diagonal crack above window of the west wall panel

A horizontal displacement has been noted on the masonry wall's centre panel, as shown in Figure 3.20.

Figure 3.20: Horizontal displacement in the gable above the centre wall panel

The masonry bricks broken from the structure are clearly visible. The horizontal displacement at the centre panel is shown along the architectural ridge between the centre panel and the gable.

This could indicate movement in the gable due to the unbraced state or poor workmanship during construction.

The dimensions of the cracks have been measured using a combination of manual measurement with a measuring tape and UPV testing. These methods were used to determine the crack width and depth and form part of the non-destructive testing conducted on the wall.

The visual inspection has indicated all the positions where possible failure can occur and where cracking is located within the wall. It is, therefore, essential to conduct further testing of the structure to determine the mechanical properties of the wall.

3.4 Conclusion

Non-Pareille manor house has been shown to be an excellent example of Cape Dutch architecture with a significant history, leading to its protection as a heritage site by SAHRA. Unfortunately, the manor house has suffered severe fire damage which destroyed the roof structure and raised concerns about the overall stability of the front gable wall. The concerns prompted further investigation.

The front gable wall has been selected for investigation because of the architectural significance to the structure. An overall visual inspection was conducted to classify the wall sections and determine the dimensions. A further detailed investigation was conducted to identify visual damage on the wall.

The fire damage is evident, with the roof structure destroyed. Several cracks are located throughout the wall, with significant cracking on the gable indicating separation. Horizontal deflection has been noted in the gable, which is currently unbraced following the destruction of the roof structure. Following the identification of damage, further investigation is required to determine the mechanical properties of the wall.

Chapter 4 NON-DESTRUCTIVE TESTING

Heritage structures are increasingly exhibiting aesthetic and structural damage. This is particularly problematic in South Africa where little research is being done to reduce the degradation of the heritage structures. The Non-Pareille manor house is an endangered heritage structure in South Africa requiring investigation to determine the mechanical properties of the gable wall.

The mechanical properties of the masonry wall are determined through non-destructive testing. Rebound hammer and ultrasonic pulse velocity testing are done, and laboratory testing is done on masonry samples to establish the relationship to correlate material properties. This assessment, unique to South African heritage structures, assists with the development of a numerical model for further investigation.

4.1 Rebound hammer testing

The surface level compressive strength of the masonry wall has been determined through rebound hammer testing. Testing has been done at selected locations spaced evenly horizontally and vertically on each wall panel. The test has been done in a 4x4 grid with 10 mm spacing at each location. This produced 16 test results where the average rebound number has been calculated for each location. The average rebound numbers have been plotted graphically to indicate the spread of results and the strength distribution over the wall. The Ectha PRO digital test hammer, produced by DRC Italia, has been used for the rebound testing. The Ectha PRO is designed in accordance with various international standards, as indicated in the product manual provided by the manufacturer.

The plunger of the instrument is released to fully extend. The plunger is pressed towards the surface to be tested, which pushes the internal mass to the back of the instrument. When fully compressed, the internal mass is released to strike the front of the instrument. On impact, the mass bounces back and registers the rebound as an index number on the scale or display. The Ectha PRO has correlation equations to convert the rebound index to compressive strength. The built-in correlation is based on the instrument's angle and standard concrete's corresponding strengths. Because the tests have been done on masonry, new correlation factors have been developed through further lab testing on the material which have been discussed in further detail in following sections. The technical specifications of the Ectha PRO are found in the product manual provided by the manufacturer. The Ectha PRO rebound hammer is shown in Figure 4.1.

Figure 4.1: Ectha PRO rebound hammer (Ectha PRO digital test hammer, n.d.)

The Ectha Pro automatically generates a table of raw result from which the average rebound number is calculated. The average rebound number calculation has been shown for test position RH1, with the full raw results displayed in Appendix B. The rebound number readings for RH1 are shown in Table 4.1.

Table 4.1: Unrefined rebound number results for test position RH1

Project Name	Position	Measurement	Angle	Rebound number (R_n)
RV_DAL01	RH1	1	0	25
RV_DAL01	RH1	2	0	23
RV_DAL01	RH1	3	0	23
RV_DAL01	RH1	4	0	22
RV_DAL01	RH1	5	0	21
RV_DAL01	RH1	6	0	23
RV_DAL01	RH1	7	0	23
RV_DAL01	RH1	8	0	24
RV_DAL01	RH1	9	0	25
RV_DAL01	RH1	10	0	31
RV_DAL01	RH1	11	0	30
RV_DAL01	RH1	12	0	23
RV_DAL01	RH1	13	0	23
RV_DAL01	RH1	14	0	22
RV_DAL01	RH1	15	0	22
RV_DAL01	RH1	16	0	20

A testing angle of 0° is chosen to correspond with tests conducted in the horizontal plane. The average rebound number has been obtained from the rebound number (R_n) readings, as shown in Table 4.1. This equates to an average rebound number of 23.75 for test position RH1.

The wall has been divided into separate testing zones to account for varying material properties within the wall; this is expected due to the age of the wall and the degradation to which the wall has been exposed as a result of time and fire damage. The test positions within the zones are shown in Figure 4.2.

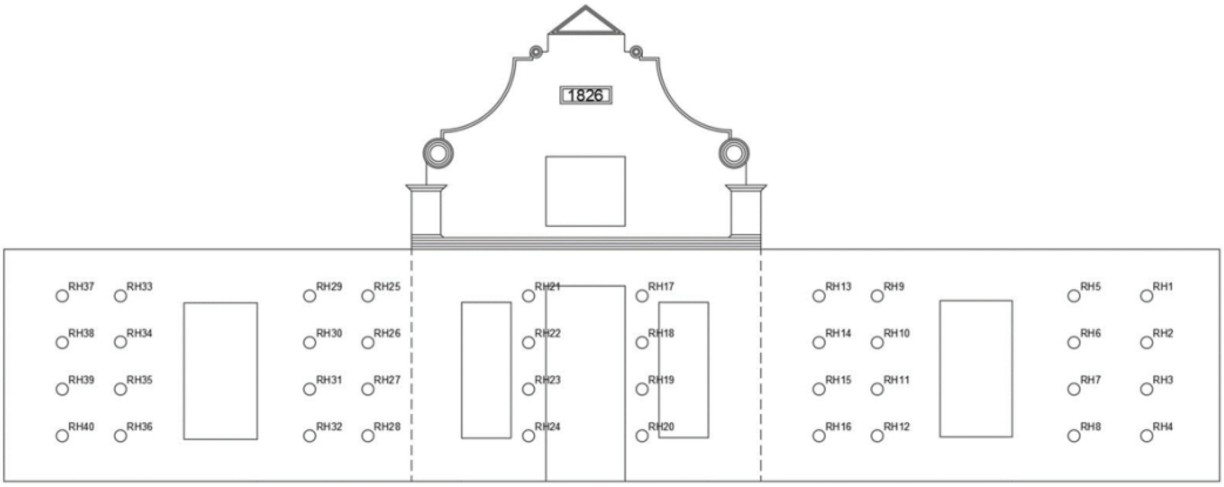

Figure 4.2: CAD drawing of rebound hammer test positions on the old masonry wall

The average rebound numbers have been summarised and are shown in Table 4.2 for all test positions.

Table 4.2: Rebound number results for all test positions

Position Description	Test Position	Average Rebound Number
Right panel, right side of window opening	RH1	23,75
	RH2	25,13
	RH3	22,31
	RH4	23,31
	RH5	23,69
	RH6	23,06
	RH7	29,38
	RH8	23,31
Right panel, left side of window opening	RH9	17,25
	RH10	20,94
	RH11	24,81
	RH12	19,94
	RH13	19,44
	RH14	21,25
	RH15	26,19
	RH16	19,19
Centre panel, right side of door opening	RH17	29,00
	RH18	29,88
	RH19	25,50
	RH20	31,63
Centre panel, left side of door opening	RH21	26,50
	RH22	26,63
	RH23	32,88
	RH24	27,56
Left panel, right side of window opening	RH25	24,00
	RH26	23,25
	RH27	22,56
	RH28	20,63
	RH29	22,50
	RH30	23,00
	RH31	22,38
	RH32	18,75
Right panel, right side of window opening	RH33	21,69
	RH34	20,81
	RH35	21,81
	RH36	19,50
	RH37	24,00
	RH38	22,88
	RH39	25,06
	RH40	28,25

The test equipment has built-in correlation equations to calculate the surface-level compressive strength from the rebound number. However, this correlation is based on modern concrete, and a new correlation equation is required for the application on the old masonry. This is done through laboratory testing and is further discussed in the following section.

4.2 Laboratory testing

Testing has been done in a laboratory to determine the relationship between compressive strength and rebound hammer of old masonry samples. Due to the protected nature of the heritage building, removing cores from the structure is not allowed. However, as Non-Pareille manor house has suffered fire damage, permission was granted to use masonry samples that have broken off the main structure to conduct lab testing.

The masonry samples were carefully selected according to the following criteria: (1) the location of the sample relative to the subject wall; (2) the shape of the sample; and (3) the visual properties of the sample. The selection criteria are discussed below.

The location of sample (1) is critical, as it needs to be near the subject wall to ensure that it did not form part of another section of the structure. It is also critical to select multiple samples in locations spread along the subject wall to ensure a suitable spread of results.

The shapes of samples (2) need to be suitably selected to ensure that each sample can be placed in a concrete cube press. A cubic shape is preferred, or the sample needs to be a suitable size to allow manual shaping into a cube.

The visual properties of samples (3) are critical, as maintenance has been done to the main structure over the years. Therefore, it is highly possible that some of the masonry samples can include modern masonry, which is not applicable to the study. This can be easily identified in the colour of the masonry: the old masonry bricks were unfired clay and were shaped without sophisticated moulds. This produced a lighter red colour and sides with non-planar properties. The old masonry also indicates less brittle and more plastic behaviour than modern masonry, should a fractured edge be inspected.

A total of seven masonry samples have been selected as per the criteria listed. The samples have been shaped into cubes, and each sample's dimensions and mass have been recorded. The dimensions and the mass have been used to determine the volume of each masonry sample. Rebound hammer testing has been conducted on each of the masonry samples. A photo of a masonry brick sample taken from the site is shown in Figure 4.3.

Figure 4.3: Masonry brick from old wall

The masonry sample exhibits a traditional forming method with rough edges and made from a possible unfired clay material. The remains of a fibrous material used as a binder during the manufacture of the masonry is visible in the figure. The masonry bricks exhibit a texture similar to a compressed clayey-silty material. Modern masonry bricks, showcasing a darker colour evident of fired clay bricks, have also been located on the site, indicating that repairs have been done on the house.

The masonry samples are shown in Figure 4.4. This includes the fractured samples that were damaged as a result of the testing.

Figure 4.4: Masonry brick sample (left) and broken sample (right)

The compressive strength of each sample is determined by using a concrete cube press in a laboratory. The concrete cube press provides an increasing force of 240 kN/min through a plate onto the sample. The force increases continuously until a fracture occurs in the masonry sample.

The force reading when the fracture occurs is recorded, and the compressive strength is calculated using Equation 4 below.

$$P = \frac{F}{A} \tag{4}$$

where:
P = Compressive Strength in MPa
F = Compression force at fracture in N
A = Sample top plane area in mm²

The cube press testing of the samples is shown in Figure 4.5. The masonry samples exhibited deformation prior to breaking. This is due to the unfired nature of the material, resulting in a less brittle sample with increased plasticity.

Figure 4.5: Crushed masonry brick sample

The compressive strength for each sample has been recorded. The rebound index number and the compressive strength of each sample have been correlated in a graph with the rebound number on x-axis and compressive strength on the y-axis. The best-fit line equation will provide a universal formula for determining the compressive strength of each rebound number for the specific material.

The mass of each sample has been recorded, and the density has been determined using the dimensions of each sample. This has been recorded to assist with the calculation of Poisson’s ratio and Young’s modulus from the results obtained through UPV testing. This is discussed in detail in a subsequent section.

A total of seven masonry samples have been selected for laboratory testing, with five samples producing relevant results because two samples were disregarded due to breaking and producing an outlier result. The samples have been shaped to form cubic bricks with dimensions of approximately 70x70x70 mm. The density of the samples has been determined through the dimensions and the mass of each. The samples have been subjected to rebound hammer testing and ultrasonic pulse velocity testing before conducting the crush testing. Each non-destructive test has been correlated to the destructive crush testing. This has provided a direct relationship between the rebound number and the compressive strength. The results from laboratory testing are shown in Table 4.3.

Table 4.3: Laboratory compressive test along with rebound hammer index value

	Seven brick samples from Non-Pareille manor house						
Test\Samples	OB-1	OB-2	OB-3	OB-4	OB-5	OB-6	OB-7
Rebound Hammer	NR	16	15	14	NR-Break	16	15
Measurements	75x75x60	70x65x55	75x70x55	75x65x60	NR-Break	70x65x55	75x70x55
Mass	573 g	355 g	439 g	409 g	NR-Break	380 g	410 g
Compressive Strength	6.82	1.76	1.22	0.615	NR-Break	1.73	1.19
Density	1697.78	1418.58	1520.35	1398.29	NR-Break	1518.482	1520.35
Description	Modern fired clay, brittle nature	Old unfired clay, plastic nature	Old unfired clay, plastic nature	Old unfired clay, plastic nature	Old, unfired clay, broke on first test	Old unfired clay, plastic nature	Old unfired clay, plastic nature

Sample OB-1 has been removed from the test group as it produced a result outside the average range of the remaining results in the group. Sample OB-5 fractured while testing, thus producing invalid results. The remaining five samples produced results ranging between 0.625 MPa and 1.76 MPa. The masonry samples' average density has been calculated as 1476.21 kg/m^3.

Figure 4.6 shows the correlation between the rebound number and the compressive strength of the masonry samples.

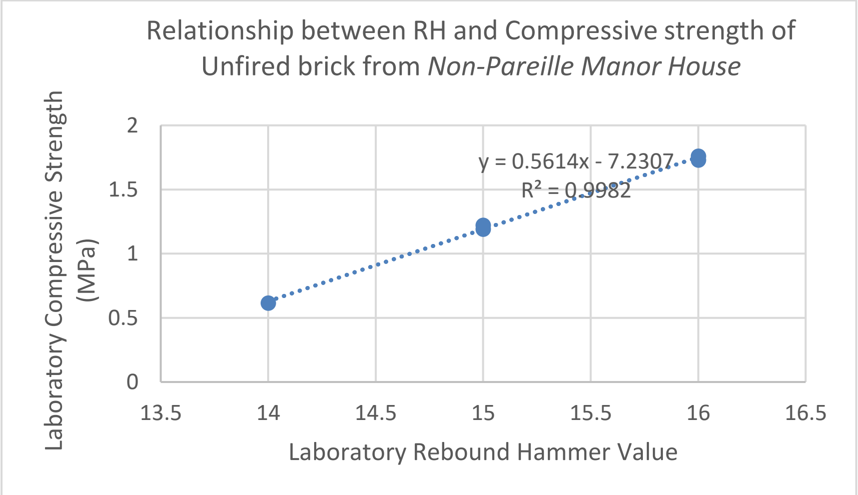

Figure 4.6: Linear relationship between the rebound number and compressive strength of the masonry samples

A best-fit line with the equation y = 0.5614x – 7.2307 has been interpreted from the graph. This equation has been applied to the results obtained on the old masonry wall to display the surface compressive strength at each test position. The compressive strength at each test position is shown in Table 4.4.

Table 4.4: Compressive strength determination at each test position through rebound hammer testing

Position Description	Test Position	Compressive Strength (MPa)
Right panel, right side of window opening	RH1	6,10
	RH2	6,88
	RH3	5,29
	RH4	5,86
	RH5	6,07
	RH6	5,72
	RH7	9,26
	RH8	5,86
Right panel, left side of window opening	RH9	2,45
	RH10	4,53
	RH11	6,70
	RH12	3,96
	RH13	3,68
	RH14	4,70
	RH15	7,47
	RH16	3,54
Centre panel, right side of door opening	RH17	9,05
	RH18	9,54
	RH19	7,09
	RH20	10,53
Centre panel, left side of door opening	RH21	7,65
	RH22	7,72
	RH23	11,23
	RH24	8,24
Left panel, right side of window opening	RH25	6,24
	RH26	5,82
	RH27	5,43
	RH28	4,35
	RH29	5,40
	RH30	5,68
	RH31	5,33
	RH32	3,30
Right panel, right side of window opening	RH33	4,95
	RH34	4,45
	RH35	5,01
	RH36	3,72
	RH37	6,24
	RH38	5,61
	RH39	6,84
	RH40	8,63

The distribution of the surface-level compressive strength has been calculated from the rebound number. The density was determined to be used in the calculation for Poisson's ratio and Young's modulus, discussed in detail in the following section. The established is applicable to the entire structure and is suitable for future rebound hammer testing.

4.3 Ultrasonic pulse velocity testing

Ultrasonic pulse velocity test equipment consists of a processor unit, transmitter, receiver and coupling cables. The test equipment used for ultrasonic pulse velocity testing is the Proceq Pundit Lab, developed by Proceq SA. The Proceq Pundit Lab allows remote testing away from an electricity source. The technical specifications are shown in the operating instruction leaflet, part number 820 326 01 E. The Proceq Pundit Lab is shown in Figure 4.7.

Figure 4.7: Proceq Pundit Lab testing equipment

The Pundit Lab is set up, ensuring all connector cables are secured. An initial reading is taken on the calibrating rod, included with the instrument. The transmitter and receiver are placed on either end of the calibrating rod, with the coupling gel, to ensure no air is entrapped between the instrument and the item being tested. The Pundit Lab is expected to return a test time reading of 25.4 µs from the calibration rod. Where any different value is obtained, it is adjusted manually on the instrument. The thickness of the wall is measured, and the data is recorded on the instrument. The processor unit is set up for automatic voltage output and automatic Rx gain due to the unknown nature of the material tested. Testing is done as a direct and indirect test.

For direct testing, the transmitter of the test equipment has been placed in the position to be tested, and the receiver has been placed on the opposite side of the wall, with both transmitter and receiver incorporating the coupling paste for more accurate contact. The test was repeated with slight variations in position until consistent readings could be produced. Before continuing to the next test position, this reading has been saved on the instrument.

For indirect testing, the transmitter and receiver have been placed at the same test positions on the same side of the wall. The transmitter and receiver have been placed at a constant distance of 200 mm using the coupling gel for both. The tests were repeated until consistent readings could be obtained after the result was stored on the instrument. The test positions are shown in Figure 4.8.

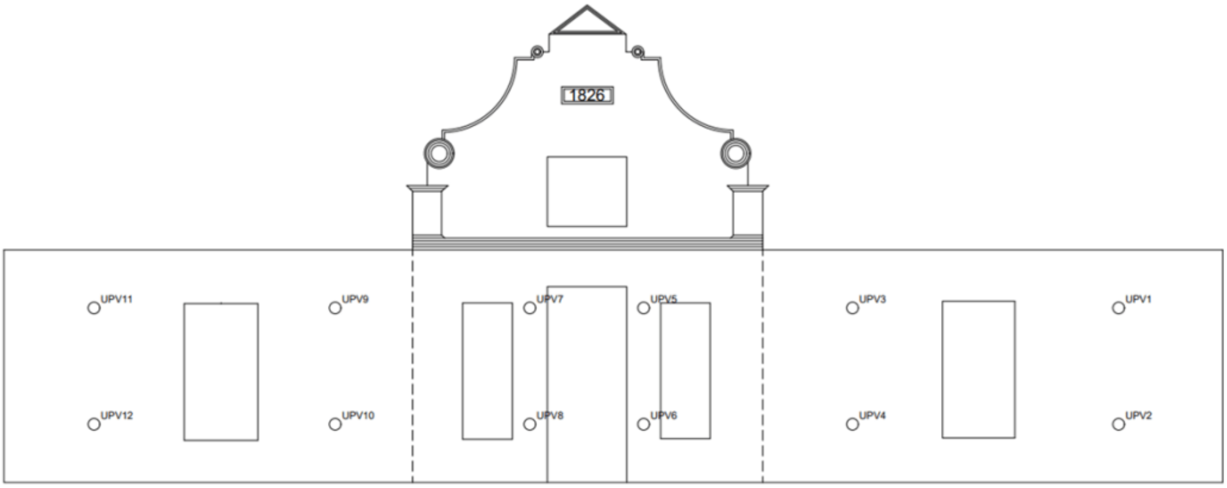

Figure 4.8: UPV testing positions on the old masonry wall

Twelve readings have been taken for the direct and transverse test each, providing a total of 24 results. The test positions have been selected to correspond with the testing zones. Four test results have been produced for each wall panel, providing the specific material properties allocated to the respective zone. The recorded results are direct and shear, shown in Table 4.5.

Table 4.5: Direct and shear velocity measurements through UPV testing

Direct Measurement		
Test Position	Velocity (m/s)	Time (µs)
UPV1	132	4534.4
UPV2	183	3281.7
UPV3	172	3479.1
UPV4	144	4164.9
UPV5	289	2073.5
UPV6	446	1344.3
UPV7	446	1344.3
UPV8	265	2268.1
UPV9	369	1627.9
UPV10	142	4224.6
UPV11	222	2705.8
UPV12	143	4194.5

Shear Measurement		
Test Position	Velocity (m/s)	Time (µs)
UPV1	1112	179.9
UPV2	1276	156.7
UPV3	1387	144.2
UPV4	799	250.2
UPV5	1789	111.8
UPV6	913	219.1
UPV7	2714	73.7
UPV8	1512	132.3
UPV9	1552	128.9
UPV10	357	559.6
UPV11	1574	127.1
UPV12	1711	116.9

The velocity measured through direct testing has returned relatively lower values when compared to the shear measurement. This is due to the testing done through the entire width of the wall, where the interior composition is unknown. The UPV results, therefore, accurately describe the overall properties of the wall and not the individual masonry bricks.

The velocities obtained from each result has been used in Equation 5 to calculate Poisson's ratio, as shown below.

$$\nu = \frac{V_{direct}{}^{2} - V_{shear}{}^{2}}{V_{direct}{}^{2} - 2 \times V_{shear}{}^{2}} \qquad (5)$$

where:
ν = Poisson's ratio
V_{direct} = direct pulse velocity in m/s
V_{shear} = shear pulse velocity in m/s

The calculated value for Poisson's ratio for each test position has been incorporated into Equation 6 to determine Young's modulus, as shown below.

$$E = \frac{\rho(1+\nu)(1-2\nu)}{1-\mu} V_{direct}{}^{2} \qquad (6)$$

where:
E = Young's modulus of elasticity in MPa
ν = Poisson's ratio
V_{direct} = pulse velocity in m/s
ρ = density in kg/m³

The values for Poisson’s ratio and Young’s modulus have been calculated, and the outputs are allocated to each test position which corresponds with the testing zones on the wall. Poisson’s ratio and Young’s modulus for each test zone are shown in Table 4.6.

Table 4.6: Poisson’s ratio and Young’s modulus for the old masonry wall

Position on wall	Test position	Poisson’s ratio	Young’s modulus (MPa)
Upper section of right wall panel	UPV1	0,248	4,399
	UPV2	0,247	5,788
Lower section of right wall panel	UPV3	0,248	6,844
	UPV4	0,246	6,804
Upper section of centre wall panel	UPV5	0,247	11,377
	UPV6	0,216	8,667
Lower section of centre wall panel	UPV7	0,247	8,728
	UPV8	0,246	12,18
Upper section of left wall panel	UPV9	0,243	8,535
	UPV10	0,229	6,705
Lower section of left wall panel	UPV11	0,247	8,807
	UPV12	0,249	10,423

The Non-Pareille manor house has suffered severe fire damage, resulting in visual cracks on the structure walls. Additional testing has been undertaken on the wall with the crack depth estimation method built into the Pundit Lab test equipment. All visual cracks have been located on the wall and plotted graphically in a site test journal, indicating the position of each crack. Crack depth testing through UPV is closely based on indirect testing. The transmitter and the receiver have been placed on either side of the crack with the coupling gel. The test has been conducted twice, with 150 mm and 300 mm between the transmitter and receiver. The two measurements combined approximate the crack depth at the testing position. The crack depth measurement positions are shown in Figure 4.9.

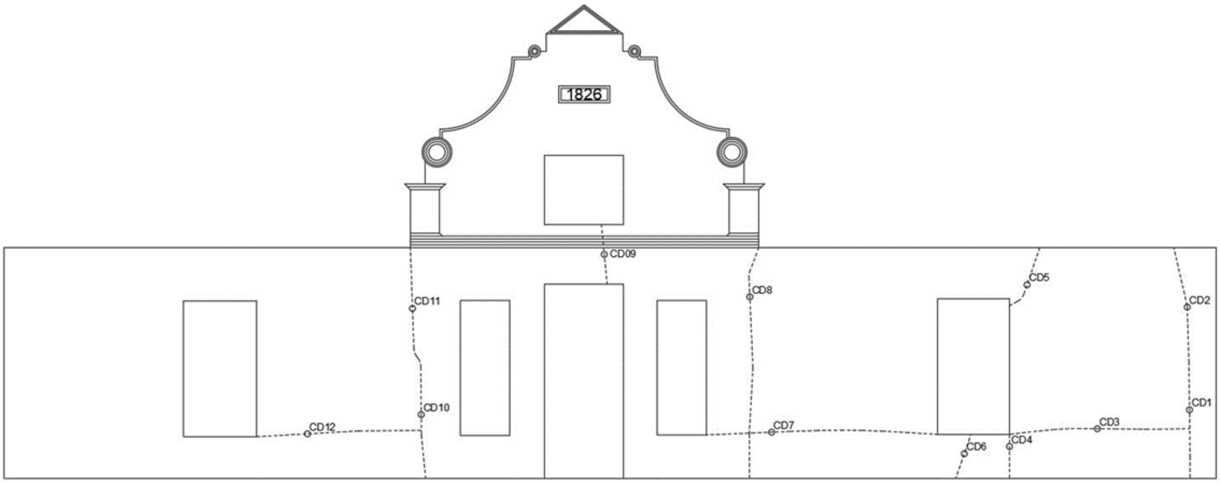

Figure 4.9: Crack depth testing positions

A total of 12 crack depth measurements have been taken, with a minimum of one test per crack. The crack depth measurements describe the condition of the wall at the specific position, identifying any internal movement that has occurred. The measured crack width and depth are shown in Table 4.7.

Table 4.7: Measurement of cracks on the old masonry wall through UPV testing and manual measurement

Crack Depth		
Test Position	**Crack Depth through UPV (mm)**	**Measured Crack Width mm)**
CD1	35	1
CD2	64	1
CD3	135	2
CD4	214	2
CD5	88	2
CD6	37	1
CD7	189	2
CD8	13	1
CD9	622	3
CD10	163	2
CD11	96	2
CD12	12	1

Many cracks have been visually identified as minor cracks and have been excluded from measurement. From the measured cracks, 41% of the cracks are identified as minor and only on surface level, with no influence on the structure. However, the remaining cracks indicate depths protruding through an entire brick course up to the whole width of the wall. The crack measurements are discussed in further detail in Chapter 6.

4.4 Conclusion

Non-destructive testing provides an effective method for evaluating the material properties of structural elements where damage to the structure must be limited. To determine the mechanical properties of Non-Pareille manor house, rebound hammer and ultrasonic pulse velocity testing have been done.

Rebound hammer testing has determined the surface-level compressive strength. The output from the test equipment was obtained as a rebound index number. The relationship between the rebound index number and compressive strength was determined through laboratory testing. This relationship determined the surface-level compressive strength for each rebound hammer test position on the masonry wall.

Ultrasonic pulse velocity testing has determined Poisson’s ratio and Young’s modulus throughout the masonry wall. The test equipment measures the pulse velocity over the travel path on the wall. Using a density measurement determined in the laboratory, Poisson’s ratio and Young’s modulus were calculated through empirical equations. Crack depth measurements were done on the wall using the UPV test equipment, and crack width was measured manually.

The non-destructive testing procedure described in this chapter is unique to South African heritage structures, specifically Cape Dutch architecture. The results obtained through the testing procedure assist with developing a numerical model for further analysis of the structure.

Chapter 5 FEM MODEL OF MASONRY WALL

Developing a finite element model allows the researcher to conduct various forms of analysis on a structure with realistic results. This section describes the development of the finite element model in detail, the actual and theoretical loads applied to the masonry wall and the interpretation of the results following analysis.

Finite element modelling is done as computational analysis to mathematically describe the properties of the masonry wall. The modelling and analysis of the masonry wall as a finite element follow the non-destructive testing phase of the current research. The results acquired from the non-destructive testing have been interpreted and incorporated into the model, from which the results have been graphically produced.

Finite element modelling is the development of a 3D model by using sophisticated computer software. This model accurately describes the material properties and element behaviour in prescribed circumstances through computer processing, which would otherwise be deemed too complex and time-consuming for manual calculations.

Finite element analysis is preferred for structural elements with complex geometry, loadings or material properties. By relying on enhanced processing, it is a powerful tool to solve numerical problems relating to the strength of materials. For this research, finite element analysis is performed to describe the mechanics of solid elements.

Prior to the development of the model, the model's accuracy needs to be is decided. The model can be developed as a macro-, micro-, or simplified micro-model. For this research, a simplified micro-model has been developed to define the masonry wall. The interface between the masonry units is assumed to be similar to the interface between masonry units of a modern wall. This creates a stable model with resistance in sliding between the masonry units.

5.1 Material properties

Finite element analysis for the old masonry wall is preferred due to the variations of the material properties throughout the wall. The material properties used in the development of the model have been determined through non-destructive testing. The material properties have been grouped in zones, as shown in Figure 5.1.

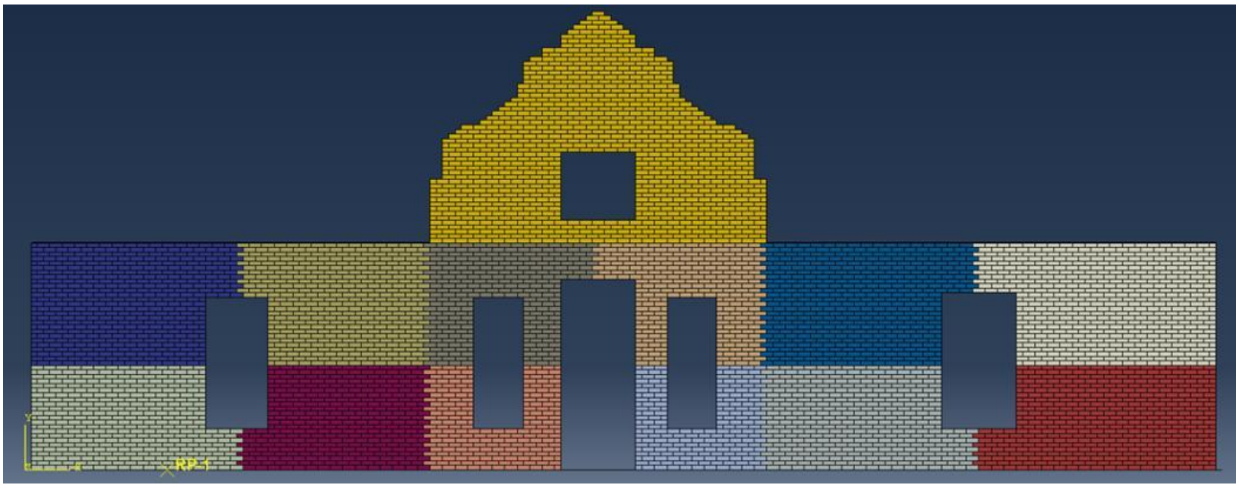

Figure 5.1: Colours indicating different material properties throughout the wall

As shown in Figure 5.1, the material properties are different throughout the wall. Each colour represents a testing zone, where non-destructive tests have been grouped. The four testing zones on the left and right wall panel each consist of four rebound hammer tests and one UPV test. The four testing zones in the centre panel each consist of two rebound hammer tests and one UPV test.

Each testing zone has been attributed material properties interpreted from the test results. The material properties have been incorporated into the model by creating various masonry units as parts, each having the allocated material properties. Young’s modulus and Poisson’s ratio have been interpreted from the test results to be incorporated into the development of the model.

5.2 Model development

The model is developed based on the actual measurements taken on-site. The size of the masonry unit used in the wall has been measured, including the average thickness of the mortar.

Using Abaqus FEA, the parts have been modelled and assembled to form a wall panel. The assembly allowed the voids in the wall to account for discontinuities in the form of window and door openings. The assembly for the wall is developed from ground to eaves to incorporate the load-bearing portion of the wall. The ultrasonic pulse velocity testing has been done for the full width of the wall, producing a homogeneous result in the face-to-face direction. Hence, the wall is modelled as masonry units for the full width, ignoring a wall cavity. The masonry brick model is shown in Figure 5.2.

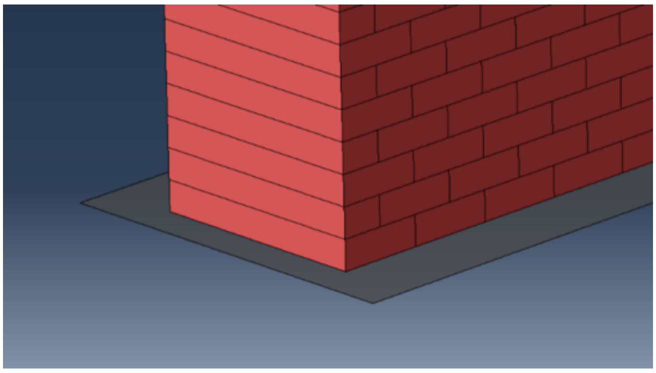

Figure 5.2: ABAQUS model of the masonry bricks

The gable has been modelled to half the total wall width, differing from the lower portion. Due to the architecture of the gable, it is comprised of more complex shapes. As consequence, the feature edges of the gable wall have been ignored as they serve no structural purpose. The internal portion has been modelled as a simplified micro-model. This will have a negligible effect on the results, as the architectural curves on the boundaries of the gable wall do not influence the overall structure.

Due to fire damage the house has sustained, the gable wall is completely unbraced and possibly unstable. The wall is unbraced between floor level and eaves height. Two internal and two end walls provide bracing against pushover actions on the masonry wall. Support actions are imposed on the wall at the floor level and each wall joint along the length of the subject wall. The support at the floor level is fully fixed against rotation and translation within the x-axis, y-axis and z-axis and fixed against translation at the eaves level due to the mostly intact ceiling. Along the length of the internal and end walls, pin supports will be imposed to provide a fixity against translation but freedom to rotate. Moment and reaction forces have been developed at the base of the wall, with only reaction force at each connecting wall. The end conditions are shown in Figure 5.3.

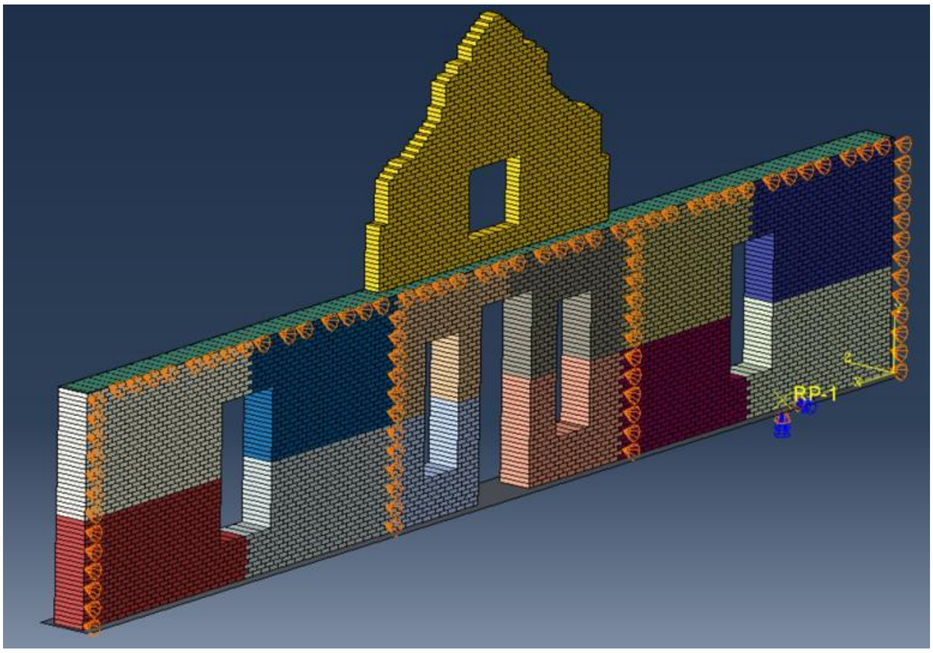

Figure 5.3: Boundary conditions of the masonry wall, indicating internal bracing of the wall

The parts have been developed for the model to the measurements taken on site for the masonry bricks. The part dimensions have been selected to include the masonry brick's full size and the mortar's thickness. The masonry units and mortar thickness are assumed to be constant throughout the wall.

Material properties are assigned to the parts following the test results in the relevant testing zone. Each test zone will have parts with unique parameters for Young’s modulus and Poisson’s ratio. The interaction between the mortar units has been assumed to have cohesive properties with friction. The interaction is required to resist sliding between the mortar units. This interaction has been assumed constant throughout the structure.

The mesh for the model has been created following the creation of the nodes. The node spacing is selected based on the time and memory constraints while considering analysis accuracy. The full development process of the model is described in Appendix C.

The model is developed as either 8-node brick elements or 20-node brick elements. As shown in Appendix C, an accurate model has been developed using a quasi-static approach and the Abaqus/Explicit solver. The 8-node brick elements are available using this solver, and the mesh was created as C3D8 elements.

For 8-node hexahedral elements with three degrees of freedom at each node, the shape functions have been shown in Equation 7.

$$N_i = \frac{1}{8}(1+\xi\xi_i)(1+\eta\eta_i)(1+\zeta\zeta_i) \tag{7}$$

where (ξ_i, η_i, ζ_i) indicates the coordinates of each node *i*.

The displacement is subsequently estimated through Equation 8.

$$u = \sum_{i=1}^{8} N_i u_i \quad , \quad v = \sum_{i=1}^{8} N_i v_i \quad , \quad w = \sum_{i=1}^{8} N_i w_i \tag{8}$$

where:
(N_1, N_2, $N_3 \ldots N_8$) reference the shape functions at the corresponding node; and
(u_1, u_2, $u_3 \ldots u_8$; v_1, v_2, $v_3 \ldots v_8$; w_1, w_2, $w_3 \ldots w_8$) reference the displacement at the corresponding node.

The strain-displacement relationship is developed through Equation 9.

$$\{\varepsilon\}_{6\times1} = [B]_{6\times24}\{\bar{x}\}_{24\times1} \tag{9}$$

where:
$\{\varepsilon\}_{6\times1}$ is the strain vector, as shown in Equation 10.

$$\{\varepsilon\}_{6\times1} = [\varepsilon_{xx} \quad \varepsilon_{yy} \quad \varepsilon_{zz} \quad \varepsilon_{xy} \quad \varepsilon_{yz} \quad \varepsilon_{zx}]^t \tag{10}$$

$\{\bar{x}\}_{24\times1}$ is the displacement at each corresponding node, as shown in Equation 11.

$$\{\bar{x}\}_{24\times1} = \sum_{r=1}^{8}[u_r \quad v_r \quad w_r]^t \tag{11}$$

$[B]_{6\times24}$ is as shown in Equation 12.

$$[B]_{6\times24}\sum_{r=1}^{8}\begin{bmatrix} \frac{\delta N_r}{\delta x} & 0 & 0 \\ 0 & \frac{\delta N_r}{\delta y} & 0 \\ 0 & 0 & \frac{\delta N_r}{\delta z} \\ \frac{\delta N_r}{\delta y} & \frac{\delta N_r}{\delta x} & 0 \\ 0 & \frac{\delta N_r}{\delta z} & \frac{\delta N_r}{\delta y} \\ \frac{\delta N_r}{\delta z} & 0 & \frac{\delta N_r}{\delta x} \end{bmatrix} \tag{12}$$

By incorporating a tress-strain relationship, the stresses can be subsequently determined through Equation 13.

$$\{\delta\}_{6\times1} = [D]_{6\times6}\{\varepsilon\}_{6\times1} \tag{13}$$

where:
$\{\varepsilon\}_{6\times1}$ is as defined previously.
$[D]_{6\times6}$ is the stiffness matrix, as shown in Equation 14.

$$[D]_{6\times6} = \frac{E}{(1+v)(1-2v)}\begin{bmatrix} (1-v) & v & v & 0 & 0 & 0 \\ v & (1-v) & v & 0 & 0 & 0 \\ v & v & (1-v) & 0 & 0 & 0 \\ 0 & 0 & 0 & (0.5-v) & 0 & 0 \\ 0 & 0 & 0 & 0 & (0.5-v) & 0 \\ 0 & 0 & 0 & 0 & 0 & (0.5-v) \end{bmatrix} \tag{14}$$

$\{\delta\}_{6\times1}$is the stress vector, as shown in Equation 15.

$$\{\delta\}_{6\times1} = [\delta_{xx} \quad \delta_{yy} \quad \delta_{zz} \quad \delta_{xy} \quad \delta_{yz} \quad \delta_{zx}] \tag{15}$$

The displacement and stress can be further obtained for the entire numerical model.

The goal of the model is to provide an accurate representation of the behaviour of the wall when various loads are imposed. These will be done through several steps, each having a different load case. The loads imposed on the wall are as per SANS 10160-2, commonly known as the loading code. The loads will be according to the serviceability limit state.

For the initial loading, only the self-weight of the wall has been imposed. This has given a representation of the wall with no other loadings imposed and tested the model's initial validity. Wind loadings have been included, acting on the outer face of the wall. The wind loads are determined from the weather data attributed to the area. The gravity load and the wind load have given a representation of the behaviour of the wall when a gravity-pushover analysis is performed.

The failure areas of the wall have been noted and compared to the visible crack patterns on the wall's surface. The material properties are adjusted for inconsistencies between the model and the actual data until the crack patterns correspond with the visible crack patterns on the wall. This deems the model accurate and suitable for further analysis.

With the house currently in a poor, destructed state, the goal is to be able to reconstruct the entire house in the future while keeping the original structure in its original state. The developed model has proven to correspond with the actual visual data obtained on-site. It is incorporated in the analysis where the gable is assumed to be braced by the roof structure. The loadings are imposed from the attic floor and the roof.

Additional support conditions have been included in the model to provide lateral bracing on the gable wall. This will accommodate the influence of the roof structure on the wall. The loadings on the roof and the attic floor have been imposed on a 3-meter strip adjoining the wall. This includes half of the roof structure and the attic floor, which spans six meters.

The behaviour of the wall under the theoretical loadings has indicated whether it is structurally stable in the scenario where full restorations have been done without construction on the wall itself.

5.3 Analysis of the masonry wall

A 3D analytical model has been created to describe the behaviour of the old masonry wall accurately and to compare the stress distribution and estimated deflections with various scenarios. An accurate simulation is essential to achieve suitable results, and verification has been done for each scenario by comparison with the calculated reaction forces. A detailed report outlining the process of generating the accurate old masonry wall model is described in Appendix B.

The finite element model has been developed using Abaqus FEA. The model has been developed as a simplified micro-model, where the individual bricks have been modelled with dimensions including the mortar interface. Each part has been modelled as 3D deformable solid elements to dimensions 220x600x80 mm. Half-brick elements have been modelled to dimensions 110x600x80 mm to fill the edges of the wall. The full- and the half-brick elements are shown in Figure 5.4.

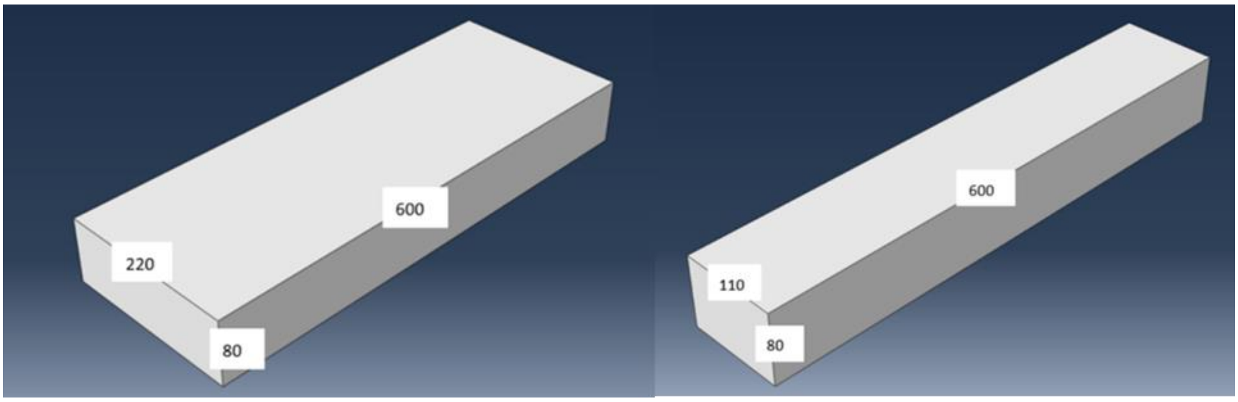

Figure 5.4: Dimensions of Abaqus full-brick (left) and the half-brick part (right)

The material properties have been assigned in Abaqus according to the results obtained from non-destructive testing and laboratory testing. The material has been developed with the density parameter obtained from laboratory testing and the elastic parameters of Poisson's ratio and Young's modulus obtained from non-destructive testing. A total number of 13 separate materials have been created for the model to be assigned to each of the 12 testing zones, with the additional material created and assigned to the gable structure. The material properties of the gable structure have been assumed from the average results obtained from the non-destructive testing. The brick arrangement in the wall is modelled as a standard running bond, as shown in Figure 5.5.

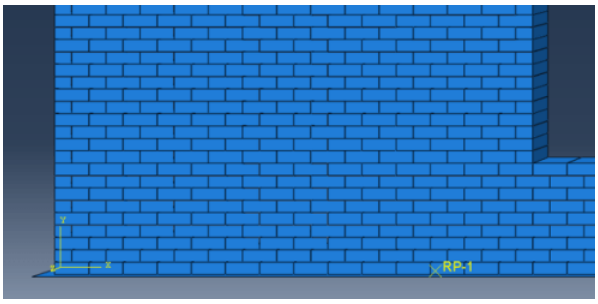

Figure 5.5: Running bond brick arrangement of old masonry wall model

The assembly has been done to the measured dimensions of the old masonry wall. The wall width has been measured as 600 mm, with the width of the wall model shown in Figure 5.6.

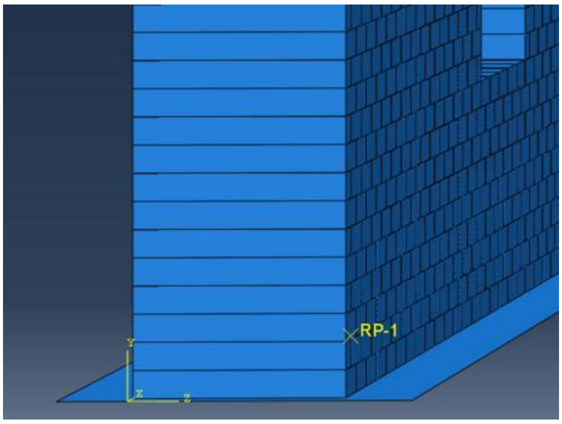

Figure 5.6: Width of old masonry wall model

The material properties have been assumed to be constant throughout the width of the wall, corresponding with the tests done on-site. Due to this, the masonry wall has been modelled as homogeneous parts over the width, with the total width of each part corresponding with the total width of the wall as 600 mm.

The material properties obtained from UPV testing have been incorporated into the model to simulate accurate behaviour. The masonry parts have been assumed to exhibit elastic behaviour, utilising the obtained Poisson's ratio and Young's modulus, with the density to provide self-weight within the model. The density is taken as constant throughout the model as 1445 kg/m³. The material properties obtained from UPV testing are shown in Table 5.1.

Table 5.1: Material properties used in finite element model

Position on wall	**Test position**	**Poisson's ratio**	**Young's modulus (MPa)**
Upper section of right wall panel	UPV1	0,248	4399
	UPV2	0,247	5788
Lower section of right wall panel	UPV3	0,248	6844
	UPV4	0,246	6804
Upper section of centre wall panel	UPV5	0,247	11377
	UPV6	0,216	8667
Lower section of centre wall panel	UPV7	0,247	8728
	UPV8	0,246	12180
Upper section of left wall panel	UPV9	0,243	8535
	UPV10	0,229	6705
Lower section of left wall panel	UPV11	0,247	8807
	UPV12	0,249	10423
Gable above centre wall panel	Gable (Average)	0,243	8271

The simulations scenarios selected include the following:

- Fire damaged model with gravity loading (FDM-G)
- Fire damaged model with gravity and wind loading (FDM-GW)
- Reconstructed model with gravity loading (RM-G)
- Reconstructed model with gravity and wind loading (RM-GW)

The four abovementioned finite element models have been developed for further investigation. The fire damaged model excludes the permanent loading of a roof structure, where the loading is included in the reconstructed model. The accuracy of the simulation has been verified by comparison with the calculated vertical reaction force using static equilibrium equations. The accuracy of each model is shown in Table 5.2.

Table 5.2: Accuracy of each finite element model

Model	Reaction force through static equilibrium calculation	Reaction force through simulation	Accuracy
1. FDM-G	708.0 kN	700.9 kN	98.99%
2. FDM-GW	708.0 kN	703.3 kN	99.34%
3. RM-G	778.6 kN	775.7 kN	99.63%
4. RM-GW	778.6 kN	770.6 kN	98.95%

The accuracy of each model has been determined as above 95%, indicating highly accurate simulations. Further investigation into each model is discussed in the subsequent section.

5.3.1 Fire damaged model – gravity loading

The FDM-G has been developed with no lateral restraint on the gable wall. Internal wall restraints have been included, and the ceiling/attic floor element provides lateral restraint. The roof structure has not been included in the loading action, simulating the model's behaviour in the current condition.

The model has been verified by calculating the reaction force in the Y-direction, which corresponds with the global direction 2 within Abaqus. The simulated reaction force is shown in Figure 5.7.

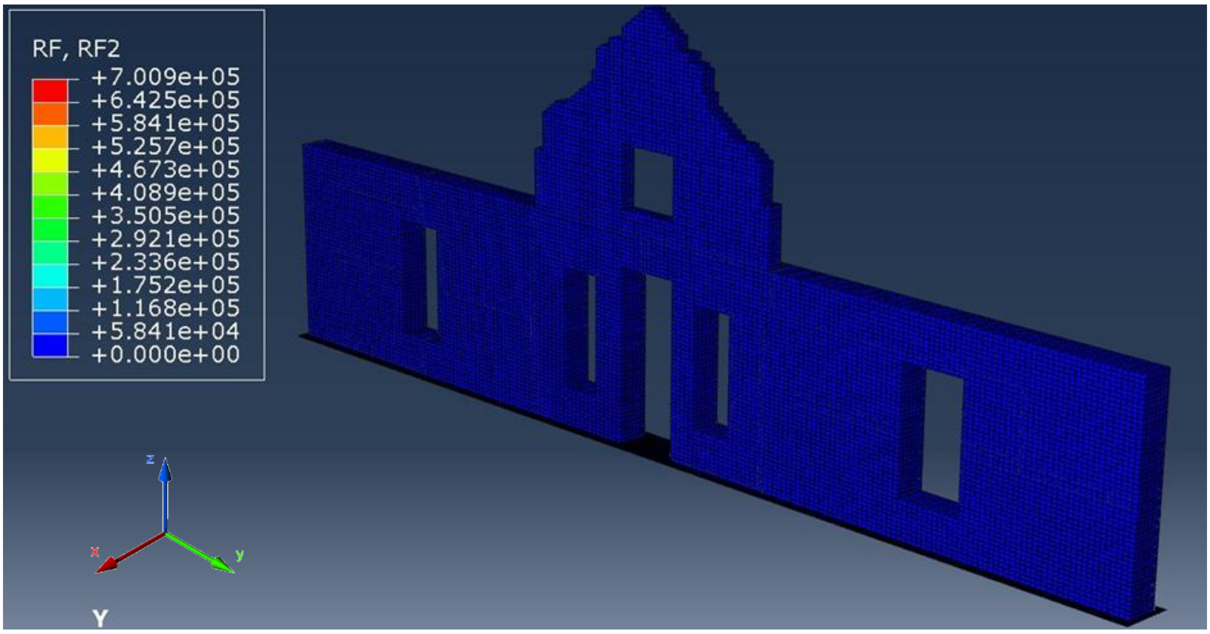

Figure 5.7: Reaction force in N in Y-direction for FDM-G

The simulation produced a reaction force of 700.9 kN, as shown in Figure 5.8. This has been compared with the calculated reaction force and the total weight of the model of 708.0 kN. The accuracy of the simulation is 99%, indicating a highly accurate model, and the stress distribution and expected deflection have been analysed.

The Von Mises stress distribution is shown in Figure 5.8.

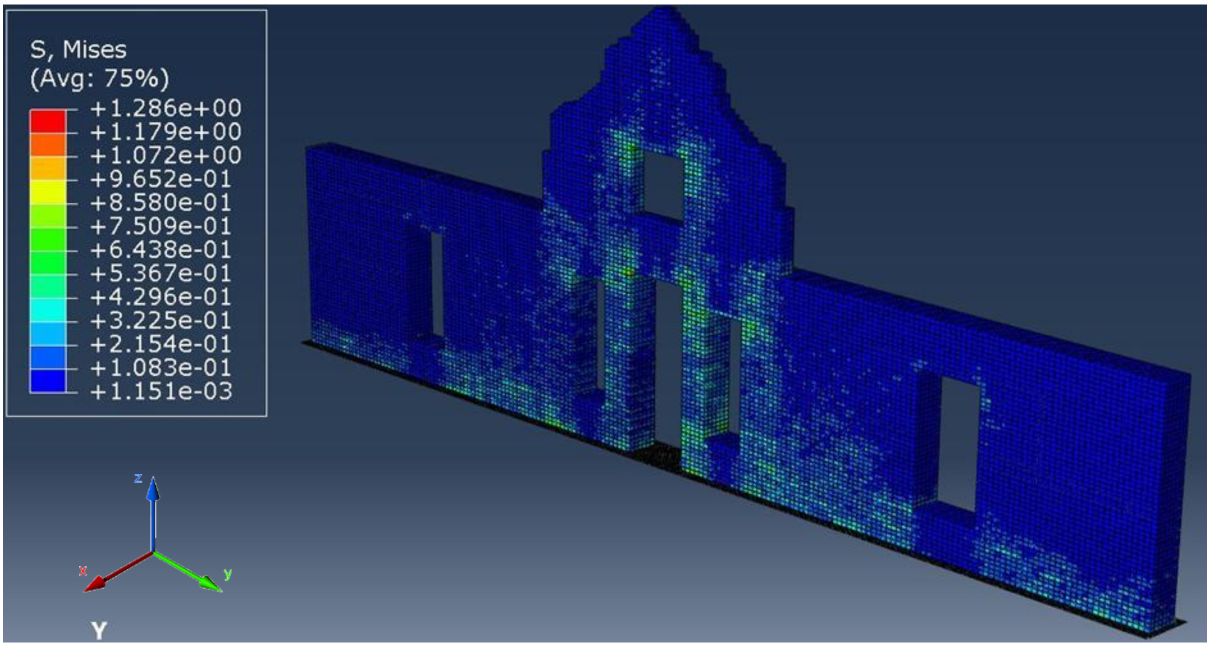

Figure 5.8: Von Mises stress distribution in MPa for FDM-G

The stress distribution indicates localised stress areas distributed mostly around the centre wall panel around the top corners of the window and door openings, and throughout the column areas next to the door openings. The side panels indicate areas of localised stress on the lower sections to the sides of the window openings.

The simulated displacement is shown in Figure 5.9.

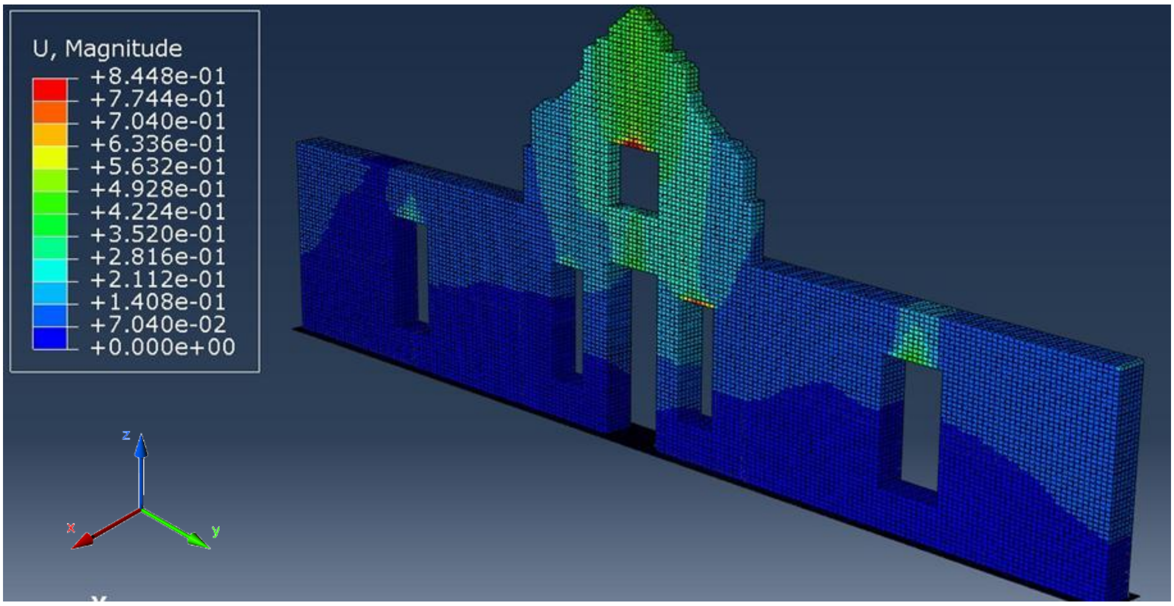

Figure 5.9: Deflection distribution in mm in horizontal direction for FDM-G

The deflection within the model indicates expected localised displacement above all the openings. The highest deflection is noted in the gable wall, due to the unbraced nature. This indicates a higher risk of failure in the future.

5.3.2 Fire damaged model – additional wind loading

A simulation with additional wind loading has been completed to simulate FDM-GW. The wind loading is applied towards the outer face of the wall also and simulates the behaviour of the unbraced gable wall.

The verification has been done by calculating the reaction force in the Y-direction and comparing to the simulated results. The reaction force determined through analysis is shown in Figure 5.10.

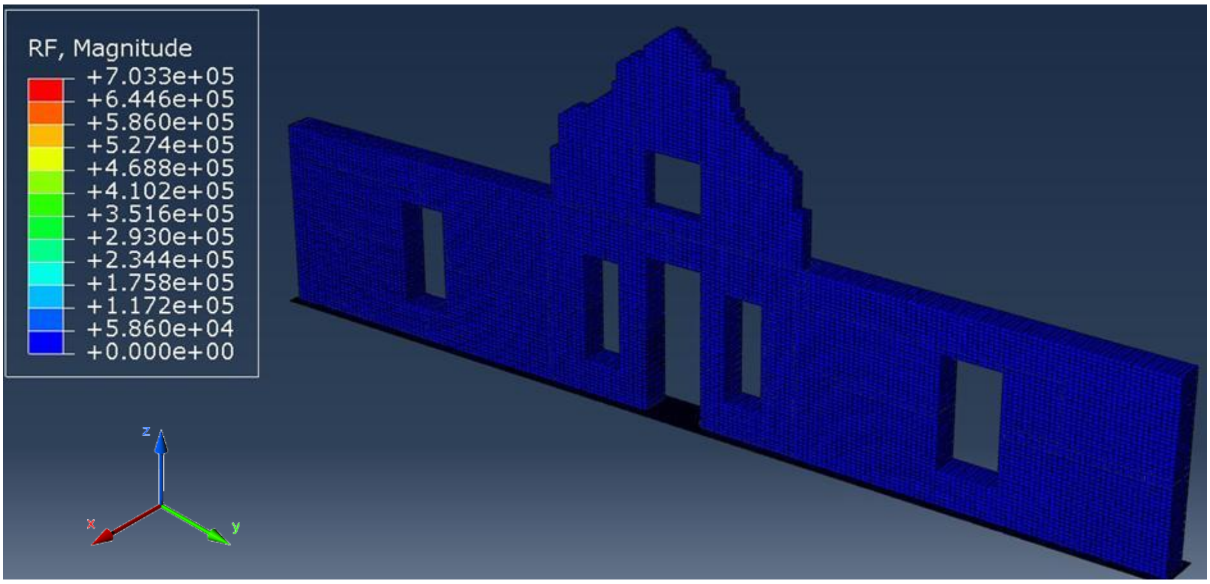

Figure 5.10: Reaction force in N in Y-direction for FDM-GW

With no additional elements imposing self-weight on the model, the reaction force obtained through static equilibrium in the Y-direction is as per the gravity only model as 708.0 kN. As shown in Figure 5.10, the reaction force obtained through analysis is 703.3 kN, providing a model accuracy of 99.3%. The model is therefore assumed to be highly accurate. The Von Mises stress distribution for FDM-GW is shown in Figure 5.11.

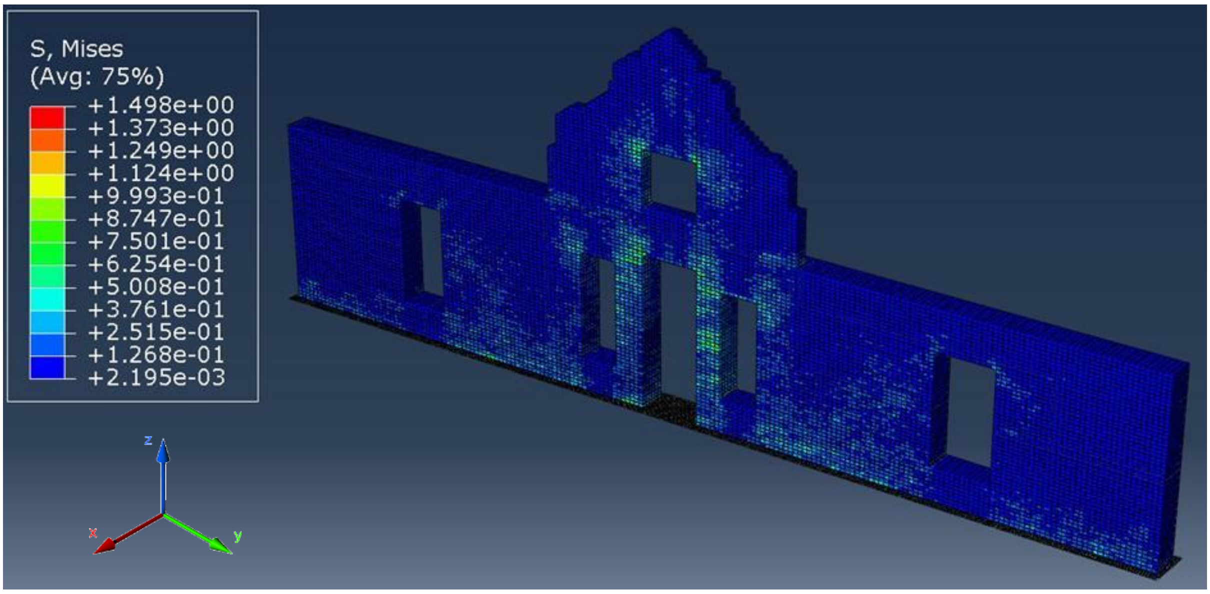

Figure 5.11: Von Mises stress distribution in MPa for FDM-GW

The additional wind loading indicates a higher maximum stress in the model. However, the stress distribution pattern is exceptionally similar when compared to the gravity only simulation. This indicates that the effect of the additional wind load is negligible.

The simulated displacement is shown in Figure 5.12.

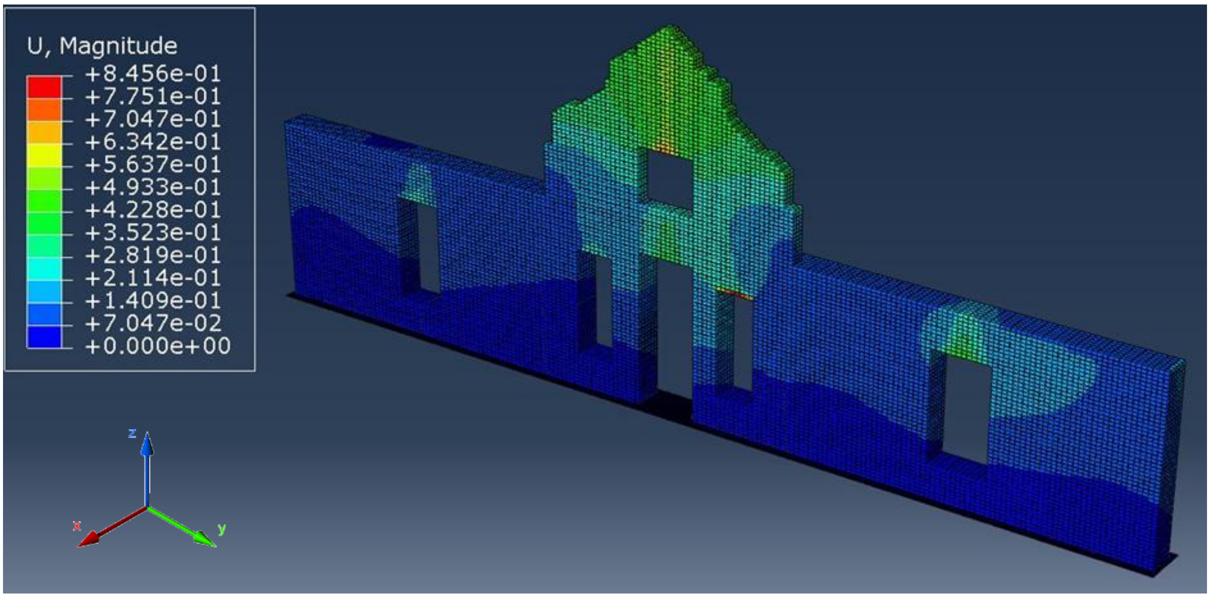

Figure 5.12: Deflection distribution in mm in horizontal direction for FDM-GW

The overall deflection within the model indicates similar values as with the gravity only model. The distribution of the displacement indicates higher movement towards the upper part of the masonry wall and has a more significant influence on the gable wall. This reiterates the severity of the unbraced gable wall as at higher risk of failure in the future.

5.3.3 Reconstructed model – gravity loading

The heritage structure has suffered severe fire damage, and the eventual goal is to provide suitable analytical data that can aid in the restoration and conservation of the building. The old masonry wall has been simulated with the additional self-weight of the roof structure, assuming the roof is reconstructed to the original state. Coupled with the additional self-weight, the roof structure provides more bracing to the gable wall which has been included in the simulation.

The verification of the model has been done by comparing the reaction force in the Y-direction with the calculated reaction force, as per the previous simulations. The reaction force is shown in Figure 5.13.

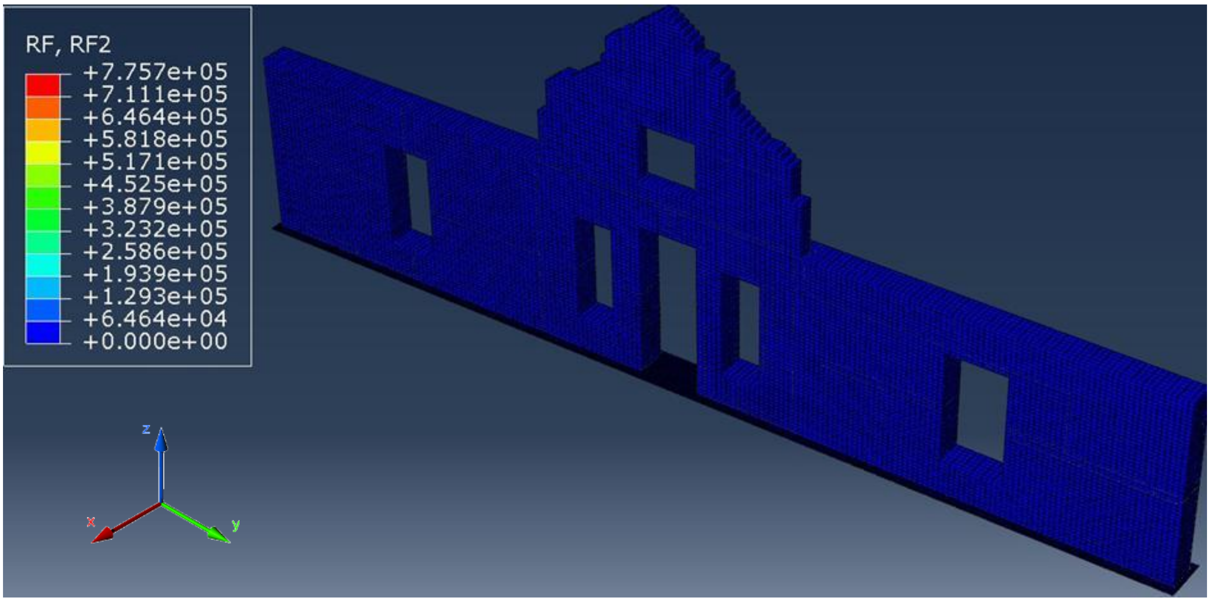

Figure 5.13: Reaction force in N in Y-direction for RM-G

The reaction force on the model has been calculated through static equilibrium equations as 778.0 kN, with the simulation providing a result for the reaction force as 775.7 kN. This has produced a model accuracy of 99.6%, indicating accurate results.

The Von Mises stress distribution is shown in Figure 5.14.

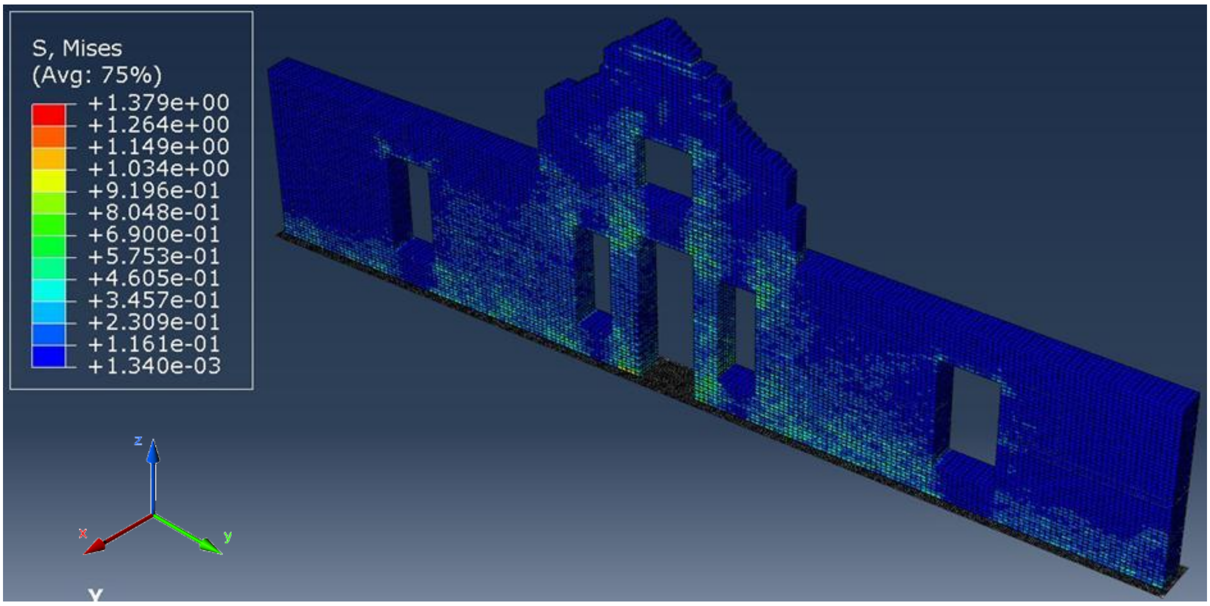

Figure 5.14: Von Mises stress in MPa distribution for RM-G

The stress distribution indicates a lower maximum stress when compared to the damaged model subjected to wind loading but a higher maximum stress when compared to the damaged model subjected to gravity only. The stress distribution indicates a higher density in the stress areas at the corners of the door and window openings. The highest stress values have been located at the column sections next to the door opening, indicating that the internal force flow paths are concentrated towards the model's middle section.

The simulated displacement for RM-G is shown in Figure 5.15.

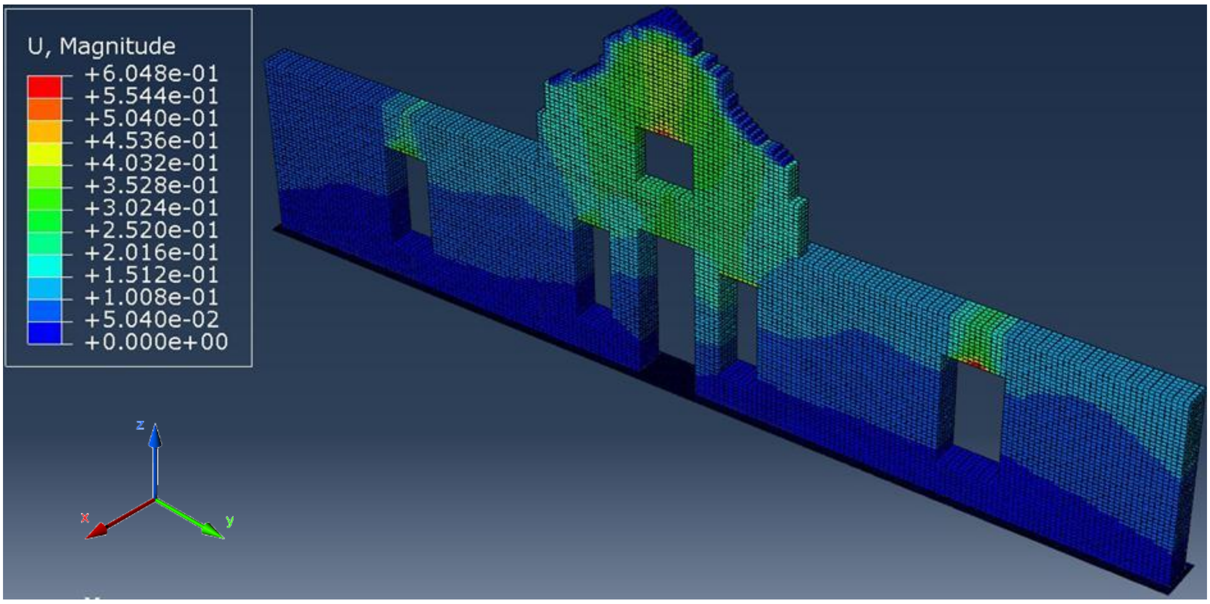

Figure 5.14: Deflection distribution in mm in the horizontal plane for RM-G

The overall deflection for the model has been analysed with a maximum value of approximately 0.6 mm. The displacement distribution throughout the model is higher than the displacement obtained with both models of the damaged model. However, the additional bracing that is provided by the roof structure on the gable visibly reduces the displacement in that area. This indicates that the reconstruction of the roof structure will have a beneficial impact on the masonry wall.

5.3.4 Reconstructed model – additional wind loading

The fully reconstructed heritage structure will be subjected to wind loading in the actual scenario, which introduces the need to develop an analytical model to provide a suitable simulation for this effect. The wind load is applied as it has been for FD-GW, with the additional bracing introduced through the roof structure's reconstruction.

The validation of the model has been done with the calculation of the reaction force in the Y-axis and the comparison of this force with the obtained reaction force through analysis. The simulated reaction force is shown in Figure 5.16.

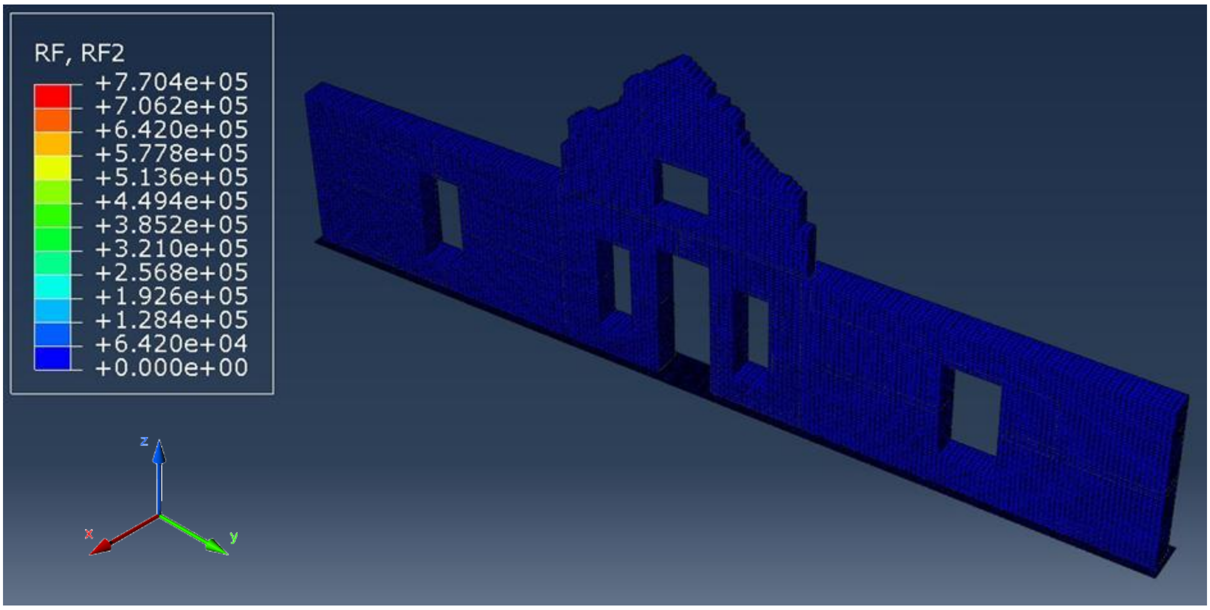

Figure 5.15: Reaction force in N in Y-direction for wind loading on RM-GW

The reaction force obtained from the simulation is shown in Figure 5.16 as 770.4 kN, whereas the reaction force calculated through static equilibrium equations is 778.0 kN. The accuracy of the model is calculated as 98.9%, indicating a highly accurate model.

The Von Mises stress distribution is shown in Figure 5.17.

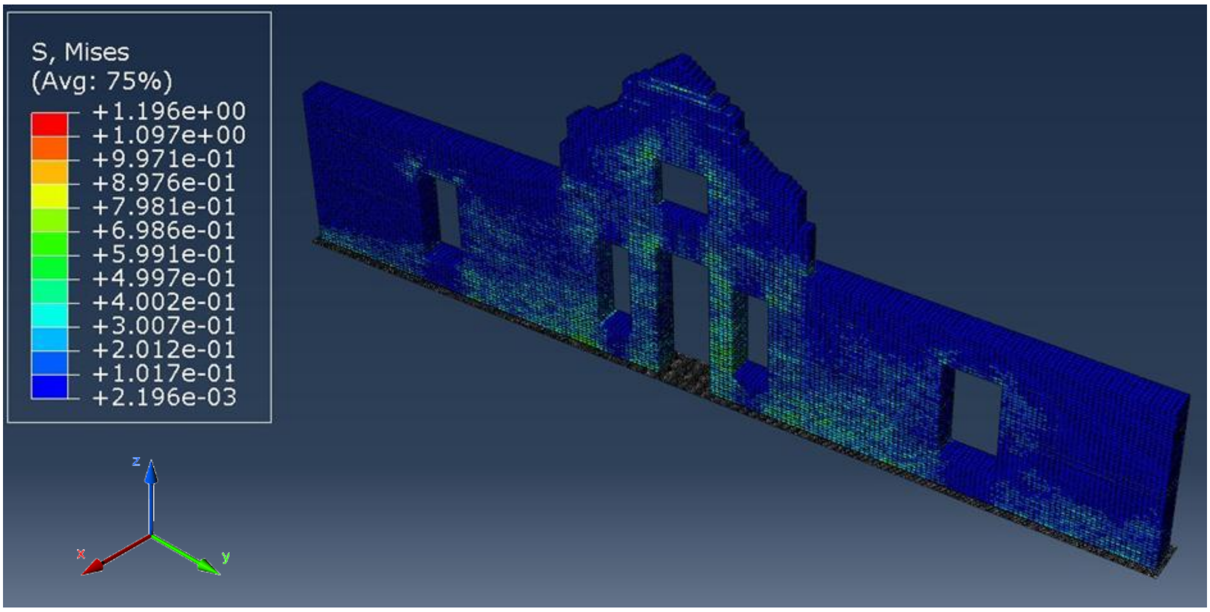

Figure 5.16: Von Mises stress distribution in MPa for RM-GW

The additional bracing provided by the roof structure on the gable wall is shown in Figure 5.17 to reduce the overall stress in the overall masonry wall. The stress distribution is shown to have a higher density in the stress areas compared to the reconstructed model with gravity loading.

The displacement distribution for RM-GW is shown in Figure 5.18.

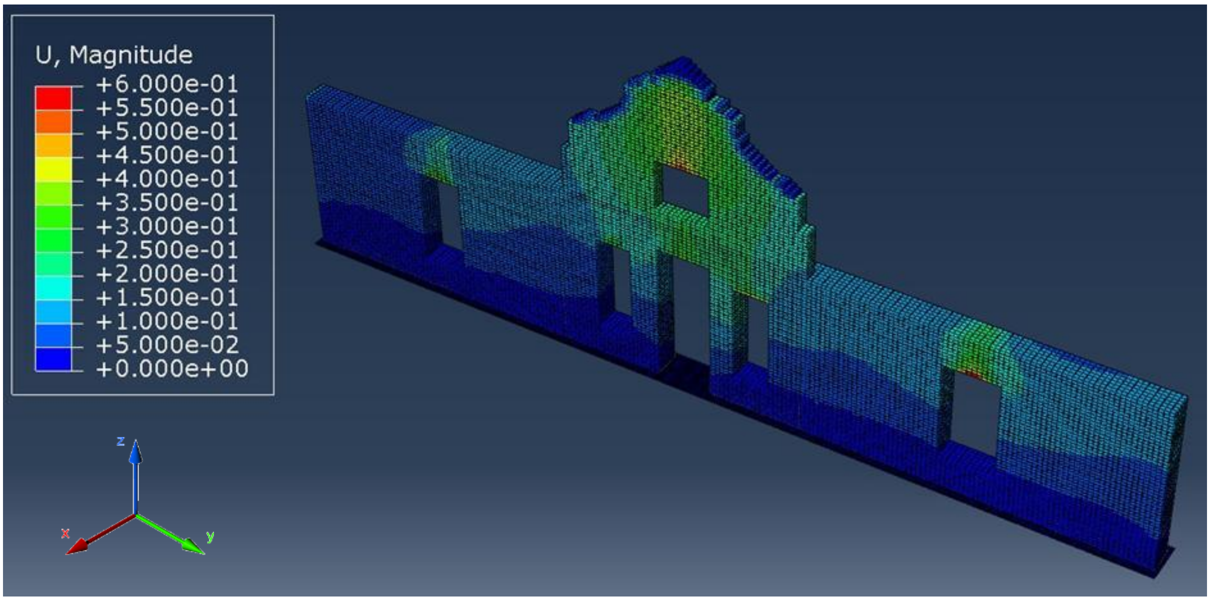

Figure 5.17: Deflection distribution in mm in the horizontal plane for RM-GW

The deflection distribution for RM-GW indicates a near identical result when compared to the reconstructed model subjected to only gravity loading. This indicates that the effect of wind loading does not significantly influence the overall behaviour of the model. This correlates with the results obtained from the effect of the wind loading on the damaged model, where an insignificant effect has been exhibited. Thus, it is evident that the structure's self-weight is the governing factor in determining the overall stress. However, it has been shown that the unbraced gable wall is at risk of failure with or without the additional wind loading should no remedial action be taken.

5.4 Conclusion

Finite element modelling has provided accurate simulations of existing structures, especially when unorthodox and varying material properties are used. The gable wall of the Non-Pareille manor house has been modelled using ABAQUS software. The material properties obtained through non-destructive testing have been incorporated into the model to simulate accurate loading response.

The finite element model was developed by adopting a quasi-static approach to ensure solvability and accuracy. Four separate analysis scenarios were simulated – the current condition of the wall with and without wind loading and the wall with a reconstructed roof with and without wind loading.

The four scenarios have produced sufficient results to describe the current condition of the masonry wall and to develop data for further discussion.

Chapter 6 RESULTS & DISCUSSION

This chapter presents the findings that have been obtained throughout this research, through two phases: firstly, through non-destructive testing, which includes laboratory testing; and secondly, through the development of a finite model. Before testing, site-specific data has been obtained to provide insight into the specific structure. The selected wall has been inspected visually, followed by rebound hammer testing and ultrasonic pulse velocity testing. Masonry samples obtained from the site have been tested in a laboratory to provide control data. The test results have been further analysed to be incorporated into the development of a finite element model, which has been done using ABAQUS FEA. All the findings will be discussed in detail, and the finite model will be described in this chapter.

6.1 Rebound hammer testing

Rebound hammer testing has been conducted on the wall to determine the surface hardness of the material used in the wall's construction. This has been done as per the methodology set out in Chapter 4 on the testing zones determined through visual inspection.

To obtain accurate results for masonry, additional calibration has been done in a laboratory on samples obtained from the site. The Ectha Pro test equipment that has been used to conduct the testing is calibrated for testing on material. This is compared with the compressive strength tests to provide a correlation with the site-specific material.

The compressive strength distribution has been displayed utilising a contour diagram imposed on the wall. This gives a visual representation of the areas on the wall and the overall surface strength distribution. The contour diagram is shown in Figure 6.1.

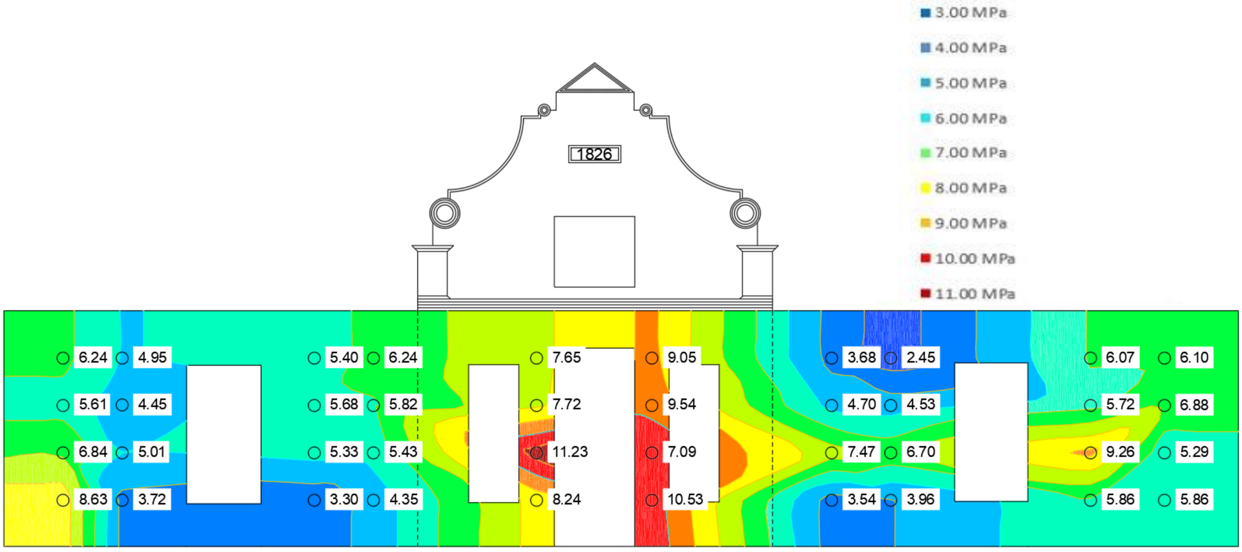

Figure 6.1: Compressive strength distribution of the wall in MPa

The compressive strength distribution is indicated in Figure 6.1, ranging from low to high values in the spectrum of blue to red. The lowest compressive strength of 2.45 MPa is determined at the top portion of the west wall panel, with the highest compressive strength of 11.23 MPa located on the centre wall panel.

The results have been reduced to the average compressive strength for each testing zone. The average compressive strength obtained from rebound hammer testing for each testing zone is shown in Figure 6.2.

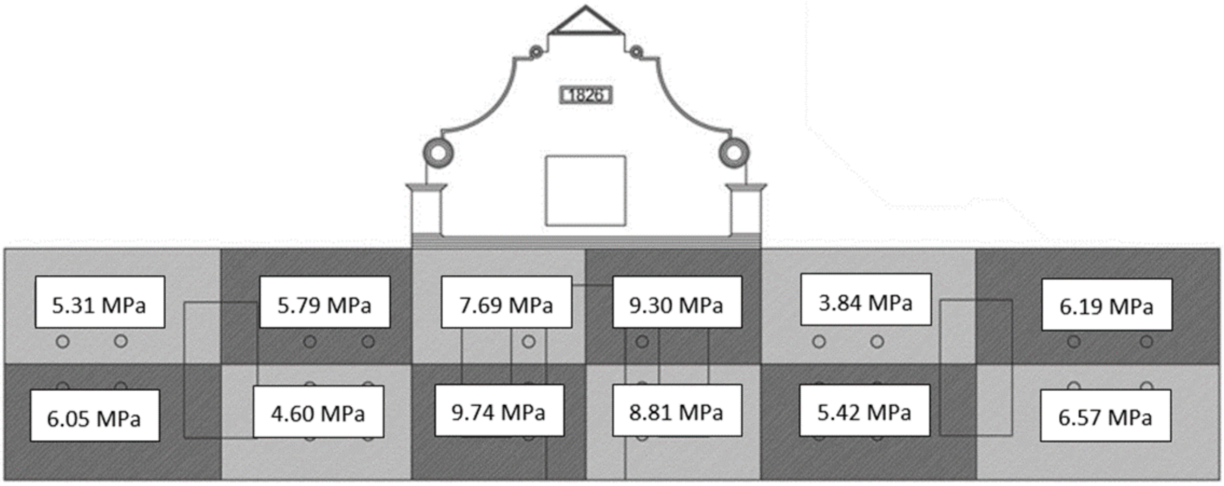

Figure 6.2: Average compressive strength for each testing zone on the wall

It is evident from Figure 6.2 that the centre wall panels have a higher average compressive strength in comparison with the east and the west wall panels. The increased strength in these areas can be attributed to the walls next to the front door constructed as masonry columns instead of load-bearing masonry walls, as per the east and west wall panels. Further results and material properties for the test zones have been described through ultrasonic pulse velocity testing in the subsequent section.

6.2 Ultrasonic pulse velocity testing

Ultrasonic pulse velocity has been conducted on the wall to determine the velocity of the pulse in the longitudinal direction through the wall and the transverse direction on the surface of the wall. Testing has been conducted in the transverse direction over the cracks on the wall surface to determine the overall depth of each crack. The testing has been done as per the methodology in Chapter 4 on the testing zones determined through the visual inspection.

The Proceq Pundit Lab test equipment can test multiple materials, with the pulse velocity describing the time of travel of the pulse through the masonry wall. The UPV results have been interpreted through calculations to determine Poisson’s ratio for each test zone. The pulse velocity has been calibrated with the density obtained from the lab testing to calculate Young’s modulus for each test zone. These material properties have been used in developing the finite model.

The results from UPV testing are shown in Figure 6.3.

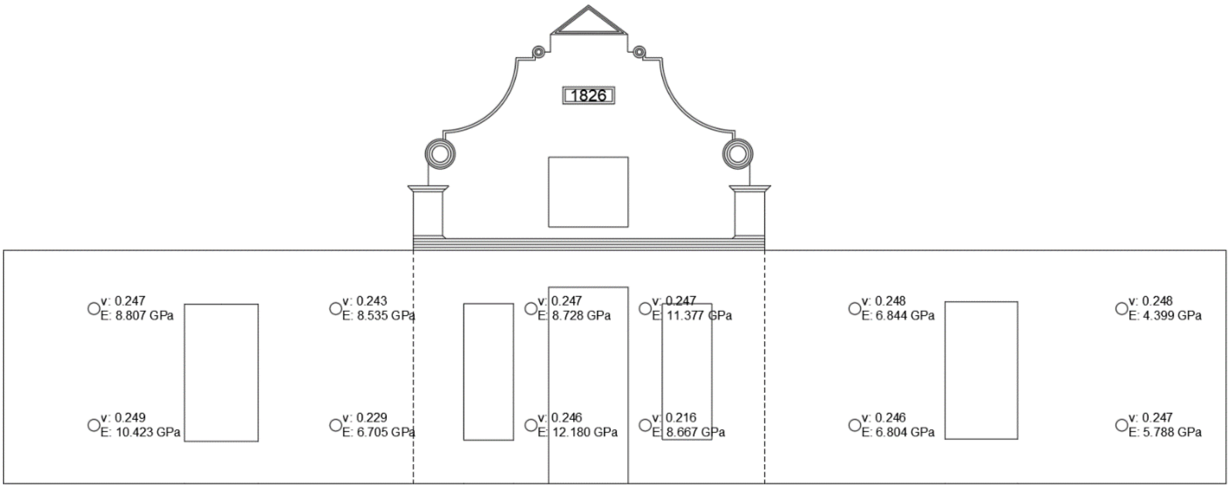

Figure 6.3: UPV results for each position on the wall

The results obtained from UPV testing have been further refined, and the distribution of the calculated values of Poisson's ratio and Young's modulus has been presented. This has been done in contour diagrams developed using linear interpolation. The contour diagrams are shown in Figures 6.4 and 6.5, respectively.

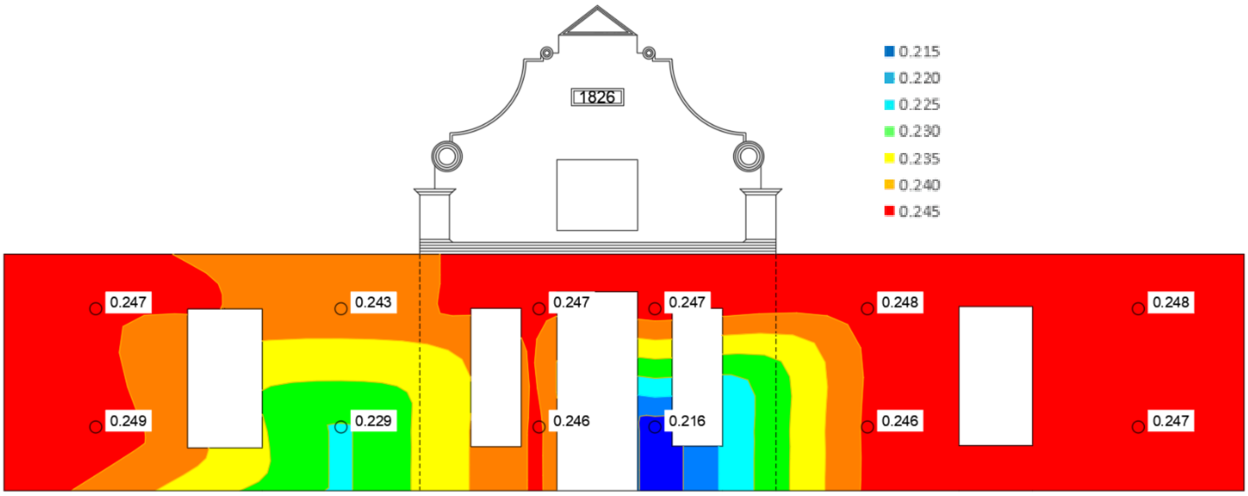

Figure 6.4: Poisson's ratio distribution of old masonry wall

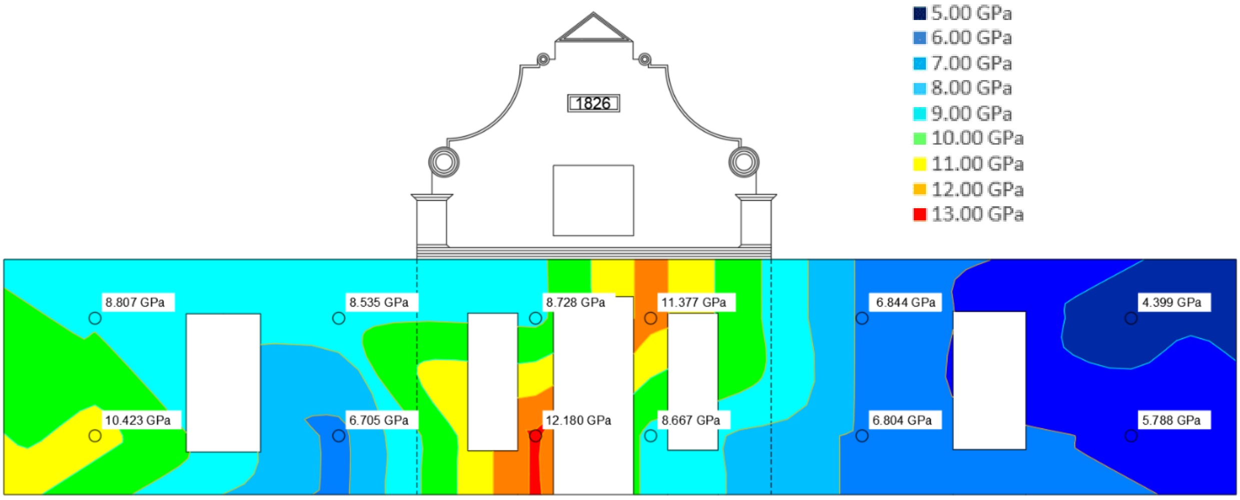

Figure 6.5: Young’s modulus distribution of old masonry wall

A higher Poisson’s ratio has been identified toward the outer edge of the left and right wall panels. The Poisson’s ratio increases towards the approximate centre of the centre panel of the wall. A lower Young’s modulus has been identified on the wall's right panel, and lower values have also been identified through the left panel. The left panel has a higher degree of cracking, which corresponds with lower Young’s modulus. The Young’s modulus increases in magnitude towards the approximate centre of the centre panel. This indicates that Poisson’s ratio is inversely proportional to Young’s modulus throughout the old masonry wall.

Cracks in the wall were identified at 12 positions, and the test locations are visually located on the wall from CD1 to CD12. The positions of these cracks have been graphically plotted, and each crack’s approximate width has been measured with a measuring tape. The crack depth has been determined through UPV testing using the Proceq Pundit Lab equipment. The measured crack width and depth at each position are shown in Table 6.1.

Table 6.1: Measurement of crack depth and crack width on the wall

Crack Depth		
Test Position	Crack Depth through UPV (mm)	Measured Crack Width (mm)
CD1	35	1
CD2	64	1
CD3	135	2
CD4	214	2
CD5	88	2
CD6	37	1
CD7	189	2
CD8	13	1
CD9	622	3
CD10	163	2
CD11	96	2
CD12	12	1

Descriptive statistical analysis was conducted on the results, showing that the data is highly variable and that they are far from the mean due to the high variance. Hence, the depth of cracks varied from a minimum of 12 mm at CD12 to a maximum of 622 mm at CD9, with a mean value of 139 mm. The crack width data show that the range variance is low, and data are close to the mean value. The kurtosis and skewness value shows that the crack width result is quite common, ranging from 1 mm to 3 mm. The statistical analysis is shown in Table 6.2.

Table 6.2: Descriptive statistical analysis of crack width and depth

Crack Depth (mm)		***Crack Width (mm)***	
Mean	139	Mean	1.67
Standard Error	48.09	Standard Error	0.19
Median	92	Median	2
Mode	N/A (no repetitive values)	Mode	2
Standard Deviation	166.60	Standard Deviation	0.65
Sample Variance	27755.09	Sample Variance	0.42
Kurtosis	7.27	Kurtosis	-0.34
Skewness	2.51	Skewness	0.44
Range	610	Range	2
Minimum	12	Minimum	1
Maximum	622	Maximum	3
Sum	1668	Sum	20
Count	12	Count	12

Table 6.2 makes evident that many cracks located on the wall can be classified as minor hairline cracks, with crack widths of less than 1 mm and surface-deep crack depths. More significant cracks have been identified at test positions CD3, CD4, CD5, CD7, CD10 and CD11, with depths protruding over 100 mm deep and crack widths of approximately 2 mm. The critical crack depth has been identified at CD9, where the crack depth has been measured as more than 600 mm, indicating that the crack is over the full width of the wall and a discontinuity in the structure. The cracks are shown in Figure 6.6.

Figure 6.6: Crack depth measurement positions and corresponding crack widths

Crack CD1 and CD2 correspond with the external wall's lateral bracing, whereas CD8, CD10 and CD11 correspond with the internal wall bracing. This could indicate differential horizontal movement within the wall panel, with the most significant cracks identified at CD10 and CD11 due to this. The horizontal cracks at CD3, CD7 and CD12 are located at the lower section of the wall and could indicate increased stresses due to the support provided by this section. Cracks CD4, CD5 and CD6 are located on the perimeter of the window opening on the right wall panel. This could indicate long-term settlement in this area. Crack CD9 indicates a severe structural discontinuity, where the other cracks appear to be only visual. Remediation is recommended to avoid further opening of the crack.

The results obtained through the crack depth determination provide a control to which the model can be compared. Concluding the non-destructive testing, the results obtained provided substantial data to be incorporated into the finite element model. The finite element modelling is elaborated on in the following section.

6.3 Finite element modelling

The results from non-destructive testing have been obtained and described in the previous section. The test methods utilised accurately describe the structure in its current state. However, to develop an accurate finite element model, it is suggested that the modelling outputs are compared to the crack patterns and visual deflection as noted in the visual inspection.

The overall comparison of the stress distribution is shown in Figure 6.7.

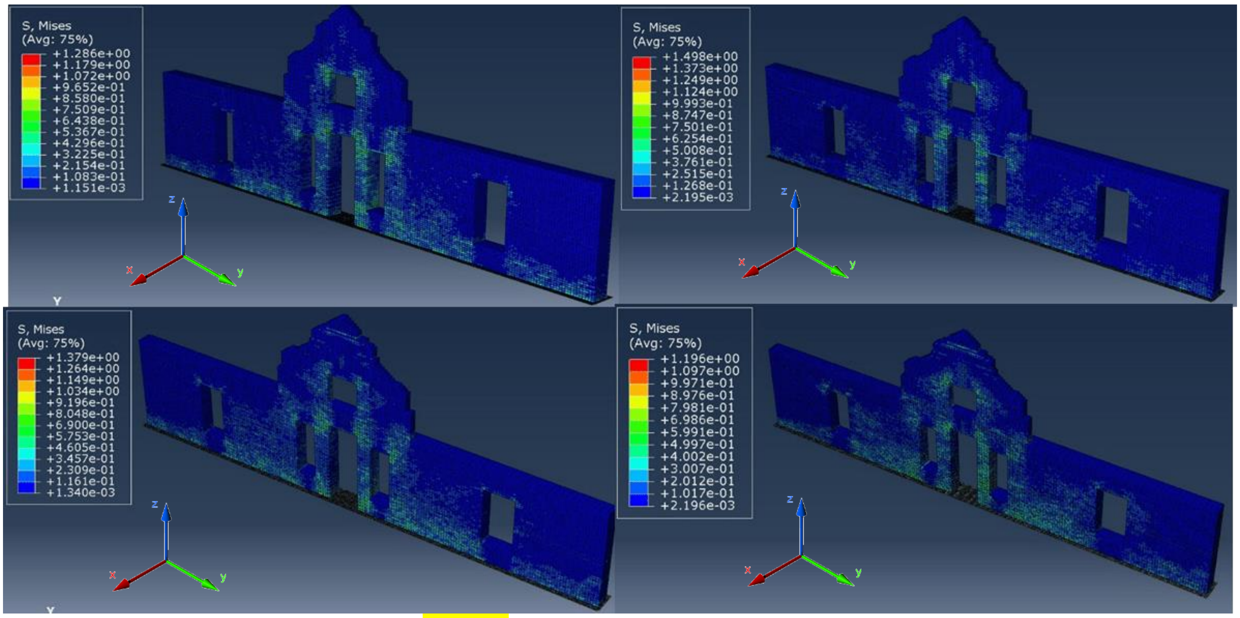

Figure 6.7: Stress distribution in MPa on the wall in current state (top) and the wall with the braced gable (bottom), without wind load (left) and with wind load (right)

The results presented in Figure 6.7 show that the stress patterns between all model scenarios produce similar output. The overall stresses are shown to be higher in the reconstructed model due to the increased gravity loading imposed by the roof structure. The wind loading does not significantly influence the stress distribution of the masonry wall.

The crack patterns in the wall can be attributed to the extreme heat that was generated by the fire in July 2019, as a result of the sustained long-term loading due to the age of the structure, or a combination of the two. The stress distribution for the finite element model does not include the effect of the thermal expansion of the masonry bricks.

The overall comparison of the deflection distribution is shown in Figure 6.8.

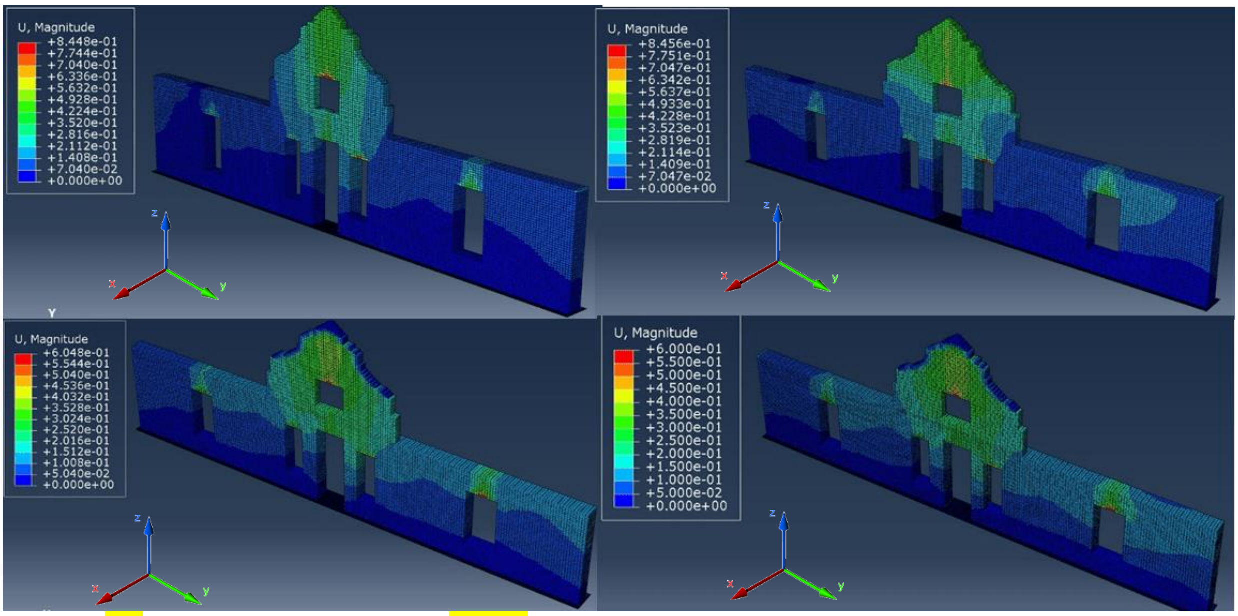

Figure 6.8: Deflection distribution in mm on the wall in current state (top) and the wall with the braced gable (bottom), without wind load (left) and with wind load (right)

A comparison of the deflection results of the various model scenarios shows that the wind load has a negligible influence on the horizontal movement of the wall. It is determined that the overall magnitude of deflection is reduced by approximately 30% where the bracing provided by the roof structure has been included in the simulation. Further comparison of the deflection in isolated directions is made to provide a more accurate description.

The isolated movement in the x-direction (U3) for each model simulation is shown in Figure 6.9.

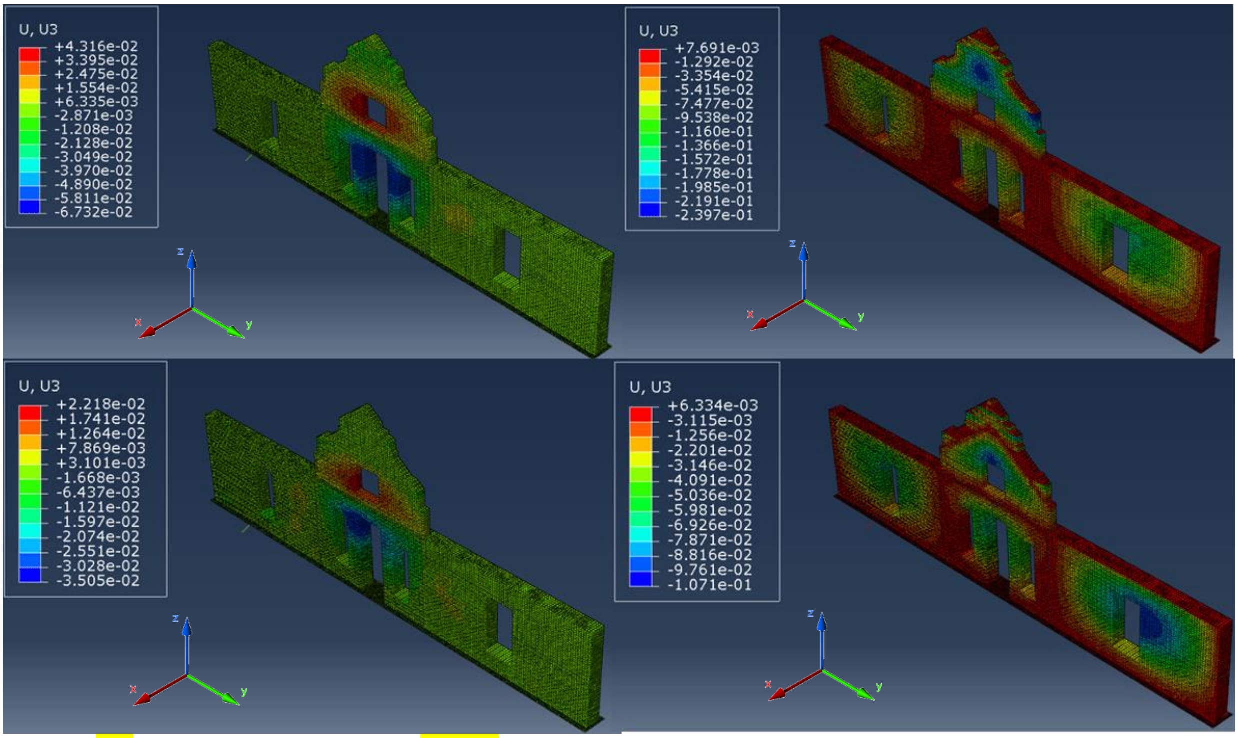

Figure 6.9: Horizontal deflection in mm on the wall in its current state (top) and the wall with the braced gable (bottom), without wind load (left) and with wind load (right)

The horizontal deflection distribution shown in Figure 6.9 indicates an approximate reduction in deflection by 49% and 58% between the damaged and reconstructed models, respectively. Further, the model indicates an out-of-plane deflection in the gable wall, which is more significant in the damaged model with no wind loading. This accurately corresponds to the actual behaviour of the gable wall, as shown in Figure 6.10.

Figure 6.10: Out-of-plane deflection above the architectural ridge of the gable wall

The horizontal, out-of-plane deflection of the gable wall, as shown with the analytical model and the visual inspection, is a cause for concern for the entire wall. As shown in Figure 6.10, the damaged wall has a higher horizontal deflection than the reconstructed wall. Thus, it is assumed that the roof structure's reconstruction will provide adequate lateral bracing to the gable wall to reduce the possibility of out-of-plane failure.

6.4 Conclusion

This chapter has described the results obtained through non-destructive testing and finite element analysis. The results obtained through non-destructive testing were used to determine the compressive strength throughout the old masonry wall and to calculate Young’s modulus and Poisson’s ratio distributed throughout the wall. The in-situ results and density measurement were calibrated through laboratory testing.

The material properties of the old masonry wall have been extrapolated from the results obtained through non-destructive testing, and the properties have been incorporated in the finite element model, following the successful analysis of four scenarios: the damaged wall in its current condition and the reconstructed wall, each with an applied wind load and without an applied wind load. The model accuracy was verified through the variation of the simulated reaction force with the calculated reaction force. The Von Mises stress distribution and the displacement in the wall have been simulated.

It was found that the applied wind load has a minor influence on the overall stress distribution. However, the additional wind loading introduces higher deflections within the gable wall where the roof structure has been damaged. The reconstruction of the roof model reduces the overall simulated deflection with approximately 30%, indicating the need for bracing to be provided to the gable wall. The gable wall also exhibits out-of-plane bending, which is indicated in the finite element model. The cracking identified through visual inspection falls within the stress zones of the finite element model or areas of higher deflection.

The finite element model developed provides accurate data to correlate the actual behaviour of the wall and reiterates the need for remedial action, especially the reconstruction of the roof structure. This will have a minor effect on the stresses within the wall and will reduce the estimated deflection of the gable wall, essentially reducing the risk of failure.

Chapter 7 CONCLUSIONS & RECOMMENDATIONS

This research has aimed to study the fire-damaged manor house at the Non-Pareille farmlands in Dal Josafat, Paarl, through non-destructive testing and finite element modelling. The non-destructive testing has been completed on the front gable wall following a comprehensive visual inspection of significant damages and crack patterns. A finite model has been developed using the processed results obtained from non-destructive testing, which has been used to further describe the stress distribution throughout the wall at the current state. This chapter summarises the research findings by providing solutions to the research problems. Recommendations are made for further research into the current field.

7.1 Conclusions

Before the commencement of this research, a problem was identified within the field of structural engineering and the conservation of heritage structures. Worldwide, many researchers have focused their attention on the testing, analysis and conservation of heritage structures due to the constant degradation over sustained periods of time. In South Africa, however, this problem is amplified due to the lack of research in the field and the lack of the required skills to maintain and restore the country's heritage structures effectively. This has led to the degradation of several old structures and has prompted urgent intervention.

This research aimed to describe the selected masonry wall of the manor house at the Non-Pareille farmlands, which is classified as a protected heritage structure by SAHRA. This research has been developed based on the following research questions:

- What is the distribution of Young's modulus and Poisson's ratio on the selected masonry wall?
- How are the results from non-destructive testing incorporated into the finite element model?
- What does the finite element model indicate about the stability of the wall?

To address the research questions, methodology has been employed on a multi-step basis. The site features have been identified through visual inspection, which has also been used to conduct planning for non-destructive testing. The non-destructive testing has been done in the form of rebound hammer testing and ultrasonic pulse velocity testing.

The rebound hammer testing has produced the distribution of the rebound number, a dimensionless value, over the wall. The rebound number has been correlated with the compressive strength on the material's surface through lab testing, together with the density measurement. The compressive strength through the wall has been indicated as a distribution ranging from 3.84 MPa to 9.74 MPa. This distribution indicated a higher compressive strength towards the centre panel of the wall, which could be attributed to the long-term settlement within the masonry bricks under load from the gable wall.

Following rebound hammer testing, ultrasonic pulse velocity testing was conducted. This produced the velocity readings required to calculate Poisson's ratio and Youngs modulus through empirical formulae. The Poisson’s ratio ranges between 0.216 and 0.249, and Young’s modulus ranges between 4.339 GPa and 12.180 GPa. These results have been incorporated into the finite element model.

The finite element model has been developed to the actual measurements from the wall, considering the zones in which the testing has been conducted. A total of 12 test zones have been identified and material properties have been assigned for each test zone. The assembly included all the material properties tested and a quasi-static analysis has been completed for the following scenarios:

- Fire-damaged wall in its current condition with only gravity loading (FDM-G)
- Fire-damaged wall in its current condition with gravity and wind loading (FDM-GW)
- Reconstructed wall with gravity loading (RM-G)
- Reconstructed wall with gravity and wind loading (RM-GW)

The analysis produced the stress distribution and the estimated displacement for each simulation scenario. It has been shown that the additional wind loading has a minor influence on the stress distribution. However, the horizontal deflection of the gable wall indicates a higher value because of the imposed wind load. The overall deflection within the masonry wall is approximately 30% lower in the scenario where the roof structure has been reconstructed.

The model has indicated stress zones which correspond with the crack patterns identified through visual inspection. The additional weight from the roof increases the maximum Von Mises stress by approximately 15%. The gable wall is braced with the additional stress imposed by the roof structure. This reduces the lateral displacement of the gable wall, which is currently at risk of collapse.

The results have indicated that while the overall wall is generally stable, the gable is at risk of collapse should no remedial action be taken. The reconstruction of the roof structure is a possible solution to limiting the risk of failure within the wall.

The current research has described the old masonry wall of the Non-Pareille manor house on a detailed and analytical level to determine the current stability and behaviour under load. With the entire structure exposed to severe fire damage, urgent intervention is required to prevent further damage, emphasising the research's significance. The simulated failure method has been described, and the focus areas for remediation have been highlighted, which can introduce a field for further research.

7.2 Recommendations

The research has covered the non-destructive testing and finite element modelling of the old masonry wall, and further studies are recommended to fully describe intricate details of the various elements within the structure. The overall process throughout the research and the results obtained from testing and analysis have provided significant insight into further fields of study. This section discusses the recommendations developed as a result of the current research.

The conservation of heritage structures consists of studies of various fields and expertise, where one section has been studied in this research. This is due to the delineation of the research and time constraints. Further studies are thus recommended to cover all the aspects.

It is recommended that non-destructive testing and finite element modelling be conducted over the entire structure. This can be done following the methodology outlined in the current research. This will provide an accurate and detailed representation of the entire structure and the relation to the results obtained from the current study on the old masonry wall. The actual long-term deflection within the structure can be determined through detailed surveying, providing the necessary data to calibrate the deflection obtained through finite element analysis. This can be coupled with seismic analysis to simulate accurate long term behaviour of the model, as Paarl is situated in a minor seismic zone. The study of the entire structure is required to achieve suitable data for the full reconstruction of the damaged elements.

Effective restoration of historical structures can only be achieved by developing suitable repair material. In the current research, it has been shown through literature that modern construction materials can be incompatible with the existing material, leading to more damage. Thus, material classification is recommended on the existing structure, describing the material on a chemical level. The material classification is used to develop a suitable material to match the existing material, effectively eliminating compatibility issues.

The conservation of historical structures in South Africa, as the ultimate goal, is emphasised by the current lack of research literature from a South African perspective. It is therefore recommended to conduct similar research with other historical structures, in collaboration with SAHRA, to classify and analyse these structures. The data obtained from further research on other historical structures can be used to develop site specific conservation manuals. This can provide building contractors with the critical data if repairs are required.

Following the non-destructive testing and finite element modelling of the masonry wall of the historical Non-Pareille manor house, the wall has been effectively described from a structural perspective. This has concluded an essential step towards the eventual restoration of the structure, which can be completed following further research as recommended. Conducting research into various historically significant structures in South Africa can effectively fill the gap in the field and provide a solution to conserving the country’s rich and valuable heritage.

References

Abdulla, K., Cunningham, L. and Gillie, M., 2017. Simulating masonry wall behaviour using a simplified micro-model approach. *Engineering Structures*, 151, pp. 349-365.

Ahn, E., Kim, H., Sim, S., Shin, S. and Shin, M., 2017. Principles and Applications of Ultrasonic-Based Non-destructive Methods for Self-Healing in Cementitious Materials. *Materials*, 10(3), p. 278.

Akoglu, K., Kotoula, E. and Simon, S., 2020. Combined use of ultrasonic pulse velocity (UPV) testing and digital technologies: A model for long-term condition monitoring memorials in historic Grove Street Cemetery, New Haven. *Journal of Cultural Heritage*, 41, pp. 84-95.

Al-Qadi, I., Leng, Z., Lahouar, S. and Baek, J., 2010. In-Place Hot-Mix Asphalt Density Estimation Using Ground-Penetrating Radar. *Transportation Research Record: Journal of the Transportation Research Board*, 2152(1), pp. 19-27.

Alwash, M., Breysse, D. and Sbartaï, Z., 2015. Non-destructive strength evaluation of concrete: Analysis of some key factors using synthetic simulations. *Construction and Building Materials*, 99, pp. 235-245.

Annecchiarico, M. & Portioli, F., and Landolfo, R., 2010. Micro and macro-finite element modeling of brick masonry panels subject to lateral loadings. *COST ACTION C26: Urban Habitat Constructions under Catastrophic Events - Proceedings of the Final Conference*, pp. 315-320.

Anwar, N. and Najam, F., 2017. *Structural Cross-Sections*. Amsterdam: Butterworth-Heinemann, pp. 1-37.

Atoyebi, O.D., Ayanrinde, O.P. and Oluwafemi, J., 2019. Reliability comparison of Schmidt rebound hammer as a non-destructive test with compressive strength tests for different concrete mix. *Journal of Physics: Conference Series*, 1378(3), pp. 1-9.

Aydin, A.,2013. Upgraded ISRM suggested method for determining sound velocity by ultrasonic pulse transmission technique. *Rock Mechanics and Rock Engineering*, 47(1), pp. 255–259.

Azam, R., Riaz, M., Haq, E., Shihata, A. and Zawam, M., 2022. Development of Quality Assessment Criteria for Burnt Clay Bricks of Different Ages Based on Ultrasonic Pulse Velocity Test. *Buildings*, 12(8), p. 1069.

Binda, L., Saisi, A. and Tiraboschi, C., 2000. Investigation procedures for the diagnosis of historic masonries. *Construction and Building Materials*, 14(4), pp. 199-233.

Bolhassani, M., Hamid, A., Lau, A. and Moon, F., 2015. Simplified micro modeling of partially grouted masonry assemblages. *Construction and Building Materials*, 83, pp. 159-173.

Brencich, A., Bovolenta, R., Ghiggi, V., Pera, D. and Redaelli, P., 2020. Rebound Hammer Test: An Investigation into Its Reliability in Applications on Concrete Structures. *Advances in Materials Science and Engineering*, pp. 1-11.

Breysse, D., Klysz, G., Dérobert, X., Sirieix, C. and Lataste, J., 2008. How to combine several non-destructive techniques for a better assessment of concrete structures. *Cement and Concrete Research*, 38(6), pp. 783-793.

Casarin, F., Valluzzi, M., da Porto, F. and Modena, C., 2007. Evaluation of the structural behaviour of historic masonry buildings by using a sonic pulse velocity method. *Structural Studies, Repairs and Maintenance of Heritage Architecture*, 10(95), pp. 227-236.

Cavalagli, N., Kita, A., Castaldo, V., Pisello, A. and Ubertini, F., 2019. Hierarchical environmental risk mapping of material degradation in historic masonry buildings: An integrated approach considering climate change and structural damage. *Construction and Building Materials*, 215, pp. 998-1014.

D'Altri, A., Milani, G., de Miranda, S., Castellazzi, G. and Sarhosis, V., 2018. Stability analysis of leaning historic masonry structures. *Automation in Construction*, 92, pp. 199-213.

DRC Italia. n.d. *Ectha PRO digital test hammer*. [online] Available at: https://www.drcitalia.it/en/negozio/structural-diagnosis-en/ectha-pro-digital-test-hammer/ [Accessed 14 November 2021].

Eljufout, T., Hadadin, N., Haddad, A. and Alhomaidat, F., 2022. Correlation models for utilising rebound hammer technique in evaluating weathered limestone walls. *Australian Journal of Structural Engineering*, pp. 1-11.

Engineersdaily. 2011. *Rebound Hammer Test*. [online] Available at: https://www.engineersdaily.com/2011/04/rebound-hammer-test.html [Accessed 14 November 2021].

Fanaie, N., Esfahani, F.G. and Soroushnia, S., 2015. Analytical study of composite beams with different arrangements of channel shear connectors. *Steel and Composite Structures*, 19(2), pp. 485–501.

Fransen, H., 2004. The old buildings of the Cape. *A survey of extant architecture from before c1910 in the area of Cape Town - Calvinia - Colesberg - Uitenhage*. Johannesburg and Cape Town: Jonathan Ball Publishers, pp. 295-296.

Heyman, J., 1969. The safety of masonry arches. *International Journal of Mechanical Sciences*, 11(4), pp. 363-385.

Illampas, R., Silva, R., Charmpis, D., Lourenço, P. and Ioannou, I., 2017. Validation of the repair effectiveness of clay-based grout injections by lateral load testing of an adobe model building. *Construction and Building Materials*, 153, pp. 174-184.

International Atomic Energy Agency, 2002. Guidebook on Non-Destructive Testing of Concrete Structures. Vienna: *International Atomic Energy Agency*.

IS 13311-1(1992), 1992. Non-Destructive Testing of Concrete - Methods of Test part 1: Ultrasonic Pulse Velocity. New Delhi, *Bureau of Indian Standards*.

Jiao, J., Xia, Q. and Shi, F., 2019. Non-destructive inspection of a brick–timber structure in a modern architectural heritage building: Lecture Hall of the Anyuan Miners' Club, China. *Frontiers of Architectural Research*, 8(3), pp. 348-358.

Kulkarni, P. and Admane, S., 2015. Recommendation for systematic and precise framework of structural audit of residential building. *International Journal of Emerging Trends in Engineering and Development,* 3(5), pp. 456-463.

Kujawa, M., Lubowiecka, I. and Szymczak, C., 2020. Finite element modelling of a historic church structure in the context of a masonry damage analysis. *Engineering Failure Analysis*, 107, p. 104233.

Kumar, A. and Pallav, K., 2020. Experimental and Numerical Investigation of Old Masonry Wall Using a Macro-Modeling Approach. *The Open Civil Engineering Journal*, 14(1), pp. 334-349.

Loke, M., Pallav, K. and Haldenwang, R., 2019. The sustainable restoration of historic masonry: Robben Island [Poster]. *Cape Peninsula University of Technology*, Cape Town.

Lourenço, P., Rots, J. and Blaauwendraad, J., 1995. Two approaches for the analysis of masonry structures: Micro and macro-modeling. *HERON*, 40(4), pp. 313-340.

Merzoug, W., Chergui, S. and Cheikh Zouaoui, M., 2020. The impact of reinforced concrete on the modern-day architectural heritage of Algeria. *Journal of Building Engineering*, 30, p. 101210.

National Geophysical Data Center, nd. NCEI/WDS Global Significant Earthquake Database. United States of America: *NOAA National Centers for Environmental Information*.

Nnaji, C., Amadi, U. and Molokwu, R., 2016. Investigative Study of Biodeterioration of External Sandcrete/Concrete Walls in Nigeria. *Research Journal of Environmental Toxicology*, 10(2), pp. 88-99.

Pacheco-Torgal, F., 2014. Eco-efficient construction and building materials research under the EU Framework Programme Horizon 2020. *Construction and Building Materials*, 51, pp. 151-162.

Pearse, G., 1973. *Eighteenth century architecture in South Africa*. London: Architectural Press, p. 18.

Prizeman, O., Sarhosis, V., D’Alri, A., Whitman, C. and Muratore, G., 2017. Modelling from the past: the leaning soutwest tower ofcaerphilly castle 1539-2015. *ISPRS Annals of the Photogrammetry, Remote Sensing and Spatial Information Sciences*, IV-2/W2, pp. 221-227.

Rao, S., Sravana, P. and Rao, T., 2016. Experimental studies in Ultrasonic Pulse Velocity of roller compacted concrete pavement containing fly ash and M-sand. *International Journal of Pavement Research and Technology*, 9(4), pp. 289-301.

Rebound hammer test on concrete, 2018. *The Constructor*. [online] Available at: https://theconstructor.org/concrete/rebound-hammer-test-concrete-ndt/2837/ [Accessed: November 14, 2021].

Riggio, M., D'Ayala, D., Parisi, M. and Tardini, C., 2018. Assessment of heritage timber structures: Review of standards, guidelines and procedures. *Journal of Cultural Heritage*, 31, pp. 220-235.

Russo, S., 2017. Simplified procedure for structural integrity's evaluation of monuments in constrained context: The case of a Buddhist Temple in Bagan (Myanmar). *Journal of Cultural Heritage*, 27, pp. 48-59.

SAHRA. n.d. *South Africa's National Heritage Sites.* Available at: https://www.sahra.org.za/national-sites/ [Accessed in April 2020].

Saloustros, S., Pelà, L., Cervera, M. and Roca, P., 2017. An Enhanced Finite Element Macro-Model for the Realistic Simulation of Localized Cracks in Masonry Structures: A Large-Scale Application. *International Journal of Architectural Heritage*, 12(3), pp. 432-447.

Statistics SA. 2019. *SA's Tourism Trade Balance Edges Lower*. Available at: http://www.statssa.gov.za/?p=12805 [Accessed 16 April 2020].

Tampone, G. and Ruggieri, N., 2016. State-of-the-art technology on conservation of ancient roofs with timber structure. *Journal of Cultural Heritage*, 22, pp. 1019-1027.

Ultrasonic Testing of Concrete (2021). *FPrimeC Solutions Inc.* [online] Available at: https://www.fprimec.com/ultrasonic-testing-of-concrete/ [Accessed 17 October 2021].

University of Cambridge DoITPoMS. 2016. *Nodes, elements, degrees of freedom and boundary conditions.* [online] Available at: https://www.doitpoms.ac.uk/tlplib/fem/node.php [Accessed 19 December 2021].

Van der Walt, L., 2016. *Non-Pareille Manor House front gable.* [online] Available at: https://www.theheritageportal.co.za/thread/non-pareille-dal-josaphat-western-cape [Accessed 7 November 2021].

Varma, M., Jangid, R. and Ghosh, S., 2010. Thrust Line Using Linear Elastic Finite Element Analysis for Masonry Structures. *Advanced Materials Research*, 133-134, pp. 503-508.

Verma, S., Bhadauria, S. and Akhtar, S., 2013. Review of Non-destructive Testing Methods for Condition Monitoring of Concrete Structures. *Journal of Construction Engineering*, pp. 1-11.

Appendices

Appendix A. Rebound hammer testing expanded raw results

Table A.1: Expanded results for rebound hammer testing

Project Name	Position	Measurement	Angle	Rebound number (R_n)
RV_DAL01	RH1	1	0	25
RV_DAL01	RH1	2	0	23
RV_DAL01	RH1	3	0	23
RV_DAL01	RH1	4	0	22
RV_DAL01	RH1	5	0	21
RV_DAL01	RH1	6	0	23
RV_DAL01	RH1	7	0	23
RV_DAL01	RH1	8	0	24
RV_DAL01	RH1	9	0	25
RV_DAL01	RH1	10	0	31
RV_DAL01	RH1	11	0	30
RV_DAL01	RH1	12	0	23
RV_DAL01	RH1	13	0	23
RV_DAL01	RH1	14	0	22
RV_DAL01	RH1	15	0	22
RV_DAL01	RH1	16	0	20
RV_DAL01	RH2	1	0	21
RV_DAL01	RH2	2	0	24
RV_DAL01	RH2	3	0	27
RV_DAL01	RH2	4	0	21
RV_DAL01	RH2	5	0	26
RV_DAL01	RH2	6	0	30
RV_DAL01	RH2	7	0	33
RV_DAL01	RH2	8	0	27
RV_DAL01	RH2	9	0	23
RV_DAL01	RH2	10	0	24
RV_DAL01	RH2	11	0	22
RV_DAL01	RH2	12	0	21
RV_DAL01	RH2	13	0	26
RV_DAL01	RH2	14	0	28
RV_DAL01	RH2	15	0	25
RV_DAL01	RH2	16	0	24
RV_DAL01	RH3	1	0	22
RV_DAL01	RH3	2	0	22
RV_DAL01	RH3	3	0	23
RV_DAL01	RH3	4	0	22

Project Name	Position	Measurement	Angle	Rebound number (R_n)
RV_DAL01	RH3	5	0	21
RV_DAL01	RH3	6	0	21
RV_DAL01	RH3	7	0	24
RV_DAL01	RH3	8	0	22
RV_DAL01	RH3	9	0	22
RV_DAL01	RH3	10	0	22
RV_DAL01	RH3	11	0	21
RV_DAL01	RH3	12	0	23
RV_DAL01	RH3	13	0	26
RV_DAL01	RH3	14	0	21
RV_DAL01	RH3	15	0	24
RV_DAL01	RH3	16	0	21
RV_DAL01	RH4	1	0	22
RV_DAL01	RH4	2	0	23
RV_DAL01	RH4	3	0	25
RV_DAL01	RH4	4	0	26
RV_DAL01	RH4	5	0	26
RV_DAL01	RH4	6	0	24
RV_DAL01	RH4	7	0	23
RV_DAL01	RH4	8	0	21
RV_DAL01	RH4	9	0	20
RV_DAL01	RH4	10	0	24
RV_DAL01	RH4	11	0	24
RV_DAL01	RH4	12	0	22
RV_DAL01	RH4	13	0	21
RV_DAL01	RH4	14	0	22
RV_DAL01	RH4	15	0	26
RV_DAL01	RH4	16	0	24
RV_DAL01	RH5	1	0	21
RV_DAL01	RH5	2	0	24
RV_DAL01	RH5	3	0	25
RV_DAL01	RH5	4	0	20
RV_DAL01	RH5	5	0	21
RV_DAL01	RH5	6	0	27
RV_DAL01	RH5	7	0	27
RV_DAL01	RH5	8	0	28
RV_DAL01	RH5	9	0	23
RV_DAL01	RH5	10	0	21
RV_DAL01	RH5	11	0	26
RV_DAL01	RH5	12	0	24
RV_DAL01	RH5	13	0	21
RV_DAL01	RH5	14	0	23

Project Name	Position	Measurement	Angle	Rebound number (R_n)
RV_DAL01	RH5	15	0	26
RV_DAL01	RH5	16	0	22
RV_DAL01	RH6	1	0	20
RV_DAL01	RH6	2	0	19
RV_DAL01	RH6	3	0	19
RV_DAL01	RH6	4	0	24
RV_DAL01	RH6	5	0	27
RV_DAL01	RH6	6	0	26
RV_DAL01	RH6	7	0	24
RV_DAL01	RH6	8	0	21
RV_DAL01	RH6	9	0	27
RV_DAL01	RH6	10	0	26
RV_DAL01	RH6	11	0	24
RV_DAL01	RH6	12	0	23
RV_DAL01	RH6	13	0	19
RV_DAL01	RH6	14	0	24
RV_DAL01	RH6	15	0	26
RV_DAL01	RH6	16	0	20
RV_DAL01	RH7	1	0	29
RV_DAL01	RH7	2	0	30
RV_DAL01	RH7	3	0	29
RV_DAL01	RH7	4	0	29
RV_DAL01	RH7	5	0	28
RV_DAL01	RH7	6	0	29
RV_DAL01	RH7	7	0	30
RV_DAL01	RH7	8	0	28
RV_DAL01	RH7	9	0	28
RV_DAL01	RH7	10	0	28
RV_DAL01	RH7	11	0	31
RV_DAL01	RH7	12	0	31
RV_DAL01	RH7	13	0	27
RV_DAL01	RH7	14	0	30
RV_DAL01	RH7	15	0	32
RV_DAL01	RH7	16	0	31
RV_DAL01	RH8	1	0	25
RV_DAL01	RH8	2	0	26
RV_DAL01	RH8	3	0	27
RV_DAL01	RH8	4	0	23
RV_DAL01	RH8	5	0	22
RV_DAL01	RH8	6	0	22
RV_DAL01	RH8	7	0	23

Project Name	Position	Measurement	Angle	Rebound number (R_n)
RV_DAL01	RH8	8	0	21
RV_DAL01	RH8	9	0	24
RV_DAL01	RH8	10	0	22
RV_DAL01	RH8	11	0	25
RV_DAL01	RH8	12	0	23
RV_DAL01	RH8	13	0	23
RV_DAL01	RH8	14	0	22
RV_DAL01	RH8	15	0	21
RV_DAL01	RH8	16	0	24
RV_DAL01	RH9	1	0	15
RV_DAL01	RH9	2	0	15
RV_DAL01	RH9	3	0	16
RV_DAL01	RH9	4	0	19
RV_DAL01	RH9	5	0	16
RV_DAL01	RH9	6	0	16
RV_DAL01	RH9	7	0	17
RV_DAL01	RH9	8	0	17
RV_DAL01	RH9	9	0	19
RV_DAL01	RH9	10	0	18
RV_DAL01	RH9	11	0	19
RV_DAL01	RH9	12	0	18
RV_DAL01	RH9	13	0	22
RV_DAL01	RH9	14	0	15
RV_DAL01	RH9	15	0	13
RV_DAL01	RH9	16	0	21
RV_DAL01	RH10	1	0	18
RV_DAL01	RH10	2	0	22
RV_DAL01	RH10	3	0	15
RV_DAL01	RH10	4	0	21
RV_DAL01	RH10	5	0	12
RV_DAL01	RH10	6	0	24
RV_DAL01	RH10	7	0	23
RV_DAL01	RH10	8	0	24
RV_DAL01	RH10	9	0	21
RV_DAL01	RH10	10	0	20
RV_DAL01	RH10	11	0	20
RV_DAL01	RH10	12	0	26
RV_DAL01	RH10	13	0	24
RV_DAL01	RH10	14	0	22
RV_DAL01	RH10	15	0	24
RV_DAL01	RH10	16	0	19

Project Name	Position	Measurement	Angle	Rebound number (R_n)
RV_DAL01	RH11	1	0	27
RV_DAL01	RH11	2	0	25
RV_DAL01	RH11	3	0	23
RV_DAL01	RH11	4	0	26
RV_DAL01	RH11	5	0	25
RV_DAL01	RH11	6	0	26
RV_DAL01	RH11	7	0	24
RV_DAL01	RH11	8	0	29
RV_DAL01	RH11	9	0	23
RV_DAL01	RH11	10	0	26
RV_DAL01	RH11	11	0	24
RV_DAL01	RH11	12	0	24
RV_DAL01	RH11	13	0	23
RV_DAL01	RH11	14	0	25
RV_DAL01	RH11	15	0	24
RV_DAL01	RH11	16	0	23
RV_DAL01	RH12	1	0	20
RV_DAL01	RH12	2	0	20
RV_DAL01	RH12	3	0	20
RV_DAL01	RH12	4	0	22
RV_DAL01	RH12	5	0	19
RV_DAL01	RH12	6	0	21
RV_DAL01	RH12	7	0	19
RV_DAL01	RH12	8	0	20
RV_DAL01	RH12	9	0	20
RV_DAL01	RH12	10	0	20
RV_DAL01	RH12	11	0	20
RV_DAL01	RH12	12	0	20
RV_DAL01	RH12	13	0	19
RV_DAL01	RH12	14	0	19
RV_DAL01	RH12	15	0	20
RV_DAL01	RH12	16	0	20
RV_DAL01	RH13	1	0	14
RV_DAL01	RH13	2	0	18
RV_DAL01	RH13	3	0	18
RV_DAL01	RH13	4	0	23
RV_DAL01	RH13	5	0	18
RV_DAL01	RH13	6	0	21
RV_DAL01	RH13	7	0	20
RV_DAL01	RH13	8	0	20
RV_DAL01	RH13	9	0	18
RV_DAL01	RH13	10	0	22

Project Name	Position	Measurement	Angle	Rebound number (R_n)
RV_DAL01	RH13	11	0	20
RV_DAL01	RH13	12	0	21
RV_DAL01	RH13	13	0	19
RV_DAL01	RH13	14	0	20
RV_DAL01	RH13	15	0	20
RV_DAL01	RH13	16	0	19
RV_DAL01	RH14	1	0	20
RV_DAL01	RH14	2	0	21
RV_DAL01	RH14	3	0	23
RV_DAL01	RH14	4	0	23
RV_DAL01	RH14	5	0	21
RV_DAL01	RH14	6	0	20
RV_DAL01	RH14	7	0	20
RV_DAL01	RH14	8	0	22
RV_DAL01	RH14	9	0	22
RV_DAL01	RH14	10	0	21
RV_DAL01	RH14	11	0	20
RV_DAL01	RH14	12	0	21
RV_DAL01	RH14	13	0	21
RV_DAL01	RH14	14	0	21
RV_DAL01	RH14	15	0	21
RV_DAL01	RH14	16	0	23
RV_DAL01	RH15	1	0	28
RV_DAL01	RH15	2	0	26
RV_DAL01	RH15	3	0	26
RV_DAL01	RH15	4	0	33
RV_DAL01	RH15	5	0	26
RV_DAL01	RH15	6	0	22
RV_DAL01	RH15	7	0	23
RV_DAL01	RH15	8	0	31
RV_DAL01	RH15	9	0	28
RV_DAL01	RH15	10	0	21
RV_DAL01	RH15	11	0	25
RV_DAL01	RH15	12	0	31
RV_DAL01	RH15	13	0	23
RV_DAL01	RH15	14	0	19
RV_DAL01	RH15	15	0	27
RV_DAL01	RH15	16	0	30
RV_DAL01	RH16	1	0	18
RV_DAL01	RH16	2	0	20
RV_DAL01	RH16	3	0	20

Project Name	Position	Measurement	Angle	Rebound number (R_n)
RV_DAL01	RH16	4	0	20
RV_DAL01	RH16	5	0	19
RV_DAL01	RH16	6	0	19
RV_DAL01	RH16	7	0	20
RV_DAL01	RH16	8	0	19
RV_DAL01	RH16	9	0	18
RV_DAL01	RH16	10	0	19
RV_DAL01	RH16	11	0	19
RV_DAL01	RH16	12	0	20
RV_DAL01	RH16	13	0	18
RV_DAL01	RH16	14	0	19
RV_DAL01	RH16	15	0	20
RV_DAL01	RH16	16	0	19
RV_DAL01	RH17	1	0	21
RV_DAL01	RH17	2	0	31
RV_DAL01	RH17	3	0	32
RV_DAL01	RH17	4	0	24
RV_DAL01	RH17	5	0	28
RV_DAL01	RH17	6	0	31
RV_DAL01	RH17	7	0	26
RV_DAL01	RH17	8	0	30
RV_DAL01	RH17	9	0	29
RV_DAL01	RH17	10	0	31
RV_DAL01	RH17	11	0	30
RV_DAL01	RH17	12	0	33
RV_DAL01	RH17	13	0	26
RV_DAL01	RH17	14	0	28
RV_DAL01	RH17	15	0	30
RV_DAL01	RH17	16	0	34
RV_DAL01	RH18	1	0	23
RV_DAL01	RH18	2	0	29
RV_DAL01	RH18	3	0	32
RV_DAL01	RH18	4	0	24
RV_DAL01	RH18	5	0	31
RV_DAL01	RH18	6	0	33
RV_DAL01	RH18	7	0	35
RV_DAL01	RH18	8	0	29
RV_DAL01	RH18	9	0	31
RV_DAL01	RH18	10	0	35
RV_DAL01	RH18	11	0	31
RV_DAL01	RH18	12	0	33
RV_DAL01	RH18	13	0	27

Project Name	Position	Measurement	Angle	Rebound number (R_n)
RV_DAL01	RH18	14	0	32
RV_DAL01	RH18	15	0	23
RV_DAL01	RH18	16	0	30
RV_DAL01	RH19	1	0	20
RV_DAL01	RH19	2	0	27
RV_DAL01	RH19	3	0	23
RV_DAL01	RH19	4	0	25
RV_DAL01	RH19	5	0	24
RV_DAL01	RH19	6	0	24
RV_DAL01	RH19	7	0	20
RV_DAL01	RH19	8	0	27
RV_DAL01	RH19	9	0	22
RV_DAL01	RH19	10	0	28
RV_DAL01	RH19	11	0	31
RV_DAL01	RH19	12	0	27
RV_DAL01	RH19	13	0	25
RV_DAL01	RH19	14	0	24
RV_DAL01	RH19	15	0	31
RV_DAL01	RH19	16	0	30
RV_DAL01	RH20	1	0	35
RV_DAL01	RH20	2	0	34
RV_DAL01	RH20	3	0	35
RV_DAL01	RH20	4	0	33
RV_DAL01	RH20	5	0	32
RV_DAL01	RH20	6	0	32
RV_DAL01	RH20	7	0	34
RV_DAL01	RH20	8	0	32
RV_DAL01	RH20	9	0	33
RV_DAL01	RH20	10	0	31
RV_DAL01	RH20	11	0	29
RV_DAL01	RH20	12	0	34
RV_DAL01	RH20	13	0	29
RV_DAL01	RH20	14	0	17
RV_DAL01	RH20	15	0	34
RV_DAL01	RH20	16	0	32
RV_DAL01	RH21	1	0	27
RV_DAL01	RH21	2	0	27
RV_DAL01	RH21	3	0	30
RV_DAL01	RH21	4	0	26
RV_DAL01	RH21	5	0	25
RV_DAL01	RH21	6	0	24

Project Name	Position	Measurement	Angle	Rebound number (R_n)
RV_DAL01	RH21	7	0	27
RV_DAL01	RH21	8	0	18
RV_DAL01	RH21	9	0	27
RV_DAL01	RH21	10	0	25
RV_DAL01	RH21	11	0	31
RV_DAL01	RH21	12	0	27
RV_DAL01	RH21	13	0	26
RV_DAL01	RH21	14	0	30
RV_DAL01	RH21	15	0	26
RV_DAL01	RH21	16	0	28
RV_DAL01	RH22	1	0	32
RV_DAL01	RH22	2	0	32
RV_DAL01	RH22	3	0	32
RV_DAL01	RH22	4	0	27
RV_DAL01	RH22	5	0	28
RV_DAL01	RH22	6	0	28
RV_DAL01	RH22	7	0	25
RV_DAL01	RH22	8	0	29
RV_DAL01	RH22	9	0	21
RV_DAL01	RH22	10	0	22
RV_DAL01	RH22	11	0	26
RV_DAL01	RH22	12	0	29
RV_DAL01	RH22	13	0	24
RV_DAL01	RH22	14	0	24
RV_DAL01	RH22	15	0	24
RV_DAL01	RH22	16	0	23
RV_DAL01	RH23	1	0	34
RV_DAL01	RH23	2	0	33
RV_DAL01	RH23	3	0	32
RV_DAL01	RH23	4	0	29
RV_DAL01	RH23	5	0	32
RV_DAL01	RH23	6	0	34
RV_DAL01	RH23	7	0	35
RV_DAL01	RH23	8	0	32
RV_DAL01	RH23	9	0	29
RV_DAL01	RH23	10	0	33
RV_DAL01	RH23	11	0	35
RV_DAL01	RH23	12	0	32
RV_DAL01	RH23	13	0	34
RV_DAL01	RH23	14	0	33
RV_DAL01	RH23	15	0	35
RV_DAL01	RH23	16	0	34

Project Name	Position	Measurement	Angle	Rebound number (R_n)
RV_DAL01	RH24	1	0	28
RV_DAL01	RH24	2	0	33
RV_DAL01	RH24	3	0	31
RV_DAL01	RH24	4	0	30
RV_DAL01	RH24	5	0	24
RV_DAL01	RH24	6	0	27
RV_DAL01	RH24	7	0	30
RV_DAL01	RH24	8	0	25
RV_DAL01	RH24	9	0	32
RV_DAL01	RH24	10	0	24
RV_DAL01	RH24	11	0	19
RV_DAL01	RH24	12	0	28
RV_DAL01	RH24	13	0	30
RV_DAL01	RH24	14	0	29
RV_DAL01	RH24	15	0	29
RV_DAL01	RH24	16	0	22
RV_DAL01	RH25	1	0	26
RV_DAL01	RH25	2	0	25
RV_DAL01	RH25	3	0	25
RV_DAL01	RH25	4	0	19
RV_DAL01	RH25	5	0	24
RV_DAL01	RH25	6	0	26
RV_DAL01	RH25	7	0	27
RV_DAL01	RH25	8	0	23
RV_DAL01	RH25	9	0	25
RV_DAL01	RH25	10	0	22
RV_DAL01	RH25	11	0	26
RV_DAL01	RH25	12	0	26
RV_DAL01	RH25	13	0	22
RV_DAL01	RH25	14	0	22
RV_DAL01	RH25	15	0	24
RV_DAL01	RH25	16	0	22
RV_DAL01	RH26	1	0	21
RV_DAL01	RH26	2	0	24
RV_DAL01	RH26	3	0	21
RV_DAL01	RH26	4	0	22
RV_DAL01	RH26	5	0	26
RV_DAL01	RH26	6	0	28
RV_DAL01	RH26	7	0	24
RV_DAL01	RH26	8	0	21
RV_DAL01	RH26	9	0	25
RV_DAL01	RH26	10	0	23

Project Name	Position	Measurement	Angle	Rebound number (R_n)
RV_DAL01	RH26	11	0	20
RV_DAL01	RH26	12	0	24
RV_DAL01	RH26	13	0	23
RV_DAL01	RH26	14	0	23
RV_DAL01	RH26	15	0	24
RV_DAL01	RH26	16	0	23
RV_DAL01	RH27	1	0	25
RV_DAL01	RH27	2	0	21
RV_DAL01	RH27	3	0	26
RV_DAL01	RH27	4	0	22
RV_DAL01	RH27	5	0	24
RV_DAL01	RH27	6	0	24
RV_DAL01	RH27	7	0	22
RV_DAL01	RH27	8	0	23
RV_DAL01	RH27	9	0	22
RV_DAL01	RH27	10	0	20
RV_DAL01	RH27	11	0	22
RV_DAL01	RH27	12	0	22
RV_DAL01	RH27	13	0	22
RV_DAL01	RH27	14	0	21
RV_DAL01	RH27	15	0	22
RV_DAL01	RH27	16	0	23
RV_DAL01	RH28	1	0	20
RV_DAL01	RH28	2	0	25
RV_DAL01	RH28	3	0	22
RV_DAL01	RH28	4	0	24
RV_DAL01	RH28	5	0	19
RV_DAL01	RH28	6	0	20
RV_DAL01	RH28	7	0	22
RV_DAL01	RH28	8	0	21
RV_DAL01	RH28	9	0	19
RV_DAL01	RH28	10	0	21
RV_DAL01	RH28	11	0	20
RV_DAL01	RH28	12	0	19
RV_DAL01	RH28	13	0	17
RV_DAL01	RH28	14	0	22
RV_DAL01	RH28	15	0	19
RV_DAL01	RH28	16	0	20
RV_DAL01	RH29	1	0	18
RV_DAL01	RH29	2	0	20
RV_DAL01	RH29	3	0	25

Project Name	Position	Measurement	Angle	Rebound number (R_n)
RV_DAL01	RH29	4	0	24
RV_DAL01	RH29	5	0	20
RV_DAL01	RH29	6	0	24
RV_DAL01	RH29	7	0	24
RV_DAL01	RH29	8	0	22
RV_DAL01	RH29	9	0	21
RV_DAL01	RH29	10	0	24
RV_DAL01	RH29	11	0	27
RV_DAL01	RH29	12	0	21
RV_DAL01	RH29	13	0	21
RV_DAL01	RH29	14	0	23
RV_DAL01	RH29	15	0	21
RV_DAL01	RH29	16	0	25
RV_DAL01	RH30	1	0	21
RV_DAL01	RH30	2	0	19
RV_DAL01	RH30	3	0	19
RV_DAL01	RH30	4	0	26
RV_DAL01	RH30	5	0	24
RV_DAL01	RH30	6	0	24
RV_DAL01	RH30	7	0	23
RV_DAL01	RH30	8	0	21
RV_DAL01	RH30	9	0	21
RV_DAL01	RH30	10	0	27
RV_DAL01	RH30	11	0	22
RV_DAL01	RH30	12	0	26
RV_DAL01	RH30	13	0	20
RV_DAL01	RH30	14	0	24
RV_DAL01	RH30	15	0	21
RV_DAL01	RH30	16	0	30
RV_DAL01	RH31	1	0	24
RV_DAL01	RH31	2	0	17
RV_DAL01	RH31	3	0	23
RV_DAL01	RH31	4	0	20
RV_DAL01	RH31	5	0	20
RV_DAL01	RH31	6	0	21
RV_DAL01	RH31	7	0	19
RV_DAL01	RH31	8	0	21
RV_DAL01	RH31	9	0	19
RV_DAL01	RH31	10	0	26
RV_DAL01	RH31	11	0	27
RV_DAL01	RH31	12	0	28
RV_DAL01	RH31	13	0	19

Project Name	Position	Measurement	Angle	Rebound number (R_n)
RV_DAL01	RH31	14	0	24
RV_DAL01	RH31	15	0	25
RV_DAL01	RH31	16	0	25
RV_DAL01	RH32	1	0	19
RV_DAL01	RH32	2	0	21
RV_DAL01	RH32	3	0	19
RV_DAL01	RH32	4	0	14
RV_DAL01	RH32	5	0	19
RV_DAL01	RH32	6	0	18
RV_DAL01	RH32	7	0	17
RV_DAL01	RH32	8	0	19
RV_DAL01	RH32	9	0	19
RV_DAL01	RH32	10	0	18
RV_DAL01	RH32	11	0	19
RV_DAL01	RH32	12	0	20
RV_DAL01	RH32	13	0	20
RV_DAL01	RH32	14	0	19
RV_DAL01	RH32	15	0	18
RV_DAL01	RH32	16	0	21
RV_DAL01	RH33	1	0	20
RV_DAL01	RH33	2	0	19
RV_DAL01	RH33	3	0	27
RV_DAL01	RH33	4	0	25
RV_DAL01	RH33	5	0	20
RV_DAL01	RH33	6	0	19
RV_DAL01	RH33	7	0	22
RV_DAL01	RH33	8	0	20
RV_DAL01	RH33	9	0	20
RV_DAL01	RH33	10	0	25
RV_DAL01	RH33	11	0	18
RV_DAL01	RH33	12	0	24
RV_DAL01	RH33	13	0	20
RV_DAL01	RH33	14	0	20
RV_DAL01	RH33	15	0	25
RV_DAL01	RH33	16	0	23
RV_DAL01	RH34	1	0	29
RV_DAL01	RH34	2	0	22
RV_DAL01	RH34	3	0	21
RV_DAL01	RH34	4	0	21
RV_DAL01	RH34	5	0	25
RV_DAL01	RH34	6	0	19

Project Name	Position	Measurement	Angle	Rebound number (R_n)
RV_DAL01	RH34	7	0	21
RV_DAL01	RH34	8	0	20
RV_DAL01	RH34	9	0	18
RV_DAL01	RH34	10	0	19
RV_DAL01	RH34	11	0	18
RV_DAL01	RH34	12	0	20
RV_DAL01	RH34	13	0	20
RV_DAL01	RH34	14	0	19
RV_DAL01	RH34	15	0	20
RV_DAL01	RH34	16	0	21
RV_DAL01	RH35	1	0	21
RV_DAL01	RH35	2	0	24
RV_DAL01	RH35	3	0	20
RV_DAL01	RH35	4	0	20
RV_DAL01	RH35	5	0	19
RV_DAL01	RH35	6	0	26
RV_DAL01	RH35	7	0	20
RV_DAL01	RH35	8	0	20
RV_DAL01	RH35	9	0	20
RV_DAL01	RH35	10	0	19
RV_DAL01	RH35	11	0	20
RV_DAL01	RH35	12	0	26
RV_DAL01	RH35	13	0	25
RV_DAL01	RH35	14	0	23
RV_DAL01	RH35	15	0	26
RV_DAL01	RH35	16	0	20
RV_DAL01	RH36	1	0	22
RV_DAL01	RH36	2	0	20
RV_DAL01	RH36	3	0	20
RV_DAL01	RH36	4	0	20
RV_DAL01	RH36	5	0	18
RV_DAL01	RH36	6	0	20
RV_DAL01	RH36	7	0	19
RV_DAL01	RH36	8	0	20
RV_DAL01	RH36	9	0	19
RV_DAL01	RH36	10	0	19
RV_DAL01	RH36	11	0	20
RV_DAL01	RH36	12	0	19
RV_DAL01	RH36	13	0	19
RV_DAL01	RH36	14	0	20
RV_DAL01	RH36	15	0	20
RV_DAL01	RH36	16	0	17

Project Name	Position	Measurement	Angle	Rebound number (R_n)
RV_DAL01	RH37	1	0	29
RV_DAL01	RH37	2	0	27
RV_DAL01	RH37	3	0	30
RV_DAL01	RH37	4	0	22
RV_DAL01	RH37	5	0	23
RV_DAL01	RH37	6	0	19
RV_DAL01	RH37	7	0	27
RV_DAL01	RH37	8	0	25
RV_DAL01	RH37	9	0	22
RV_DAL01	RH37	10	0	29
RV_DAL01	RH37	11	0	23
RV_DAL01	RH37	12	0	20
RV_DAL01	RH37	13	0	24
RV_DAL01	RH37	14	0	22
RV_DAL01	RH37	15	0	23
RV_DAL01	RH37	16	0	21
RV_DAL01	RH38	1	0	26
RV_DAL01	RH38	2	0	21
RV_DAL01	RH38	3	0	22
RV_DAL01	RH38	4	0	28
RV_DAL01	RH38	5	0	25
RV_DAL01	RH38	6	0	20
RV_DAL01	RH38	7	0	22
RV_DAL01	RH38	8	0	23
RV_DAL01	RH38	9	0	24
RV_DAL01	RH38	10	0	21
RV_DAL01	RH38	11	0	21
RV_DAL01	RH38	12	0	23
RV_DAL01	RH38	13	0	23
RV_DAL01	RH38	14	0	22
RV_DAL01	RH38	15	0	22
RV_DAL01	RH38	16	0	23
RV_DAL01	RH39	1	0	27
RV_DAL01	RH39	2	0	21
RV_DAL01	RH39	3	0	26
RV_DAL01	RH39	4	0	20
RV_DAL01	RH39	5	0	15
RV_DAL01	RH39	6	0	29
RV_DAL01	RH39	7	0	19
RV_DAL01	RH39	8	0	26
RV_DAL01	RH39	9	0	26
RV_DAL01	RH39	10	0	28

Project Name	Position	Measurement	Angle	Rebound number (R_n)
RV_DAL01	RH39	11	0	30
RV_DAL01	RH39	12	0	25
RV_DAL01	RH39	13	0	24
RV_DAL01	RH39	14	0	28
RV_DAL01	RH39	15	0	30
RV_DAL01	RH39	16	0	27
RV_DAL01	RH40	1	0	33
RV_DAL01	RH40	2	0	31
RV_DAL01	RH40	3	0	23
RV_DAL01	RH40	4	0	31
RV_DAL01	RH40	5	0	31
RV_DAL01	RH40	6	0	31
RV_DAL01	RH40	7	0	28
RV_DAL01	RH40	8	0	28
RV_DAL01	RH40	9	0	29
RV_DAL01	RH40	10	0	19
RV_DAL01	RH40	11	0	27
RV_DAL01	RH40	12	0	27
RV_DAL01	RH40	13	0	29
RV_DAL01	RH40	14	0	30
RV_DAL01	RH40	15	0	26
RV_DAL01	RH40	16	0	29

Appendix B. Finite Element Methodology Report

Finite Element Modelling Report

Non-destructive testing and finite element modelling of historical masonry wall

1. Introduction

Finite element analysis has been proven to be a powerful tool for engineers worldwide to design and calculate structural elements in various engineering fields. Certain construction materials exhibit unique behaviour due to ageing and weathering; more sophisticated analysis methods are required to capture this behaviour. Historical structures have been exposed to natural elements for long periods, impacting the properties of the materials which cannot be captured in standard material libraries of conventional analysis computer software. Abaqus CAE's ability to develop unique material properties is a suitable option for analysing a historic masonry wall.

In this report, the modelling of the historical masonry wall is described. Firstly, the overall modelling procedure is described. The material properties that have been used for each modelling attempt are described. The model is built step by step using modelling procedures to achieve a stable and accurate final model. Each attempt is described in detail, and the verification of each model is displayed.

2. Modelling procedure

A step-by-step approach is essential for developing a finite element model using Abaqus CAE to ensure a stable analysis and conduct sufficient diagnostics when errors are encountered. This section describes the methods used to obtain a stable analysis and to reduce the degree of error in the results.

The model geometry and material properties obtained from testing are described, followed by the boundary conditions employed during modelling.

2.1. Model geometry

The historical masonry wall has been modelled as a simplified micro-model. This model assumes that the mortar interface with the masonry units has a thickness of zero and that the contact between the masonry units has restricted slip behaviour due to friction.

The overall width of the wall has been measured as 600 mm, and due to the non-destructive testing done over the wall's full thickness, it is assumed that the material properties are homogeneous over the full thickness. The model is therefore developed as a single leaf wall using the masonry bricks as parts, with the full bricks having dimensions of 220x80x600 mm (LxHxW) and the half bricks having dimensions of 110x80x600 mm. A running bond configuration is used, as shown in Figure B.1.

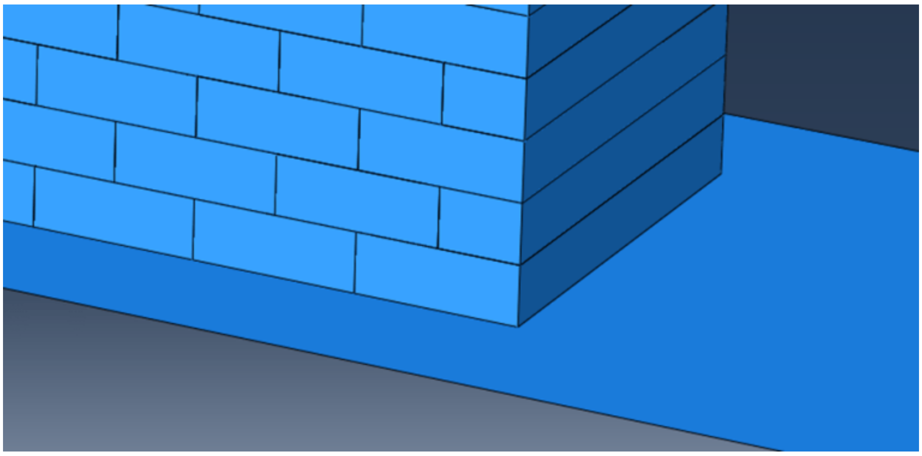

Figure B.1: Masonry brick configuration for the Abaqus model

The full masonry wall has an overall length of 20.88 m and a height of 3.98 m, excluding the gable height. The dimensions as taken on the site are shown in Figure B.2.

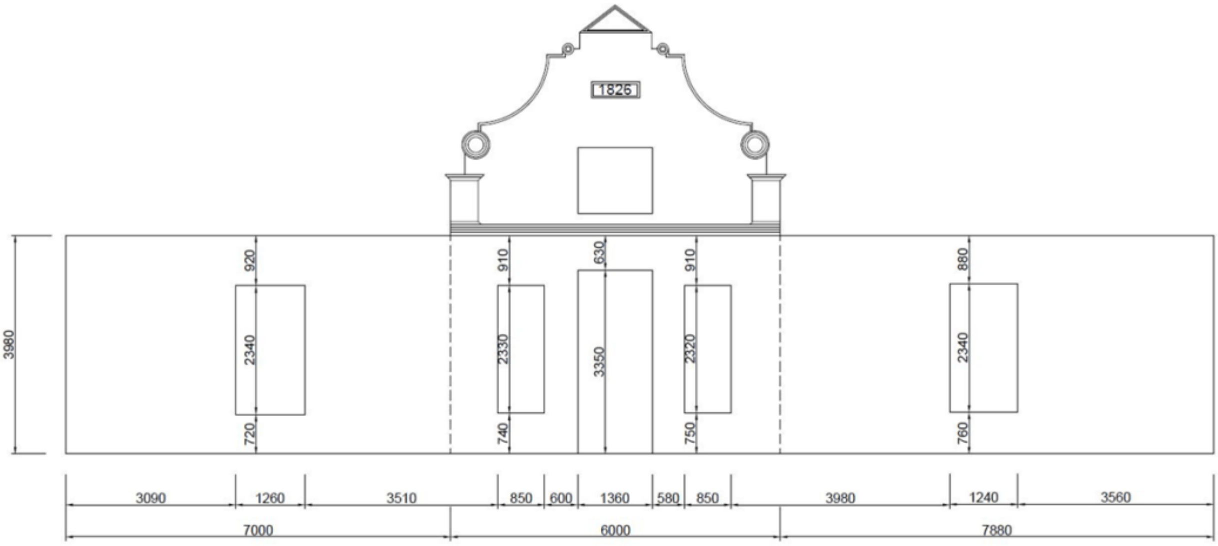

Figure B.2: Measured dimensions of the masonry wall

The model dimensions of the full masonry wall have been rounded to 20.9 m in length and 4.0 m in height.

The properties used in the overall model are discussed in the following section.

2.2. Model properties

The model is developed with the bricks having a C3D8R mesh. C3D8R elements are characterised as tetrahedron elements with eight nodes.

A discrete rigid element has been developed for the foundation plate. This foundation plate is assigned an R3D4 mesh. This element provides a constraint from the bottom and thus supports the full model. The foundation plate is assigned a reference point. This reference point is given an encastre (fully fixed against rotation and translation) boundary condition, and the foundation plate is constrained to the reference point. This restricts all translational and rotational actions on the foundation plate in the X-Y-Z planes. All brick elements are assembled on the foundation plate.

Each model is developed with increasing complexity up to the full extent of the final model. This isolates errors and incorporates remedial action before increasing the model size.

The material properties have been defined with elastic properties and with a density assigned. The elastic properties, namely Young’s modulus and Poisson’s ratio, vary throughout the structure, while the density is constant for all elements at 1445 kg/m³. The elastic properties, determined through ultrasonic pulse velocity testing, have been conducted in a grid formation over the face of the wall. The test positions are shown in Figure B.3, and the tested material properties are shown in Table B.1.

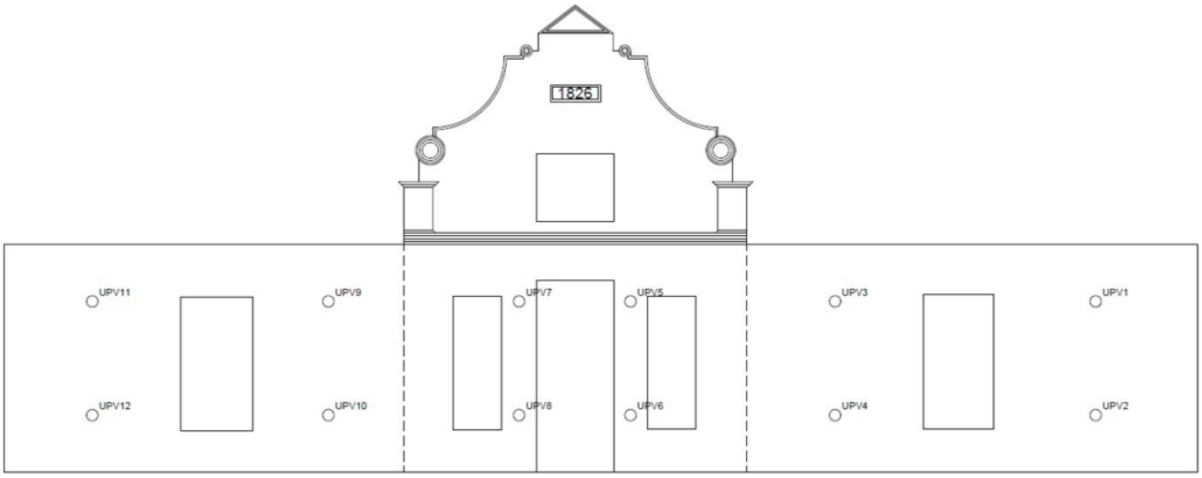

Figure B.3: Positions where UPV tests were conducted on the wall

Table B.1: Elastic material properties for the entire wall

Test position	Poisson's ratio	Young's modulus (MPa)
UPV1	0.248	4399
UPV2	0.247	5788
UPV3	0.248	6844
UPV4	0.246	6804
UPV5	0.247	11377
UPV6	0.216	8667
UPV7	0.247	8728
UPV8	0.246	12180
UPV9	0.243	8535
UPV10	0.229	6705
UPV11	0.247	8807
UPV12	0.249	10423

The material properties have been assigned to the model in zones corresponding to each test position. Each test zone corresponds with one UPV test result, and a quarter of the single wall panel is attributed to the obtained properties.

Interaction between the masonry elements has been specified as a general contact. Abaqus CAE automatically selects the corresponding element faces chosen to be in contact. This is also known as surface-to-surface contact; however, the general contact function uses less initialisation time but can be less accurate in some instances. The contact properties are specified with normal behaviour, where the default settings are selected and tangential behaviour is specified. The tangential contact properties are shown in the screenshot from Abaqus in Figure B.4.

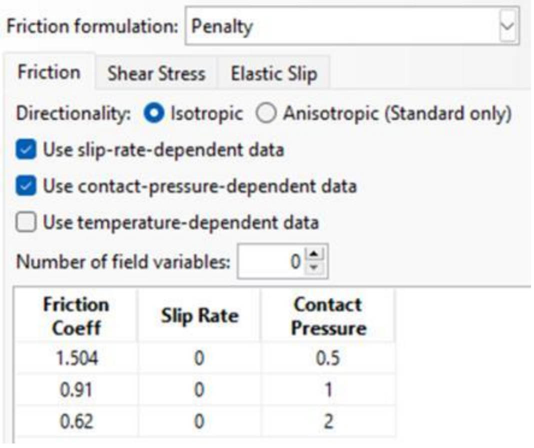

Friction formulation: Penalty

Directionality: ● Isotropic ○ Anisotropic (Standard only)

☑ Use slip-rate-dependent data

☑ Use contact-pressure-dependent data

☐ Use temperature-dependent data

Number of field variables: 0

Friction Coeff	Slip Rate	Contact Pressure
1.504	0	0.5
0.91	0	1
0.62	0	2

Figure B.4: Screenshot from Abaqus showing the tangential contact behaviour properties used in the wall model

As previously mentioned, each model is developed with increasing complexity. The initial model is developed as a smaller wall with no internal openings, and only one material property set assigned to all elements. Further, the wall is increased in height with a new material property set assigned to the additional masonry elements. The model is increased in size to develop a single panel of the full model, with the window opening. The final model is developed following the successful analysis of the previous models.

2.3. Boundary conditions and loads

Boundary conditions are introduced in the model to apply constraints and to simulate the accurate behaviour of the model when exposed to various loads. These boundary conditions are described for each model.

The model is analysed under loads to induce stresses within the masonry elements, thereby simulating real-life behaviour. All the models are subjected to a gravity loading of 9.81 m/s. The final model introduces an imposed weight load to the top of the wall to account for an attic floor and roof load. This is done in the form of an incompressible solid element that is assembled on the top of the wall with a self-weight equivalent to the calculated load.

Further, the wall is also restrained and loaded to simulate a fully reconstructed scenario, introducing a roof loading on the gable. For each scenario, a separate simulation for wind loading is introduced. The wind load is applied in the form of a pressure load, and the value of the pressure value is calculated as per SANS 10160-3: Wind Actions to be 0.94 kN/m^2.

3. Modelling procedure

The finite element models have been developed using Abaqus CAE by utilising a step-by-step approach, as discussed in the previous section. The first model developed is a small test model to evaluate the validity of the contact parameters and the overall material properties under gravity load. Following a successful simulation, the model size is increased by adding separate material properties. The model size is increased incrementally until the full model size has been obtained.

Following the successful simulation of the full model under gravity load, additional loads and boundary conditions are introduced to simulate certain real-life scenarios. The error margin is calculated, and the analysis is deemed successful once the analysed reaction forces are within 5% of the calculated reaction forces.

The subsequent section describes each model that has been developed and discusses the parameters used and the validation of the results.

3.1. Model 1: Single material test model

The first model has been developed as a preliminary test to validate the assumptions made for the contact properties and to evaluate the validity of the tested material properties. The validation is required due to the unorthodox material behaviour of the old masonry bricks. The model has been assembled as shown in Figure B.5.

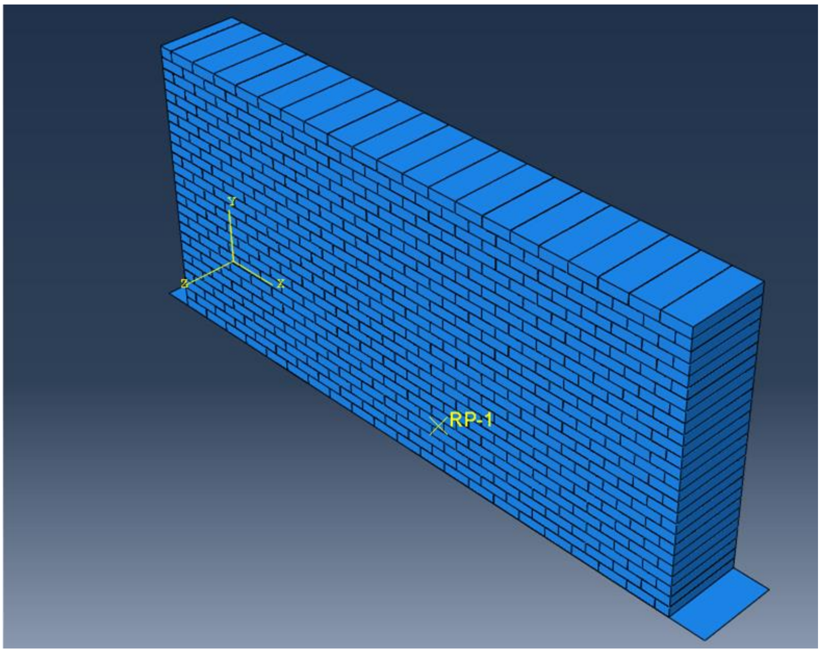

Figure B.5: Assembly of the test model using single material properties

The assembly of the model has been done on the foundation plate, a discrete rigid element. The material properties that are assigned to the masonry bricks are allocated to test zone 12 on the full model. The material properties are shown in Table B.2.

Table B.2: Elastic material properties used for Model 1

Test Zone	Density (tonne/mm^3)	Poisson’s ratio	Young’s modulus (MPa)
12	1.475 x 10^{-9}	0.249	10426

The model is subjected to a gravity loading of 9810 mm/s^2. No additional boundary conditions have been defined.

The interaction has been defined as general contact, with the domain “all with self” selected. Due to the large number of contact faces defined, automatic stabilisation is required to ensure convergence during analysis. Damping is introduced in the analysis, which applies viscous behaviour to the contact faces. Upon convergence of each time increment, the damping is slowly decreased to reduce the overall error in the results. The stabilisation parameters are shown in Figure B.6.

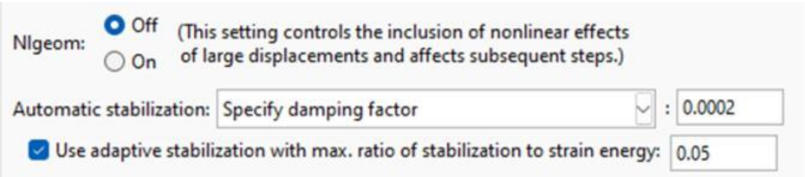

Nlgeom: ● Off ○ On (This setting controls the inclusion of nonlinear effects of large displacements and affects subsequent steps.)

Automatic stabilization: Specify damping factor : 0.0002

☑ Use adaptive stabilization with max. ratio of stabilization to strain energy: 0.05

Figure B.6: Screenshot from Abaqus showing the stabilisation parameters used for Model 1

The analysis was completed successfully following the introduction of automatic stabilisation. The obtained reaction forces are shown in Figure B.7.

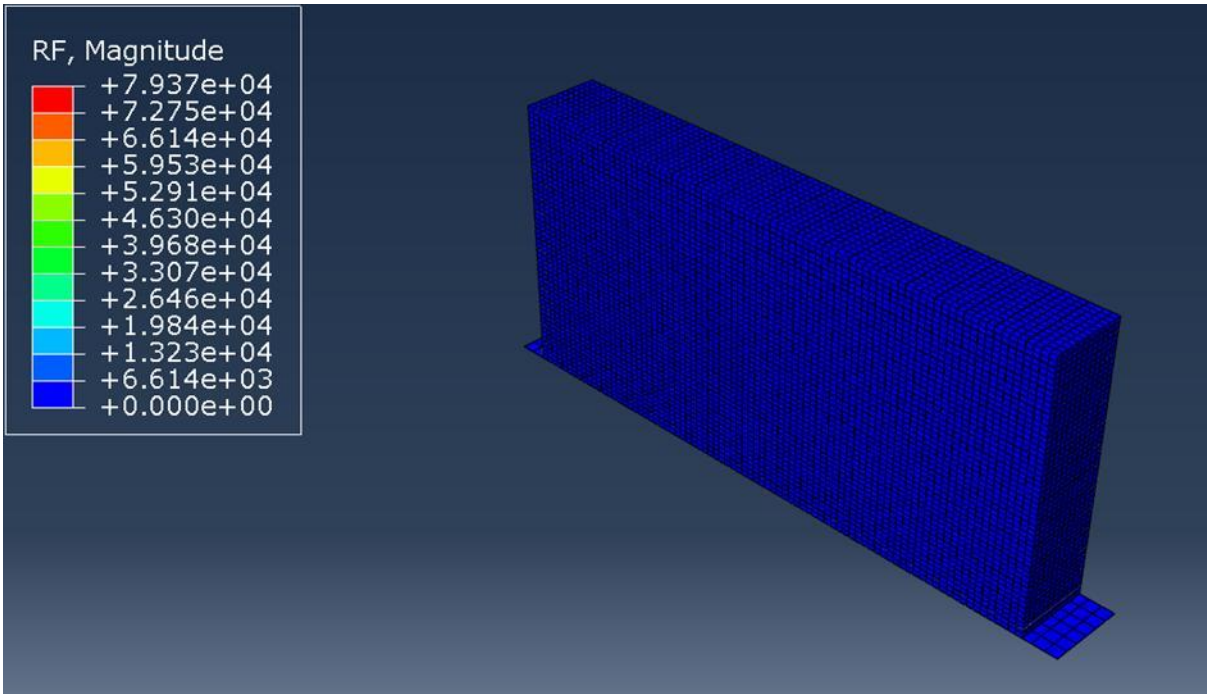

Figure B.7: Model 1: Reaction of the masonry wall along the Y-axis, in N

The reaction force produced by the analysis is Rf = 79 370 N for the self-weight of the model. The reaction force has been manually calculated through equilibrium as R = 79 786.24 N. This indicates an error of 0.52% for the analysis, which indicates a successful analysis.

3.2. Model 2: Larger test model

The second model was developed, following the first model's successful analysis, to evaluate the model's behaviour when the wall's height was increased. The test model is shown in Figure B.8.

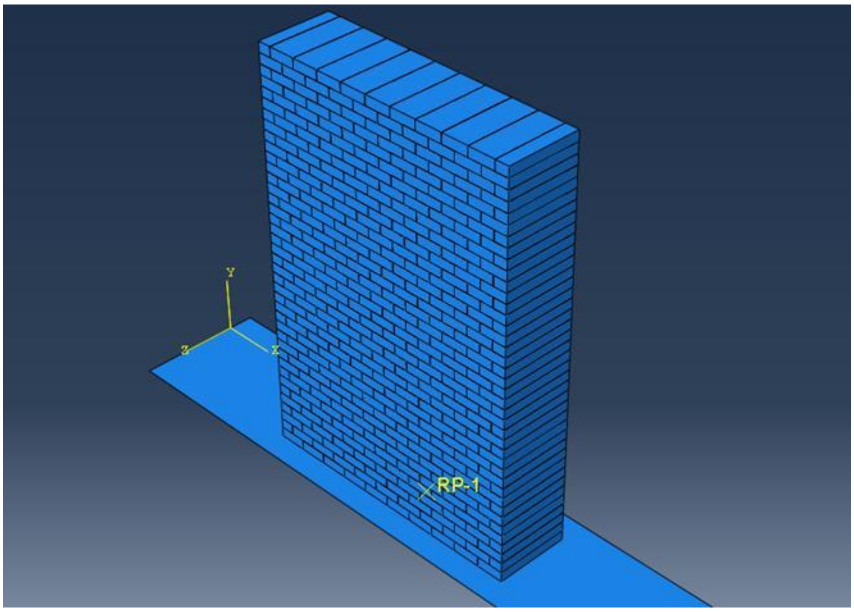

Figure B.8: Assembly of the enlarged test model using single material properties

As with the first test model, the assembly of the model has been done on the foundation plate. The material properties that are assigned to the masonry bricks are allocated for testing zone 12 on the full model. The material properties are shown in Table B.3.

Table B.3: Elastic material properties used for Model 2

Test Zone	Density (tonne/mm^3)	Poisson's ratio	Young's modulus (MPa)
12	1.475×10^{-9}	0.249	10426

The model is only subjected to a gravity loading of 9810 mm/s^2. No additional boundary conditions have been defined.

The analysis of the model failed due to non-convergence. This could be attributed to the contact faces between the masonry bricks failing to initialise, leading to slipping elements or penetration problems properly. This has been solved by replacing general contact with surface-to-surface contact. The master and slave contact faces have been selected using the "find contact pairs" function of Abaqus CAE. This proved to be more resource-intensive and time-consuming. However, the analysis could complete successfully. No stabilisation has been introduced in the simulation. The reaction forces obtained are shown in Figure B.9.

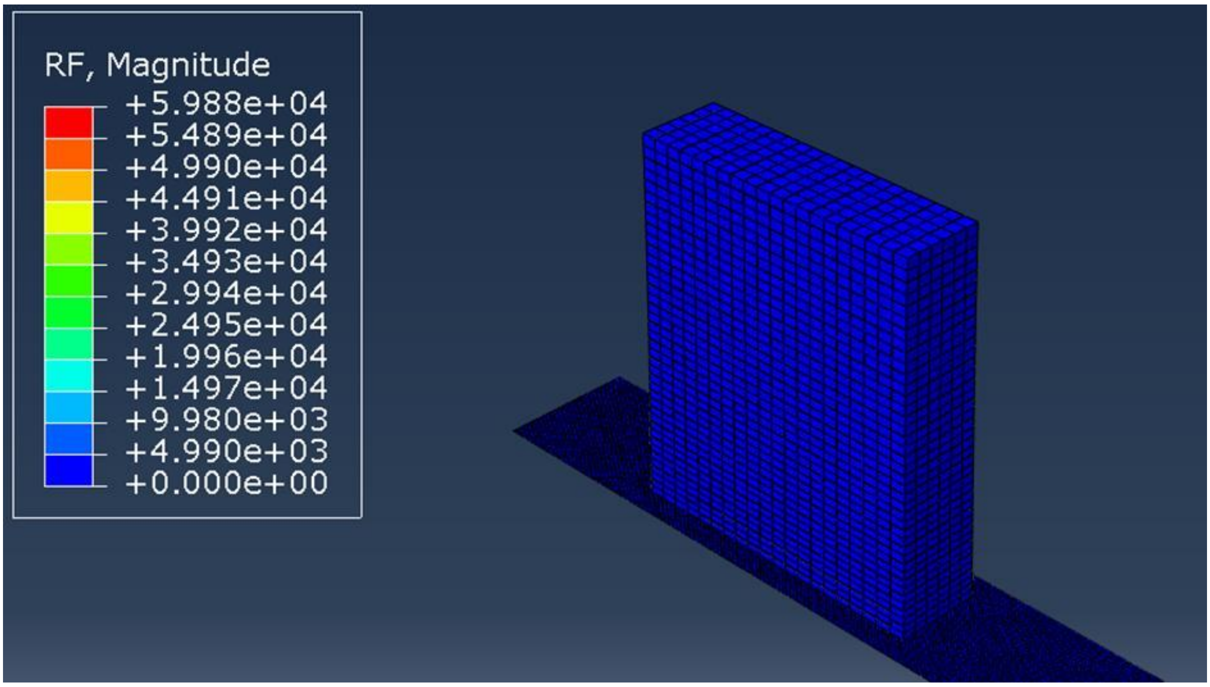

Figure B.9: Model 2: Reaction of the masonry wall along Y-axis, in N

The reaction force produced by the analysis is Rf = 59 880 N for the self-weight of the model. The reaction force has been manually calculated through equilibrium as R = 59 877.10 N. The calculated reaction force correlates perfectly with the analysed reaction force, indicating an accurate model with no error.

Following the successful analysis of the second model, a smaller portion of the old masonry wall has been analysed using surface-to-surface contact instead of general contact.

3.3. Model 3: Portion of wall panel

The following model has been developed to simulate the varying material properties defined within a portion of one of the old wall panels. The model is shown in Figure B.10.

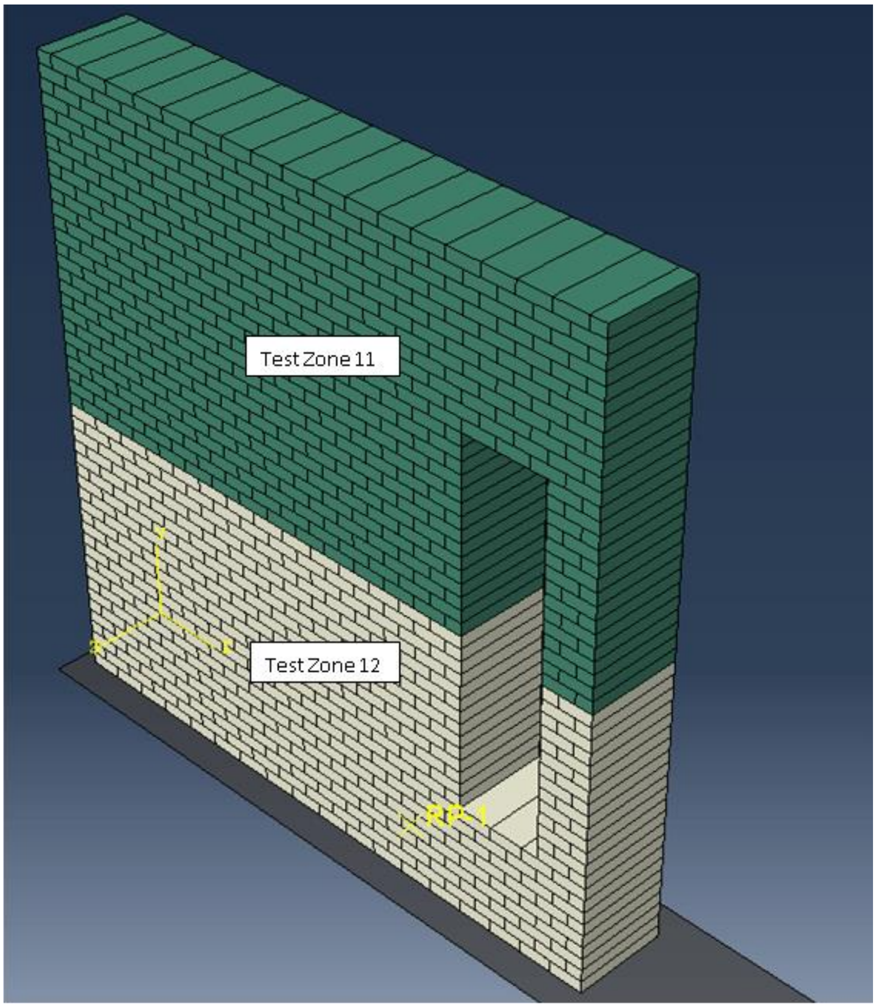

Figure B.10: Assembly of a portion of the full wall

The model has been developed to simulate the behaviour when an additional set of material properties are introduced. Figure B.10 indicates the different material properties in separate colours. The material properties are shown in Table B.4.

Table B.4: Elastic material properties used for Model 3

Test Zone	Density (tonne/mm^3)	Poisson's ratio	Young's modulus (MPa)
11	1.475×10^{-9}	0.247	8807
12	1.475×10^{-9}	0.249	10426

Due to the wall section ending in the middle of a window opening, a masonry column has been introduced to limit the abnormal behaviour at that position. The model is only subjected to gravity loading of 9810 mm/s^2. No additional boundary conditions have been defined. The interaction between the masonry bricks has been selected as surface-to-surface contact.

Due to the increased size and the overall non-linearity of the model, automatic stabilisation had to be introduced. However, the degree of stabilisation had to be kept constant to ensure convergence. This has the undesirable effect of producing a higher degree of error. The stabilisation parameters are shown in Figure B.11.

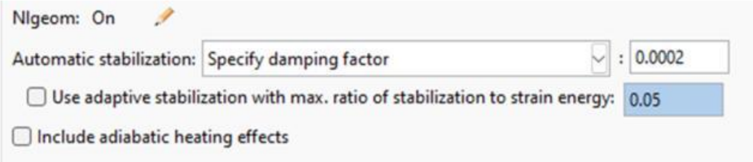

Nlgeom: On

Automatic stabilization: Specify damping factor : 0.0002

☐ Use adaptive stabilization with max. ratio of stabilization to strain energy: 0.05

☐ Include adiabatic heating effects

Figure B.11: Screenshot from Abaqus showing the stabilisation parameters used for Model 3

The results obtained through analysis are shown in Figure B.12.

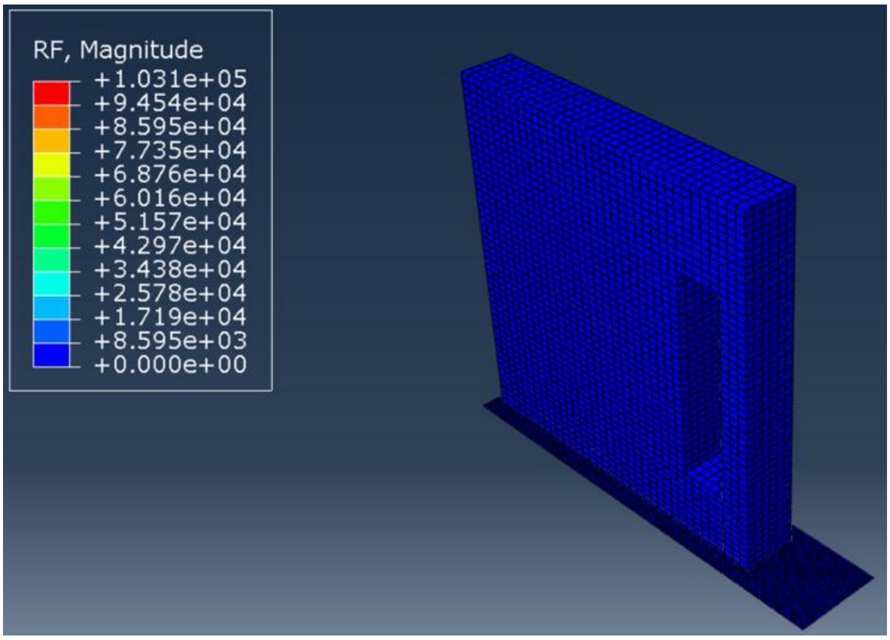

Figure B.12: Model 3: Reaction of the masonry wall along Y-axis, in N

The reaction force produced by the analysis is Rf = 103 310 N for the self-weight of the model. The reaction force has been manually calculated through equilibrium as R = 123 870.77 N. This equates to an error of 16.76%, a higher error than desirable.

Although the analysis could complete successfully, the margin of error is high. The following model was developed to evaluate the change in error when the full wall panel is modelled using the same parameters.

3.4. Model 4: Single wall panel

The wall panel was modelled to evaluate the change in the error margin with the increased model size. The model is more authentic than the actual scenario, as the column has been removed and the full window opening is modelled. The model is shown in Figure B.13.

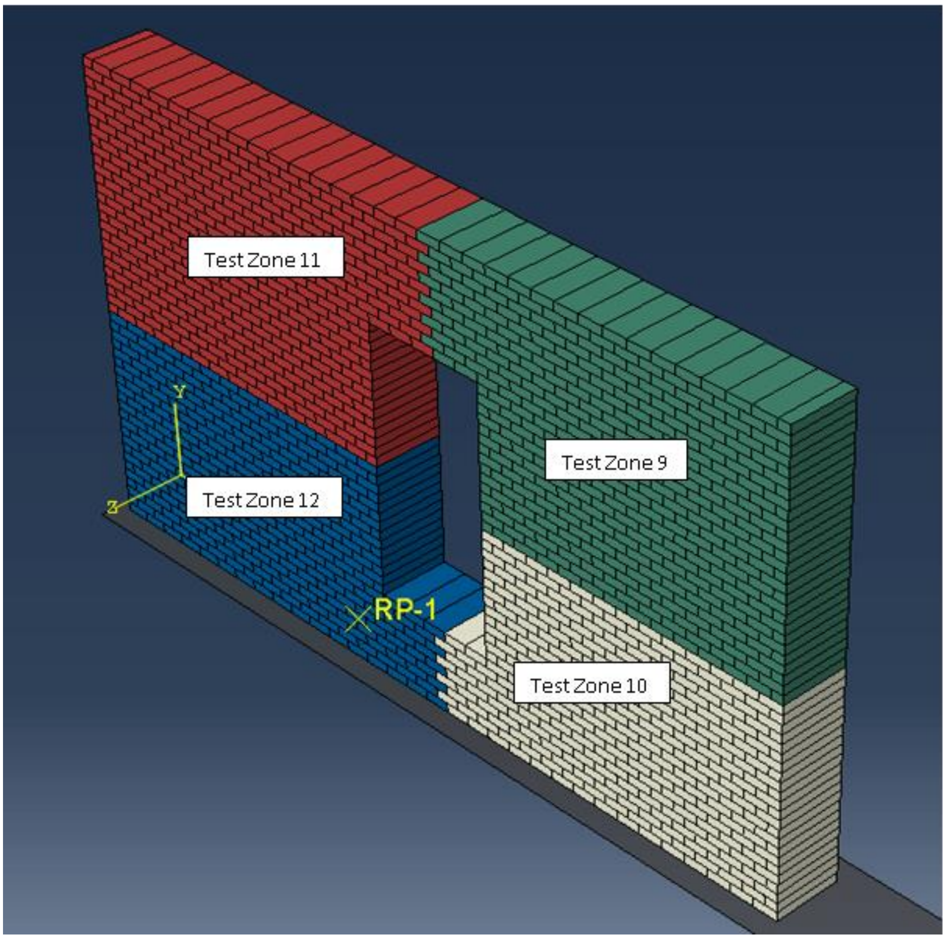

Figure B.13: Assembly of the left wall panel

The model has been developed with the material properties as tested. This is displayed in Figure B.13 in separate colours. The material properties are shown in Table B.5.

Table B.5: Elastic material properties used for Model 4

Test Zone	Density (tonne/mm^3)	Poisson's ratio	Young's modulus (MPa)
9	1.475×10^{-9}	0.243	8535
10	1.475×10^{-9}	0.229	6705
11	1.475×10^{-9}	0.247	8807
12	1.475×10^{-9}	0.249	10426

The model evaluates a third of the full model of the old masonry wall under only gravity loading. The model is only subjected to a gravity loading of 9810 mm/s^2. No additional boundary conditions have been defined. The interaction between the masonry bricks has been selected as surface-to-surface contact.

The stabilisation properties are shown in Figure B.14. The parameters have been carried over from the previous model, with the stabilisation kept constant. The degree of error is expected to be similar with the same parameters.

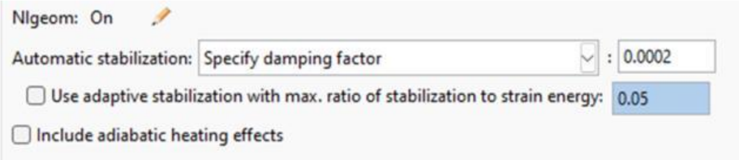

Nlgeom: On

Automatic stabilization: Specify damping factor : 0.0002

☐ Use adaptive stabilization with max. ratio of stabilization to strain energy: 0.05

☐ Include adiabatic heating effects

Figure B.14: Screenshot from Abaqus showing the stabilisation parameters used for Model 4

The analysis was completed successfully, and the results for the reaction force and the reaction forces results are shown in Figure B.15.

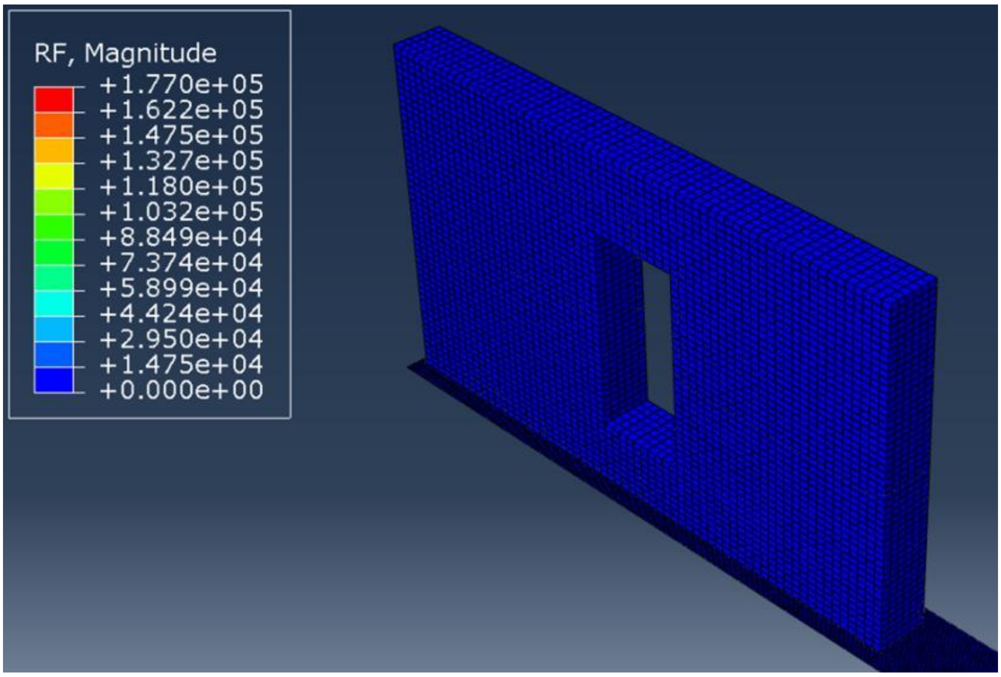

Figure B.15: Model 4: Reaction of the masonry wall along the Y-axis, in N

The reaction force produced by the analysis is Rf = 177 000 N for the self-weight of the model. The reaction force has been manually calculated through equilibrium as R = 217 802.99 N. This equates to an error of 18.73%. This degree of error remains within the range of the results obtained from Model 3, which has been expected.

The parameters used in this analysis have been carried forward to the analysis of the full masonry wall.

3.5. Model 5: Full model of old masonry wall

The current model was developed following the previous model's successful convergence, further evaluating the change in the degree of error with increased model size. All the material properties that have been tested on-site have been included in this model. The model is shown in Figure B.16.

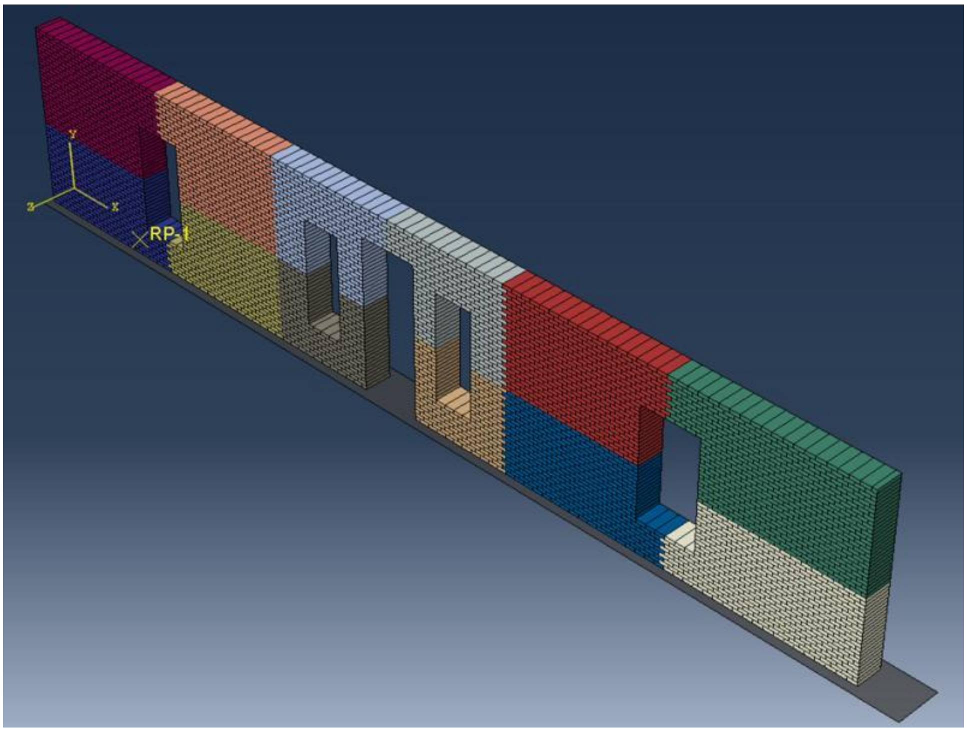

Figure B.16: Assembly of the full masonry wall, excluding the gable

All tested material properties have been included and shown in Figure B.16. The density is assigned to all elements as 1.475 x 10^{-9} tonne/mm^3. The material properties are as per Table B.6.

Table B.6: Elastic material properties used for Model 5

Test Zone	Density (tonne/mm^3)	Poisson's ratio	Young's modulus (MPa)
1	1.475 x 10^{-9}	0.248	4399
2	1.475 x 10^{-9}	0.247	5788
3	1.475 x 10^{-9}	0.248	6844
4	1.475 x 10^{-9}	0.246	6804
5	1.475 x 10^{-9}	0.247	11377
6	1.475 x 10^{-9}	0.216	8667
7	1.475 x 10^{-9}	0.247	8728
8	1.475 x 10^{-9}	0.246	12180
9	1.475 x 10^{-9}	0.243	8535
10	1.475 x 10^{-9}	0.229	6705
11	1.475 x 10^{-9}	0.247	8807
12	1.475 x 10^{-9}	0.249	10423

The model is subjected to a gravity loading of 9810 mm/s^2. No additional boundary conditions have been defined. The model describes the full extent of the old masonry wall when subjected to only gravity forces. Due to the non-convergence of the analysis, the automatic stabilisation has been increased. The parameters are shown in Figure B.17.

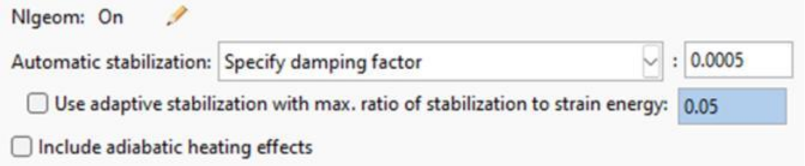

Nlgeom: On

Automatic stabilization: Specify damping factor : 0.0005

☐ Use adaptive stabilization with max. ratio of stabilization to strain energy: 0.05

☐ Include adiabatic heating effects

Figure B.17: Screenshot from Abaqus showing the stabilisation parameters used for Model 5

Surface-to-surface contact has been employed as the interaction property. The increased model size significantly increases the time and processing power required to locate all contact pairs and initialise contact.

The analysis has been completed successfully, and the reaction forces calculated are shown in Figure B.18.

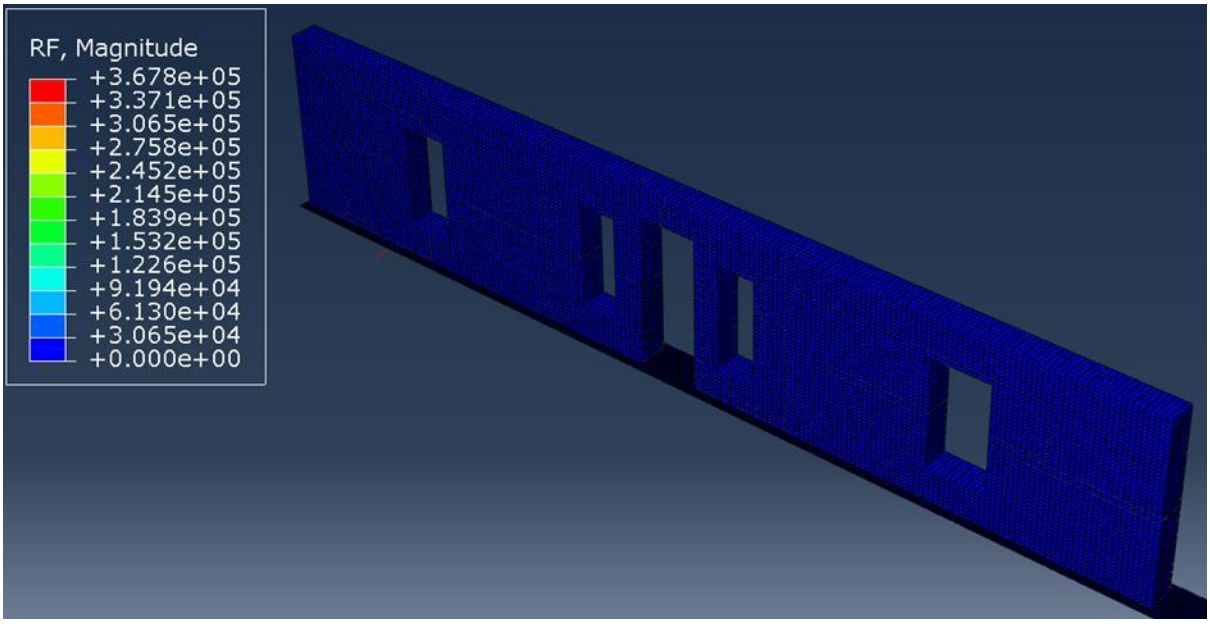

Figure B.18: Model 5: Reaction of the masonry wall along the Y-axis, in N

The reaction force produced by the analysis is Rf = 367 800 N for the self-weight of the model. The reaction force has been manually calculated through equilibrium as R = 592 558 N. It equates to an error of 37.9%. The margin of error indicates a high degree of losses encountered because of the damping that has been introduced.

The analysis has shown that the model exhibits highly non-linear behaviour which causes non-convergence; analysis can only be completed with the introduction of stabilisation. The effect of the stabilisation is unreliable results, so it is recommended that a different solver is attempted due to this non-linearity.

3.6. Model 6: Quasi-static analysis of old masonry wall

The analysis for the full model has shown that stabilisation is required to ensure convergence when running the solver. This dramatically reduces the accuracy of the results to the degree that the analysis is deemed unreliable. The solver employed is the Abaqus Standard solver, which utilises implicit static analysis.

The static implicit analysis is suitable for linear material behaviour and can analyse non-linear behaviour up to a certain limit. A quasi-static analysis is recommended if the material is highly non-linear, and the overall model displays non-linear boundary conditions. This is done using the Abaqus Explicit solver.

The Explicit solver is typically used to solve dynamic problems. However, it can be particularly useful in solving certain static problems. This is where quasi-static analysis is employed. Where dynamic problems are time-dependent, a quasi-static state is achieved when the load is applied at a low rate in a short timeframe where inertia is negligible. The model, therefore, remains in static equilibrium.

For quasi-static analysis, Model 5 has been used, as shown in Figure B.19. All material properties as tested have been assigned in the model.

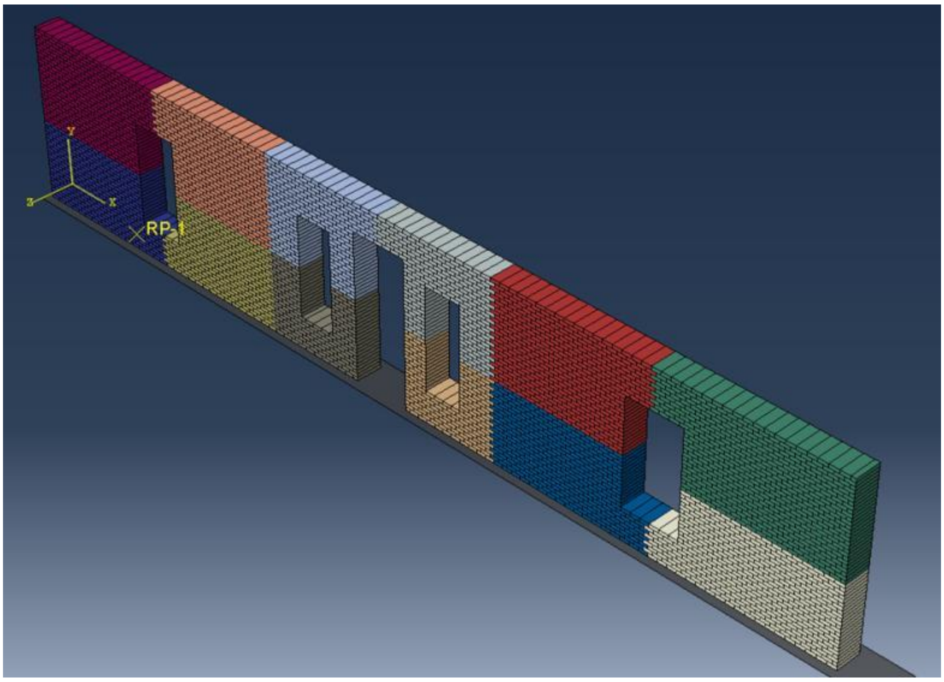

Figure B.19: Assembly of the full model used for quasi-static analysis

The material is subjected to gravity loading of 9810 m/s² only. Amplitude has been created to define the application of the load over time. The applied load is increased smoothly from 0 to the entire load at the time increment of 1. No additional boundary conditions were applied.

The interaction has been defined as general contact, with the domain “all with self” selected. No stabilisation has been used. The default step settings have been used for this modelling attempt. The reaction forces obtained through analysis are shown in Figure B.20.

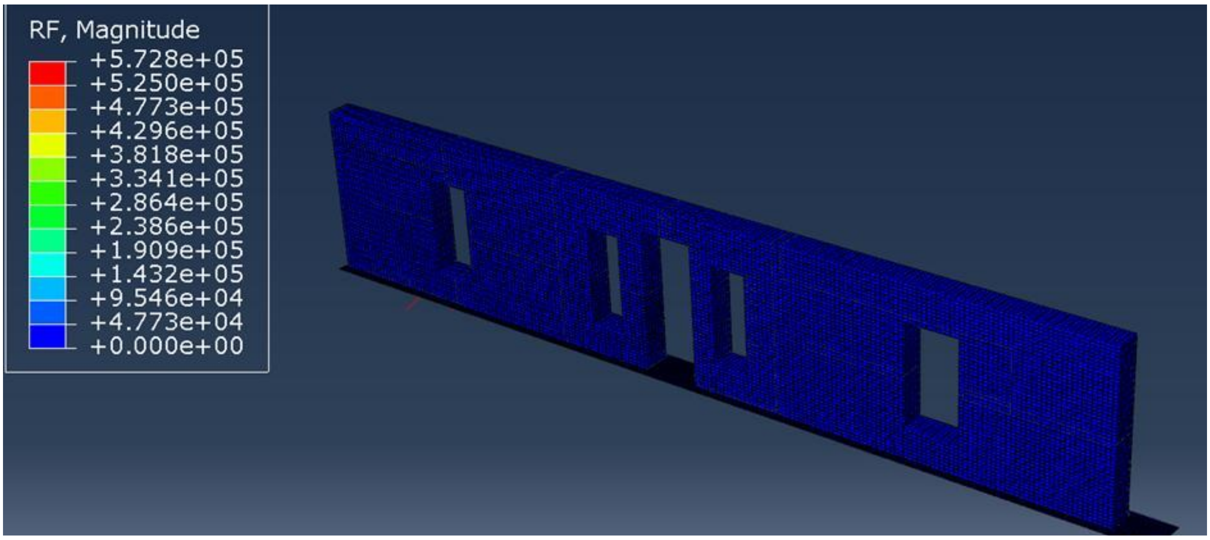

Figure B.20: Model 6: Reaction of the masonry wall along Y-axis, in N

The reaction force produced by the analysis is Rf = 573 800 N for the self-weight of the model. The reaction force has been manually calculated through equilibrium as R = 592 558 N. This equates to an error of 3.3%, which is significantly lower than the error produced by the implicit solver and within the maximum 5% tolerance.

The quasi-static analysis approach is deemed suitable for accurately solving the old masonry wall analysis and is further employed to calculate the results for the final model exposed to various loading scenarios.

4. Results and discussion

By employing a quasi-static analysis approach, the finite element model of the historical masonry wall has been successfully solved. As predicted, a degree of error is still present. However, this error is below the tolerance of 5% of the calculated reaction force, which is deemed acceptable.

The model build-up has been done using Model 6 as the basis. The gable is added to the model, and all tested material properties have been included. The gable’s material properties have been calculated as the overall average from the tested material properties.

The final model is shown in Figure B.21.

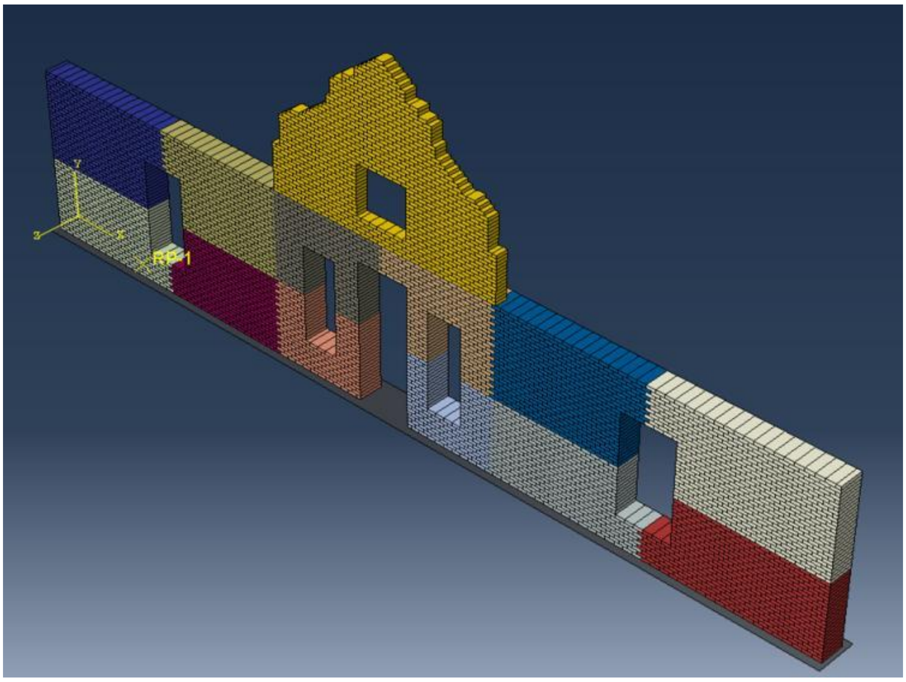

Figure B.21: Assembly of the full masonry wall including the gable

The various material properties are shown in separate colours in Figure B.21. The model has been assembled to the actual geometry measured on site. All window and door openings have been included. The width of the wall is 600 mm, as described in a previous section, and the gable width is 300 mm. The material properties assigned to the parts in the model are shown in Table B.7.

Table B.7: Elastic material properties used for the final model

Test Zone	Density (tonne/mm^3)	Poisson's ratio	Young's modulus (MPa)
1	1.475 x 10^{-9}	0.248	4399
2	1.475 x 10^{-9}	0.247	5788
3	1.475 x 10^{-9}	0.248	6844
4	1.475 x 10^{-9}	0.246	6804
5	1.475 x 10^{-9}	0.247	11377
6	1.475 x 10^{-9}	0.216	8667
7	1.475 x 10^{-9}	0.247	8728
8	1.475 x 10^{-9}	0.246	12180
9	1.475 x 10^{-9}	0.243	8535
10	1.475 x 10^{-9}	0.229	6705
11	1.475 x 10^{-9}	0.247	8807
12	1.475 x 10^{-9}	0.249	10423
Gable (Average)	1.475 x 10^{-9}	0.243	8271

The model is assembled on the foundation plate, an R3D4 element assigned a reference point. The reference point is assigned an encastre boundary condition, restricting rotation and translation. The foundation plate is constrained to the reference point, which creates a fully fixed base for the model.

Four separate simulations have been described for the model. Additional boundary conditions have been introduced to simulate the real-life behaviour of the old masonry wall according to the specific simulation. The simulated scenarios are as follows:

1. Masonry wall in current condition with no wind load
2. Masonry wall in current condition with wind load
3. Masonry wall fully reconstructed with no wind load
4. Masonry wall fully reconstructed with wind load

Each simulation is described in detail, and the results are discussed. The loadings applied and the boundary conditions are displayed in the following section.

4.1. Simulation 1: Current condition with no wind load

The first simulation has been completed on the full model subjected to gravity loading and an imposed permanent load from the attic floor on top of the wall. The wall is braced vertically by internal walls and edge walls and horizontally by the attic floor. The vertical and horizontal bracing has been modelled by restricting horizontal movement. The boundary conditions are shown in Figure B.22.

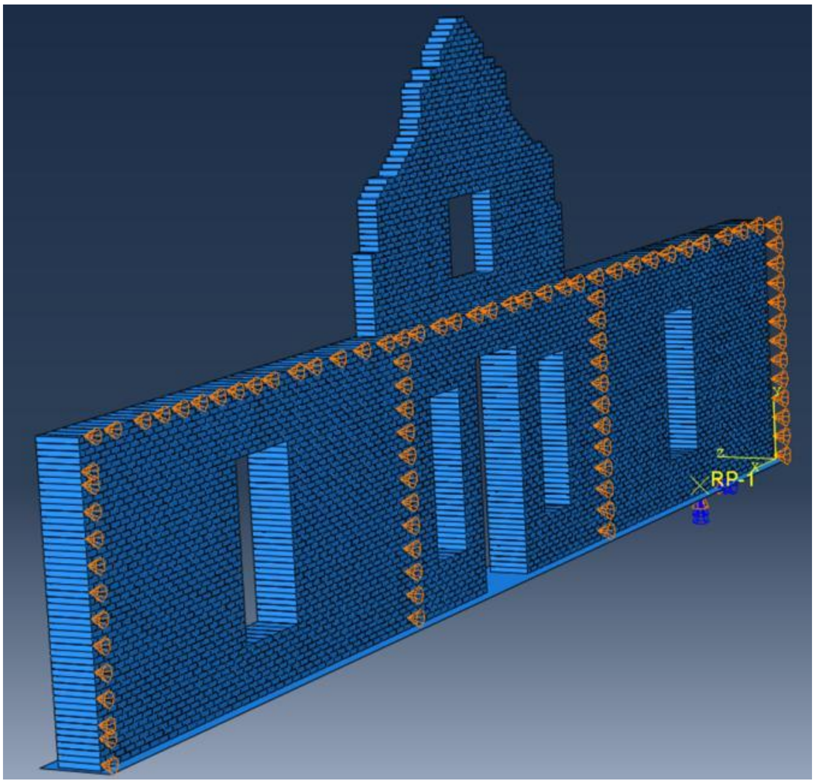

Figure B.22: Boundary conditions for the internal bracing on the wall

The attic floor's self-weight has been applied to the top of the wall in the form of a non-deformable element. The density of the element's material is equivalent to the self-weight of the floor loading, having a tributary area of 3 m.

The element imposing the self-weight of the floor is shown in Figure B.23.

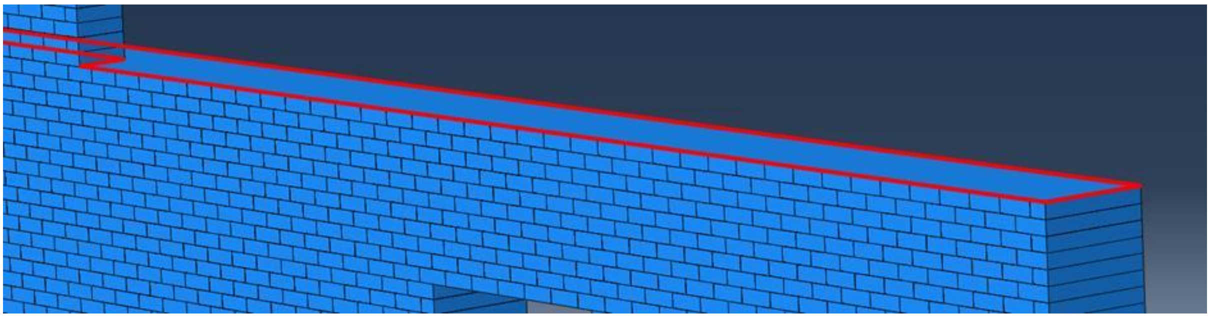

Figure B.23: Self-weight element simulating the attic floor

The full model analysis was completed successfully and results obtained. The stress distribution and displacement have been analysed, with results shown in Figures B.24 and B.25.

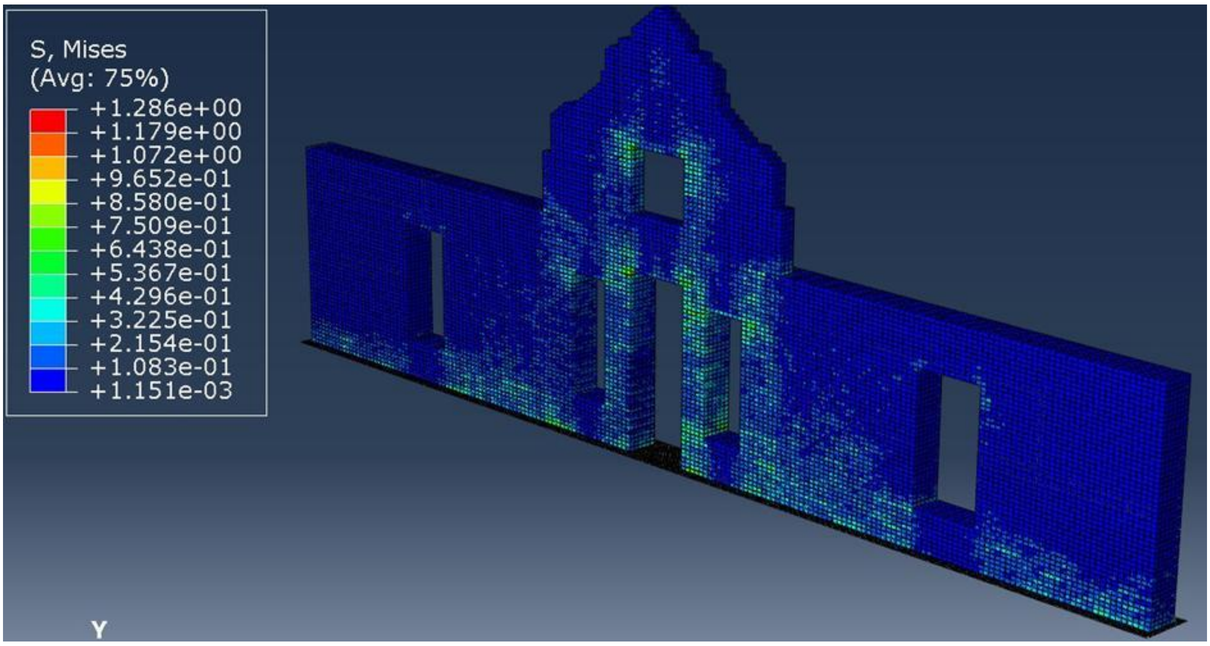

Figure B.24: Simulation 1: Distribution of Von Mises stress (MPa) on masonry wall

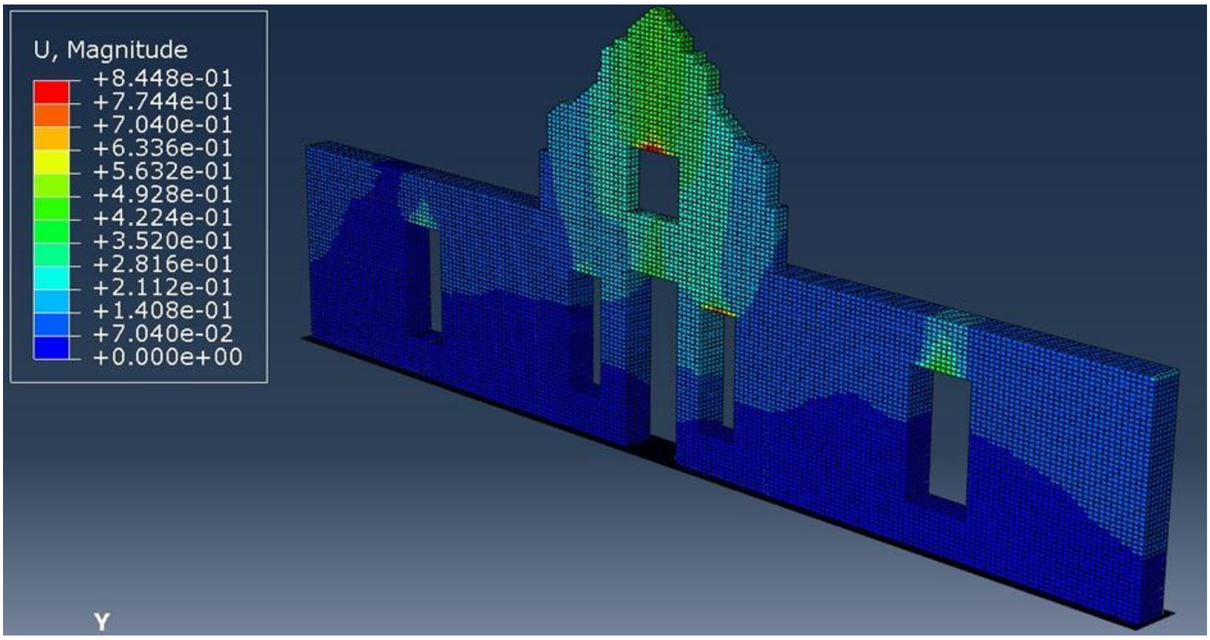

Figure B.25: Simulation 1: Displacement (mm) in the horizontal plane

The reaction force has been calculated through static equilibrium equations. The self-weight of the structure is calculated, which in turn provides the reaction force. The results obtained through analysis have been verified by comparing the reaction force in the Y-axis (direction 2) with the calculated reaction force. The reaction force obtained through analysis is shown in Figure B.26.

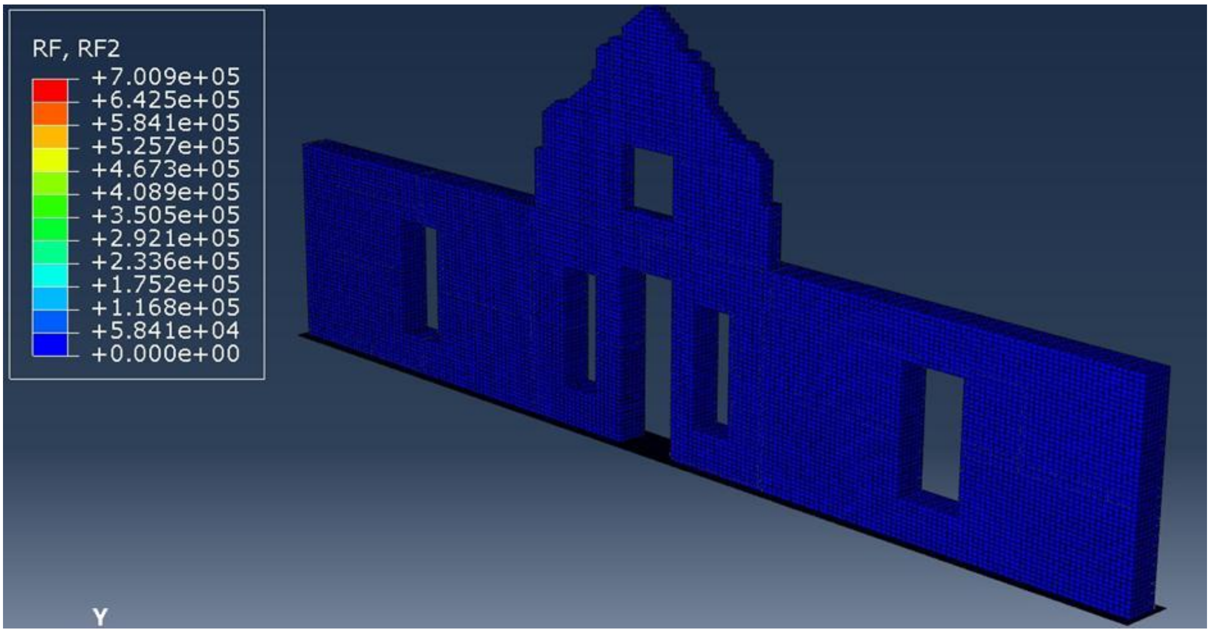

Figure B.26: Simulation 1: Reaction of the masonry wall along the Y-axis, in N

The reaction force obtained through analysis has been shown in Figure B.26 to be 700.9 kN. The reaction force has been calculated through equilibrium as 708.0 kN, which gives an error of 1%. The results are therefore assumed to be highly accurate.

It is evident that the gable experiences a higher deflection when compared to the rest of the structure, as shown in Figure B.25. This is due to the damage the overall structure has suffered which destroyed the roof structure and makes the gable wall act as unbraced at the top.

As shown in Figure B.24, the stress distribution has been calculated with the self-weight of the wall and attic floor only. Increased stresses are shown in the centre panel of the wall, which is due to the higher load distribution from the self-weight of the gable. The window opening on the gable indicates higher stresses at the top edges, with the centre wall panel indicating higher stress areas next to the door opening and at the top and bottom corners of the window openings. On the left and right panels, increased stresses are located at the bottom corners of the window openings toward the outside of the wall. These stress patterns correspond with certain crack patterns that have been identified through visual inspection.

4.2. Simulation 2: Current condition with wind load

The second simulation has been completed on a similar model as Simulation 1. The model has been adjusted by adding a wind load on the front face of the wall. This has been done by a pressure load acting on the brick surfaces. The pressure load on the front face of the wall is shown in Figure B.27. The wind load has been taken as q_k = 0.94 kPa (SANS 10160-3: Wind Actions).

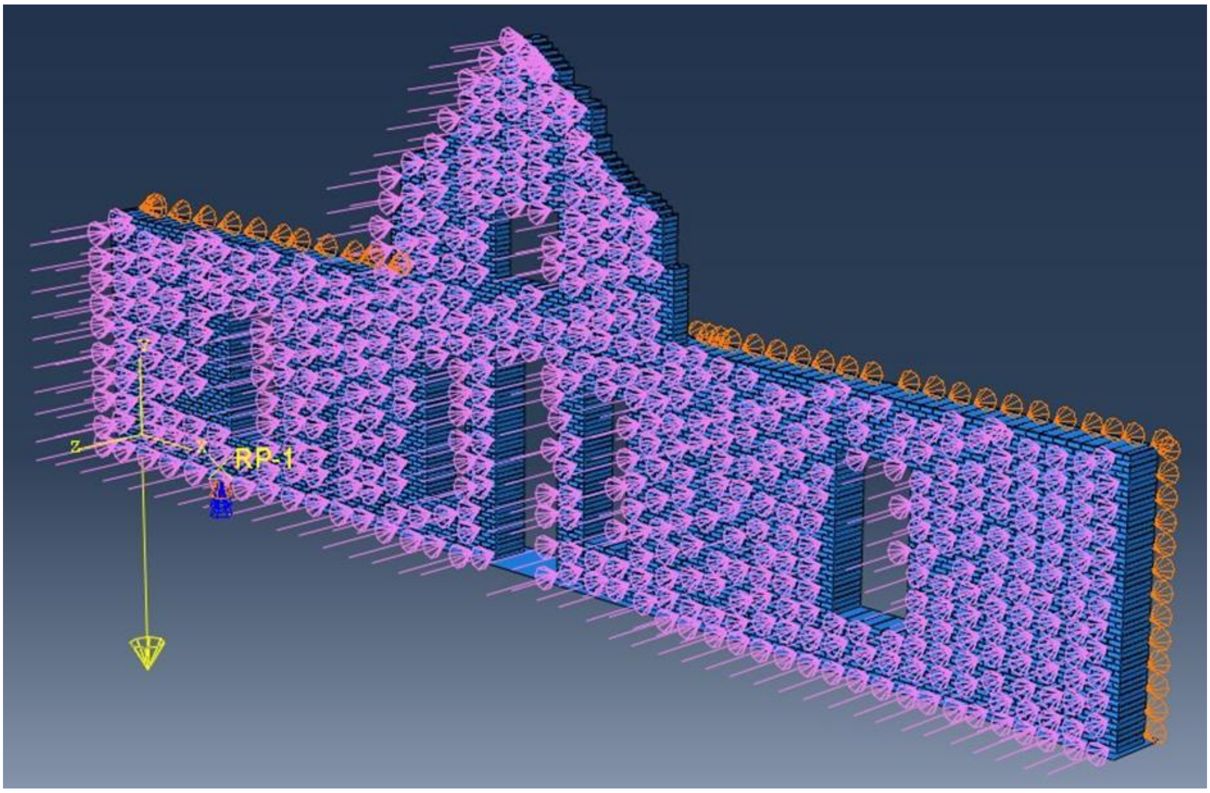

Figure B.27: Wind load imposed in the Z-axis (horizontally) on the wall

The analysis of the model with the addition of the wind load was completed successfully and results obtained. The stress distribution and displacement have been analysed, and the results are shown in Figures B.28 and B.29, respectively.

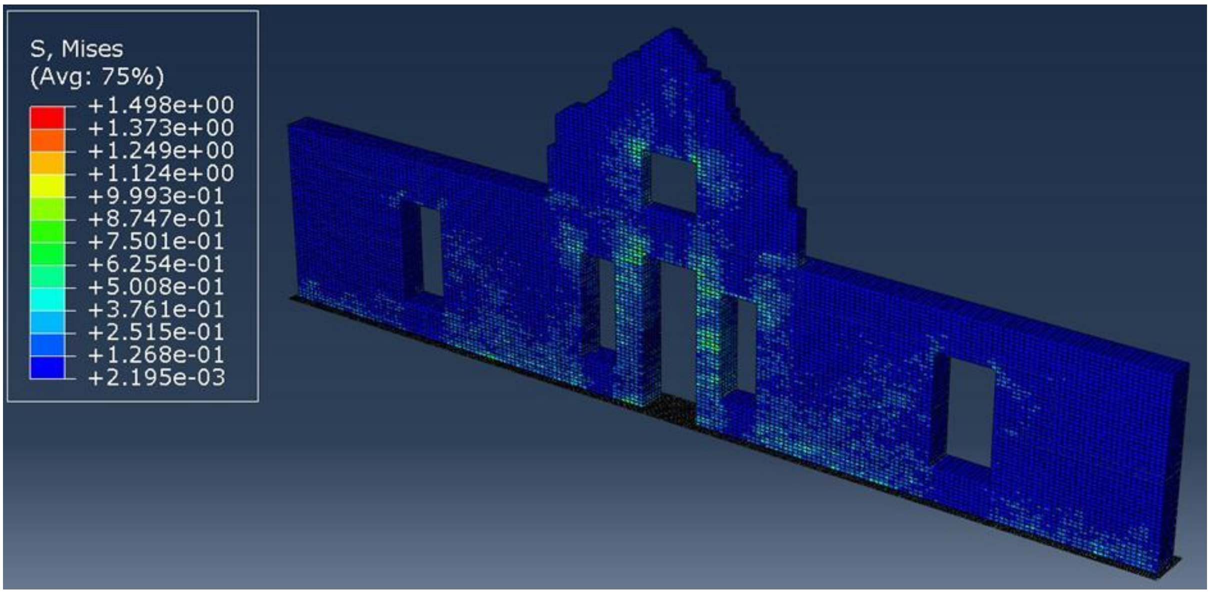

Figure B.28: Simulation 2: Distribution of Von Mises stress (MPa) on masonry wall

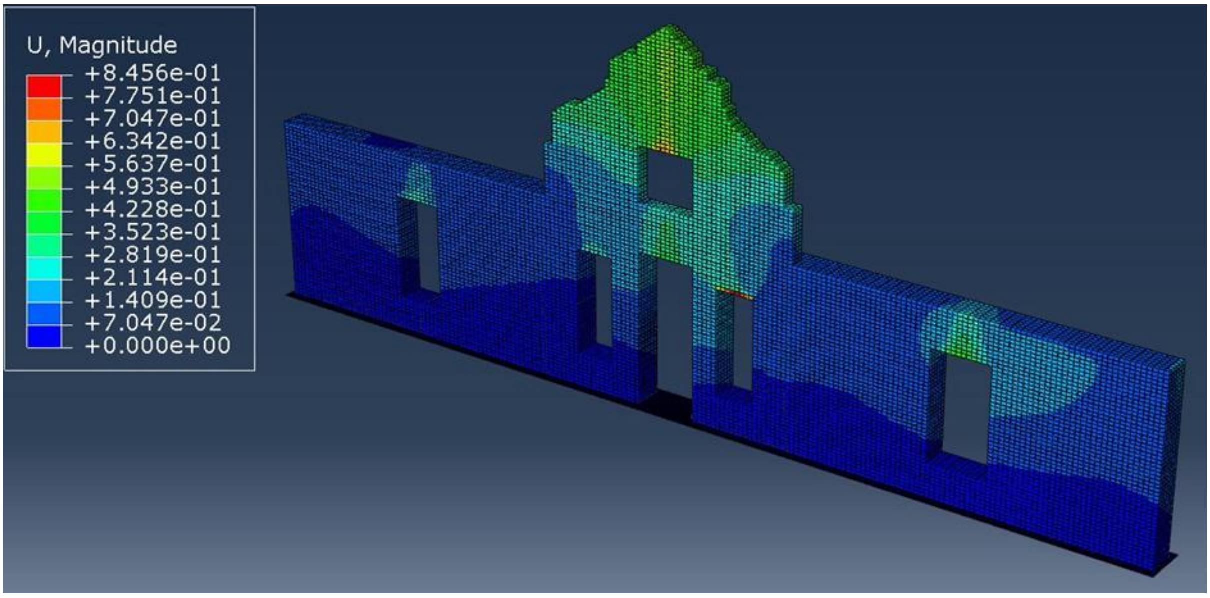

Figure B.29: Simulation 2: Displacement (mm) in horizontal plane

The results have been verified by comparing the analysed reaction force with the calculated reaction force. The reaction force obtained from the analysis is shown in Figure B.30.

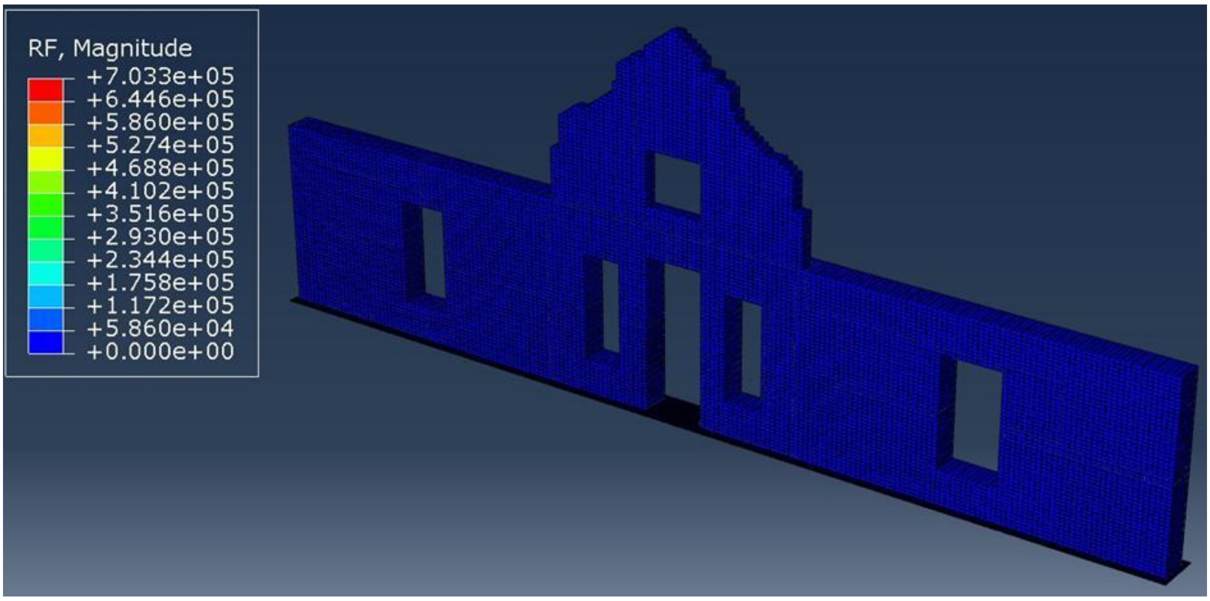

Figure B.30: Simulation 2: Reaction of the masonry wall along the Y-axis, in N

The reaction force obtained through the analysis of Simulation 2 is shown in Figure B.30 as 703.3 kN. This indicates an accurate analysis. The reaction force calculated through equilibrium equations is equal to 708.0 kN, which gives a margin of error of 0.7%.

The stress distribution, as shown in Figure B.28, indicates a similar pattern as Simulation 1. The model's peak stress magnitude is higher, located on the right-hand side of the door opening in the middle wall panel. This is attributed to the additional forces that the wind load has imposed.

A comparison of the distribution of deflection within the two models shows that the addition of the wind load increases the extent of the deflection. The wind load acting on the front face of the wall has imposed a peak deflection of 0.85 mm, which correlates with the peak deflection on the model with no wind load. However, the wind load's overall deflection is not significant.

The wind does not significantly influence the stress distribution and deflection of the masonry wall with the comparison of the results of Simulation 1 and Simulation 2. Therefore, failure in the masonry wall is not expected to occur because of wind action. However, a significant risk of failure is exposed due to the unbraced gable.

4.3. Simulation 3: Fully reconstructed condition with no wind load

The third simulation has been completed on an adjusted full model. An additional load imposed from the roof has been added to the gable wall. The loading on the wall has been increased to accommodate the additional load from the roof. Additional boundary conditions have been added to the gable wall to include the support provided by the roof structure.

The total load of the attic floor and the roof is assumed to be double the mass of the attic floor in isolation. As both elements are timber, it is assumed that each element has a similar thickness. The tributary area remains unchanged at 3 m. A portion of the loading is distributed over the gable. The loading element is shown in Figure B.31.

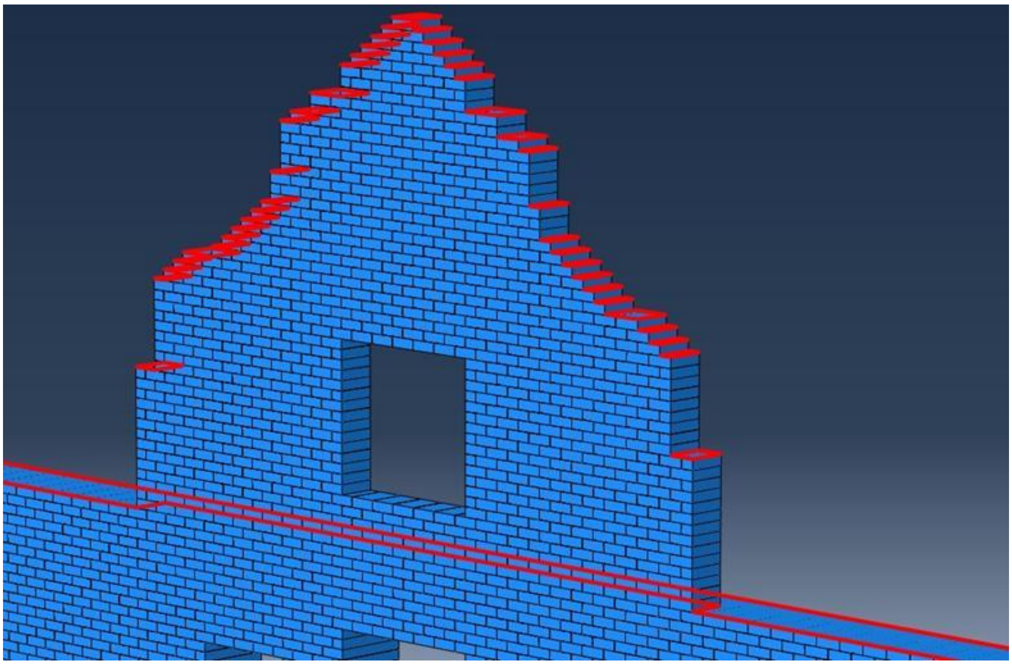

Figure B.31: Self-weight element simulating the roof and attic floor

With the fully reconstructed structure, the gable has been braced with the roof structure. The displacement in the Z-axis is fixed to zero. The roof bracing is shown in Figure B.32.

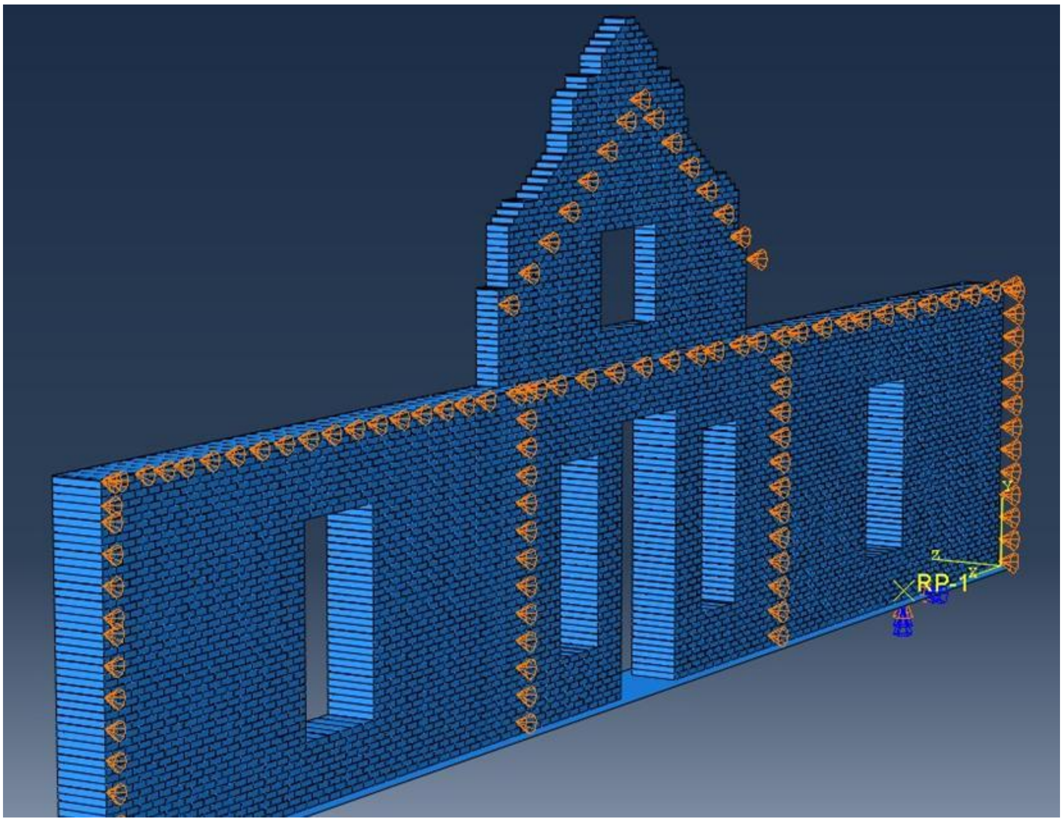

Figure B.32: Boundary conditions for the internal bracing on the wall and the gable

The analysis with the additional roof load and the braced gable has been completed successfully, and the stress distribution and deflection of the wall are shown in Figures B.33 and B.34, respectively.

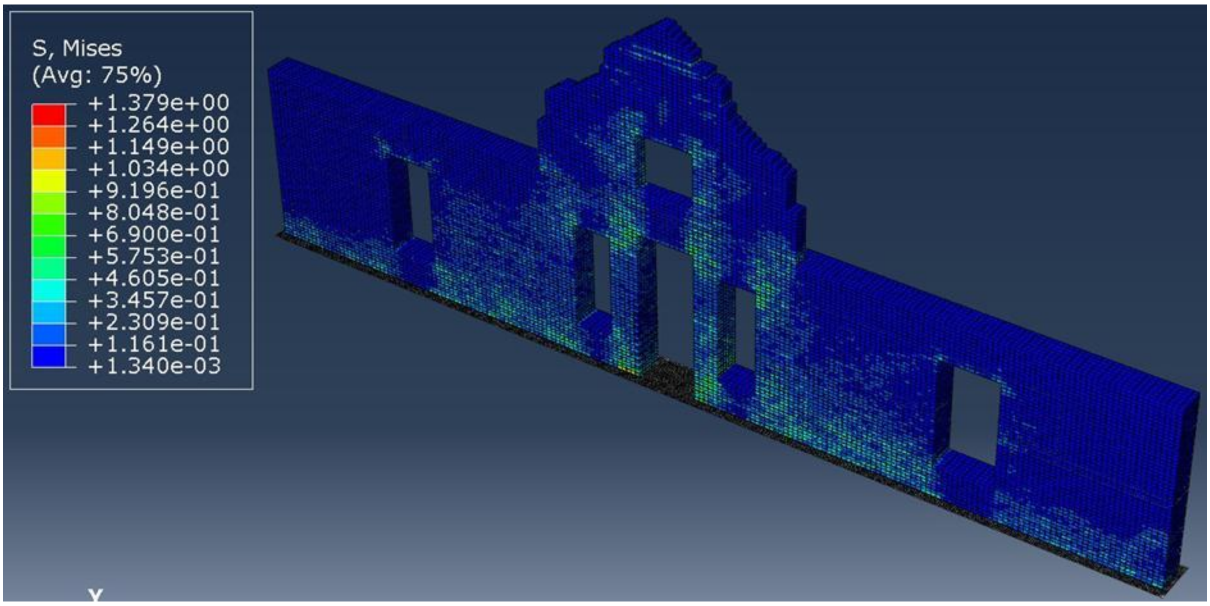

Figure B.33: Simulation 3: Distribution of Von Mises stress (MPa) on masonry wall

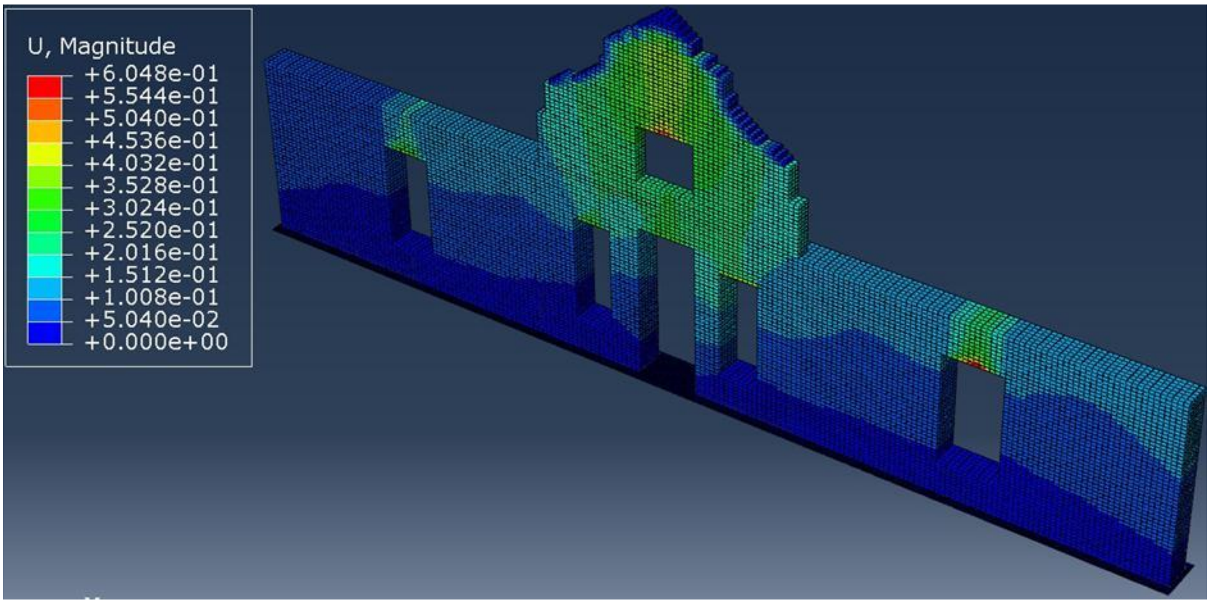

Figure B.34: Simulation 3: Displacement (mm) in horizontal plane

The model has been validated with a comparison between the analysed reaction force in the Y-direction and the calculated reaction force based on the overall self-weight. The analysed reaction force is shown in Figure B.35.

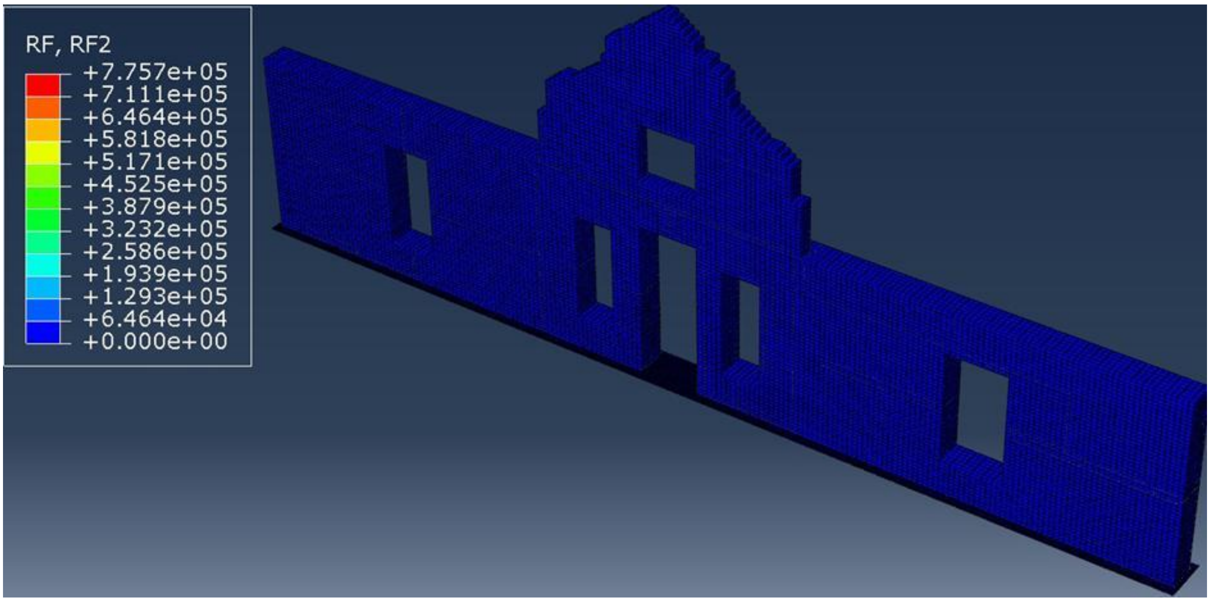

Figure B.35: Simulation 3: Reaction of the masonry wall along Y-axis, in N

The reaction force for the fully reconstructed model is based on the self-weight of the entire wall, attic floor and roof structure. This equates to a total reaction force of 778,6 kN. The analysis produced a reaction force of 775.7 kN, which indicates a margin of error of 0.4%. This indicates an accurate model.

Stress distribution is shown in Figure B.33, similar to the previous models, namely Simulation 1 and Simulation 2. The peak stress is shown to be less than the wall with the applied wind load but higher than the peak stress in the wall without wind loading. The stress areas in Figure B.33 indicate larger areas with higher stress due to the higher overall load imposed on the top of the wall.

The displacement in the wall, as shown in Figure B.34, is lower overall than the wall with the unbraced gable. The roof structure limits the horizontal displacement significantly, which underscores the need for the reconstruction of the wall to limit the overall risk of failure of the gable.

4.4. Simulation 4: Fully reconstructed condition with wind load

Simulation 4 has been completed on the similar model as Simulation 3. An additional wind load has been applied on the front face of the wall in the form of a pressure load. The load has been taken as q_k = 0.94 kPa (SANS 10160-3: Wind Actions). The pressure load indicating the wind load is shown in Figure B.36.

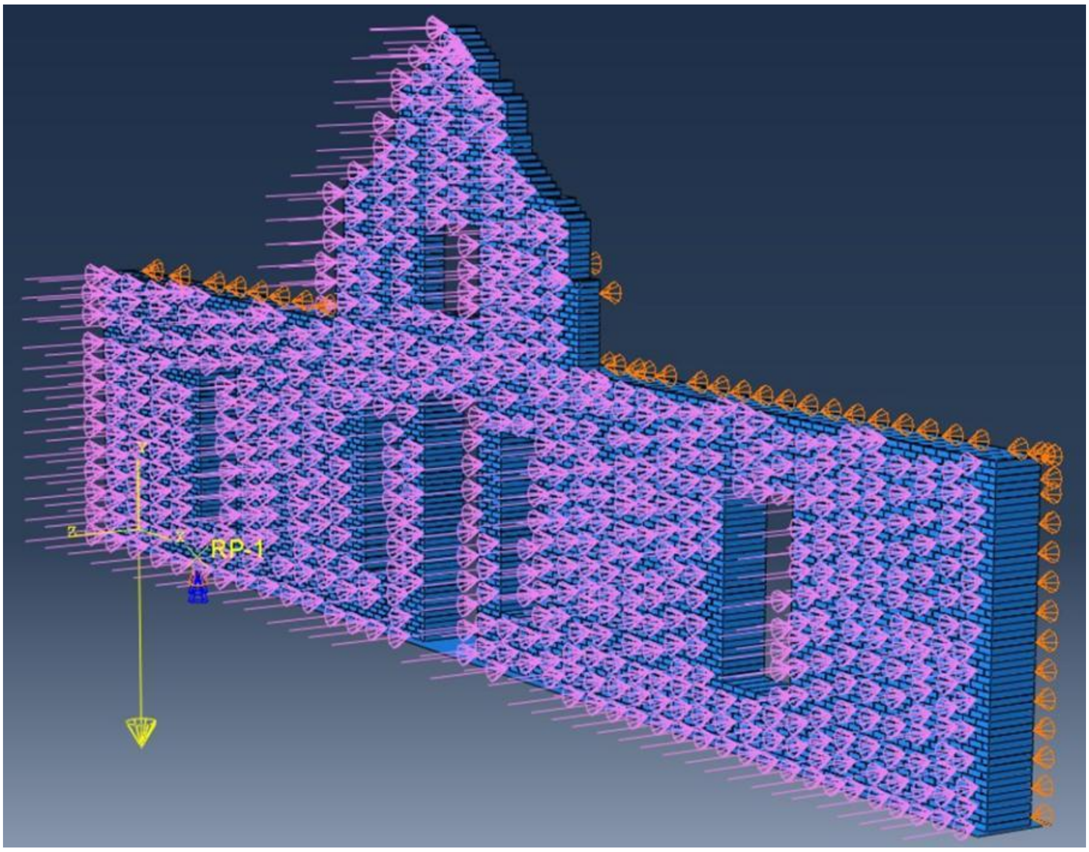

Figure B.36: Masonry wall with wind load in the Z-direction (horizontally)

All the boundary conditions selected for Simulation 3 have been kept constant, with only the wind load added to the model. Analysis has been completed successfully, and the stress distribution and displacement results are shown in Figures B.37 and B.38, respectively.

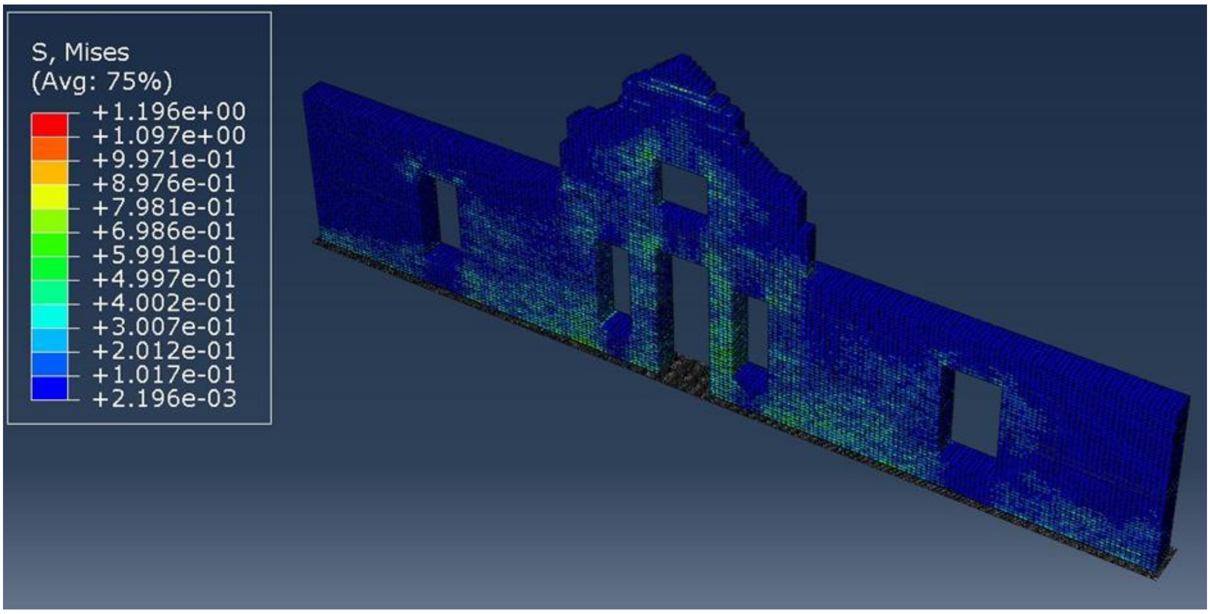

Figure B.37: Simulation 4: Distribution of Von Mises stress (MPa) on masonry wall

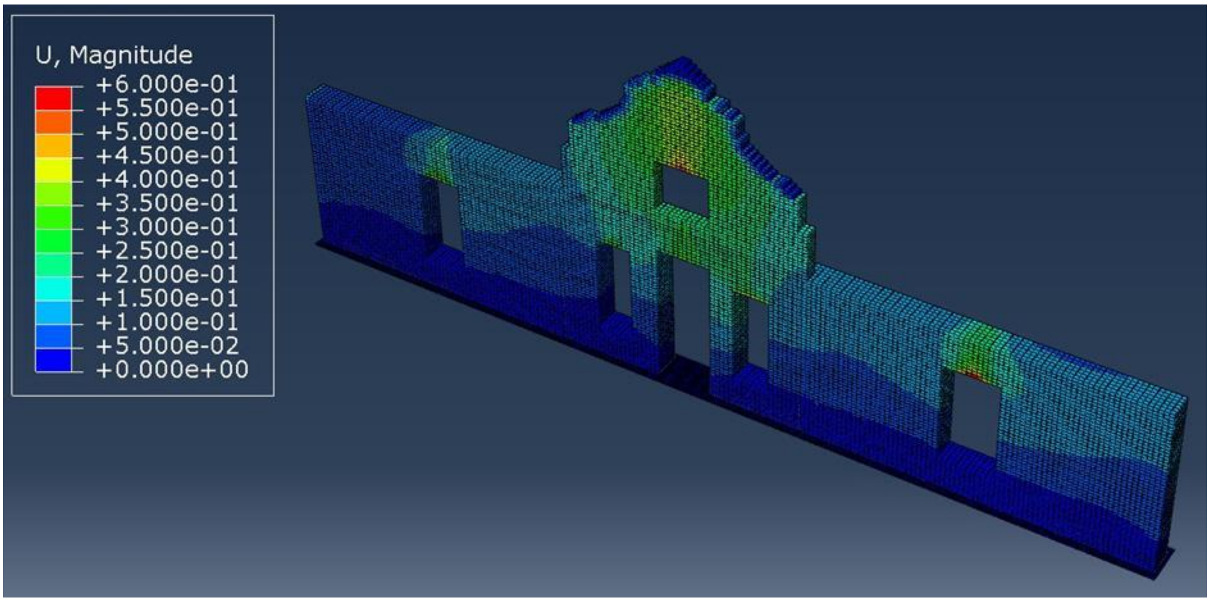

Figure B.38: Simulation 4: Displacement (mm) in horizontal plane

The model's validation has been undertaken by comparing the analysed reaction force in the Y-axis and the reaction force calculated through equilibrium equations. The analysed reaction forces are shown in Figure B.39. The degree of error has been determined.

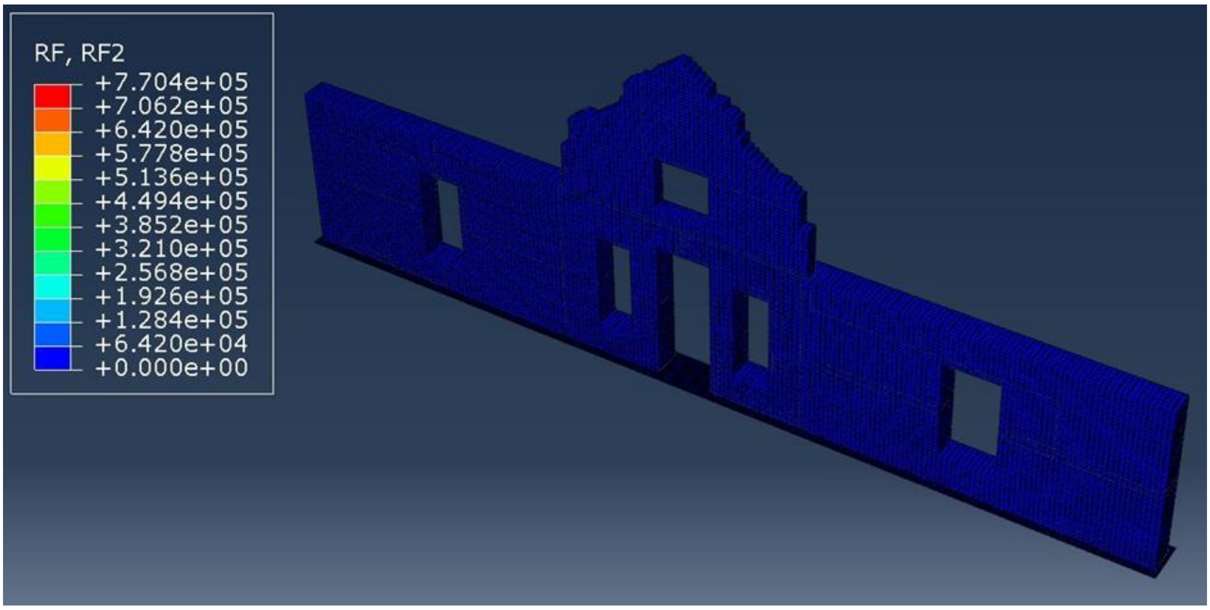

Figure B.39: Simulation 4: Reaction of the masonry wall along Y-axis, in N

The calculated reaction force on the fully reconstructed wall exposed to wind load is 778.6 kN on the Y-axis. From the analysis, a reaction force of 770.4 kN has been produced. This indicates a margin of error of 1.1%, which describes an accurate model.

The stress distribution shown in Figure B.37 indicates a similar stress pattern as shown in the analysis of Simulation 3. Although the peak stress on the model is lower than with Simulation 3, the stress distribution is denser due to the applied horizontal force on the wall. The overall difference in stress distribution is not significant enough to indicate a large influence from the applied wind load.

As shown in Figure B.38, the deflection indicates highly similar results, with a maximum displacement of 0.6 mm for both simulations. This further indicates the unstable nature of the unbraced wall which is at risk of collapse. This risk can be mitigated with the reconstruction of the roof structure.

5. Conclusion

Historical masonry structures exhibit complex behaviour because of weathering and ageing. Finite element analysis has proven to be a powerful tool for analysing these structures, especially where severe non-linearity is involved. This report has outlined the modelling process and the steps to develop an accurate and stable model. The following section provides a summary of the results obtained.

The finite element model has been developed following a “bottom-up” approach, initially starting with static analysis and a small test model. After the successful completion of each analysis, the model is scaled up until the full model size has been achieved. Throughout the steps, an increased number of convergence errors were evident, leading to failure analysis. This needs to be mitigated by incorporating automatic stabilisation through viscous damping. However, this reduced the overall accuracy of the analysis. The reduced accuracy prompted using a quasi-static analysis solver, significantly reducing the error margin.

A quasi-static analysis has been completed for the old masonry wall in two separate scenarios – the simulation of the wall in its current state and the simulation of the fully reconstructed wall. Each scenario has been analysed with and without wind loading. The four models have been analysed with a maximum margin of error of 1.1%.

The results obtained through analysis indicate the stress distribution and the estimated deflection for each model. It is evident that the unbraced gable wall is expected to be subjected to a higher degree of deflection and is thus at a higher risk of collapse. The stress distribution indicates a higher density in the stress distribution when the wind load is applied than without, confirming the influence of the load.

The stress distribution can further be compared with the crack patterns on the actual wall. A negligible difference in displacement is indicated when the simulation with an applied wind load is compared with the simulation without an applied wind load. The addition of the boundary conditions imposed by the reconstruction of the roof structure indicates a reduction in the expected deflections, further indicating the need for appropriate rehabilitation.

This report has indicated that the quasi-static solver is suitable for providing a stable model and producing accurate results. It is, therefore, a better option for the current model due to the high degree of nonlinearity.